THE DESIGN AND CHARACTERIZATION OF AN ATOMIC RUBIDIUM SOURCE AND APPARATUS FOR COUPLED LASER AND PARTICLE BEAM PROPULSION EXPERIMENTS

A Thesis

by

HAYDEN PATRICK MORGAN

Submitted to the Graduate and Professional School of
Texas A&M University
in partial fulfillment of the requirements for the degree of

MASTER OF SCIENCE

Chair of Committee,	Christopher Limbach
Committee Members,	Daniil Andrienko
	Philip Hemmer
Head of Department,	Ivett Leyva

December 2021

Major Subject: Aerospace Engineering

ABSTRACT

The need for a high specific impulse and innovative space propulsion technology is growing as NASA sets goals for exploring celestial bodies in our solar system and beyond. Directed energy space propulsion has been a candidate for these missions as it removes the need for thrusters and reaction mass systems from the science spacecraft. However, these proposed directed energy concepts, either in the form of electromagnetic (EM) radiation pressure (e.g. laser) or mass momentum beams (e.g. ion beams) suffer from inherent divergences that ultimately lower the total impulse transferred. A new concept for directed energy space propulsion utilizes a neutral atom beam spatially overlapped with a co-propagating laser which is detuned from the resonant frequency of the atom. Through refractive guiding and the optical dipole force, this combined beam shows potential for self-guiding over millions of kilometers.

The next stage for this low Technology Readiness Level (TRL) technology is ground experiment validation of theory and simulations. The present work describes efforts directed toward experimentally studying the combined beam propulsion system in laboratory-scale facilities. This includes the development of an atomic rubidium jet source, encapsulating vacuum facilities, laser overlapping and separation apparatus, and diagnostic techniques for studying the laser and atom beam. Tunable diode laser absorption spectroscopy (TDLAS) is applied toward characterization of the propagation parameters of the atomic jet including density, temperature, and axial velocity. The laser absorption profiles extracted from the TDLAS measurements indicate the presence from a cold group of atoms (< 10 K) and a hot group of atoms (50 - 200 K) which is predicted in literature for an atomic source that is transitioning from the continuum to free-molecular flow regime. The TDLAS data indicate that for a rubidium getter source at high current, the mass flow of the beam is approximately 2×10^{-3} μg/s. Although the mass flow rate from the rubidium source was lower than predicted, calculations of the waveguide V-Parameter indicate a potential light guiding capability for laser detunings less than 30 GHz from resonance. Findings from this initial experimental study to characterize the rubidium jet were used to influence the design of a combined

beam study which attempted to produce a sufficient dipole potential to reduce the divergence of an atomic jet.

The present work also describes novel advancements to the measurement capabilities through the development of new experimental apparatuses. The experiment added two additional TDLAS measurement stations and utilized a semi-automated synchronized spatial scanning gantry. Additionally, a method of separating the combined beam into the constituent atomic/laser beams was devised in order to study the final overlapped laser profile. Results from the combined beam experiment indicated that the atom temperature was at or above the 300 K ambient temperature, suggesting a significant degree of rubidium was present as background species in the chamber rather than in a low divergence jet. With the contamination of the jet diagnostics from the background rubidium, the behavior of the atomic jet could not be analyzed. However, the laser overlapping and separation systems did provide valuable data in terms of the interaction of the guiding laser with a rubidium vapor. The overlapped laser profile experienced detectable attenuation as it was tuned about the atomic resonance of the rubidium, which could be used in future experiments for atom jet bulk velocity measurements. Additionally, when the overlapped laser was tuned close to the atomic resonance, the TDLAS diagnostic stations confirmed a depletion of the ground state number density via the measured transmission.

DEDICATION

This dissertation is dedicated to my mother and father.

ACKNOWLEDGMENTS

This document provides a culmination of my two years of study and an achievement I take great pride in. My short time at Texas A&M University will always hold a place in my heart. While the rewards of my research will leave a lasting impact on me, the main reason I will fondly remember my time at A&M is the people. A graduate degree is not something one earns alone, and I am no exception. There are several groups of people in my life that unequivocally deserve to be acknowledged because, without them, this would not have been possible.

First, I would like to thank my mother and father. You both have given me so much love and support for as long as I can remember. You are my number one fans, the people I go to with good news and bad, and the people that have given me all the tools needed to be who I am. Through struggles and hardships, you have never once stopped showing me love. You have always been fantastic parents.

As my high school robotics and engineering teacher, I owe a great deal of who I have become to Tom Pope for fueling the initial spark of engineering. Thank you for the countless hours of teaching, guiding me through my decision to become an engineer, and being a friend to always turn to for guidance. The effort you put into going above and beyond the work of a teacher did not go unnoticed or unappreciated. You have left a lasting and profound impact on many of your students.

During my time as an undergraduate student at the University of Cincinnati, I forged some very strong bonds with an outstanding group of people. These bonds were tested through everything imaginable, including countless arguments and distances so far you needed to look up where a country was on a map. However, after seven years of experiencing the struggles of college and life, I am proud to give acknowledgement to Liberty Shockley, McKenzie Kinzbach, Russell Wilder, Jake Mueller, Ben Clark, Ian Schrock, and Sam Bauman. All of your successes fill me with enormous pride. You all taught me aspects of what it means to be a good engineer and a better person. Wherever we go in life, no matter what paths we choose, know I will always be supporting

you.

There are few things more intimidating to someone who has not lived outside their home city in 23 years, than moving 1,000 miles away from home for a graduate program. I have since counted my blessings on how fortunate I was to be placed with the group of people in my lab. From all walks of life and from unique backgrounds, we have all seen each other struggle, and we have all seen each other succeed. From learning new topics, running experiments, and even proofreading this document, the graduate students and faculty at the ALLEMO and NAL have been there for me since I started at A&M. Thank you to Yue Wu, Maddie Hetlage, Maddie Smotzer, Ashley Moran, Zachary Buen, Boris Leonov, Atulya Kumar, Frisco Koelling, Grant Erickson, James Creel, Cecil Rhodes, John Kochan, and the rest of the NAL and ALLEMO laboratories. You each have given me guidance when I have needed it, helped on my project in the limited spare time you have, or taught me something I hope to hold onto forever. You each have been a blessing to have in my life, and I am truly honored to call you all friends.

I must also acknowledge the team of undergraduate students I have had the privilege of mentoring throughout my research: Diego Morales, Rohan Jillapalli, William Hodges, and Kyle York. I greatly appreciate your dedication to this project. I know you will all go on to be great engineers.

I would also like to thank the NASA Space Technology Graduate Research Opportunities Office for awarding me with my NSTGRO fellowship. The honor of receiving this would have been sufficient, but it has also connected me with mentors and provided me a phenomenal internship experience that is allowing me leave A&M with confidence in my abilities as an engineering professional.

Lastly, I would like to thank my advisor, Dr. Christopher Limbach. You have been a lasting role model as an academic, a mentor, and a leader. Thank you for taking a chance on me, putting in the time and effort it took to get me where I am, and giving me opportunities to learn and better myself. I consider myself unfathomably lucky to have a research advisor that has shown vested interest in my success both professionally and personally. I have been fortunate enough in my short time at A&M to see the Laser Diagnostics and Plasma Devices Lab grow and expand in such

a great way. Your passion for learning and drive to contribute to the field is an inspiration for me and the other students in your lab.

My appreciation for you all, and many others, is limitless. May this be the first of many times I get to acknowledge you in my achievements.

CONTRIBUTORS AND FUNDING SOURCES

Contributors

This work was supervised by a dissertation committee consisting of Professor Christopher Limbach (committee chair) and Professor Daniil Andrienko (committee member) from the Texas A&M University Department of Aerospace Engineering, and Professor Philip Hemmer (committee member) from the Texas A&M University Department of Electrical Engineering. Additionally, Dr. Geoffrey Landis at NASA Glenn Research Center served as the NASA Research Collaborator as part of the NASA Space Technology Graduate Research Opportunities (NSTGRO) Fellowship.

A portion of the work disclosed in this thesis was done in collaboration with, or received a contribution from, the following people:

- Diego Morales (Texas A&M undergraduate student)- contributed to the designs of early vacuum infrastructure and the initial supersonic rubidium jet source as well as assisting in testing of the source.

- William Hodges (Texas A&M undergraduate student)- provided design assistance for early vacuum facilities, developed electronic hardware setup for controlling the MKS vacuum pressure gauge, created several LabView GUIs to log temperature and pressure over time, aided in experimental testing of the initial supersonic and effusive rubidium sources, and assisted in the design and manufacturing of the TDLAS spatial scanning gantry system.

- Rohan Jillapalli (Texas A&M graduate student)- assisted in vacuum facility assembly, maintenance, and testing, aided in experimental testing of the two effusive jet source configurations, and helped in developing a cleaning procedure for the rubidium in the chamber.

- Kyle York (Texas A&M undergraduate student) - created a LabView GUI for repositioning the TDLAS spatial scanning gantry, and developed the electrical and software infrastructure to micro-step the scanning gantry via an Arduino Uno.

- Anuj Rekhy (Texas A&M graduate student) - developed the rubidium absorption code which was modified and used as model to fit to the generated data.
- Grant Erickson (Texas A&M graduate student) - developed the data acquisition GUI used during the combined beam experiment to acquire voltage waveforms and record camera images.

All other work conducted for the dissertation was completed by the student independently.

Funding Sources

This work was supported by a NASA Space Technology Graduate Research Opportunity from August, 2020 to December, 2021. Previous graduate study was supported by a fellowship from Texas A&M University Department of Aerospace Engineering.

NOMENCLATURE

A	atom jet cross sectional area
A_{21}	Einstein A coefficient from excited state to ground
a	waveguide radius
α	atomic polarizability
B_T	combined beam brightness
C_{mp}	most probable speed
c	speed of light
Δ	laser detuning (angular frequency)
Δ_{opt}	optimal laser detuning
E_k	kinetic energy
e	charge of the electron
ϵ_0	vacuum permittivity constant
$\mathbf{F}_{dip}$	dipole force
F	hyperfine state quantum number
f_0	static frequency
f_{shift}	Doppler shifted frequency
$G(\omega)$	Gaussian lineshape function
Γ	excited state decay rate
Γ_{sc}	scattering rate

γ_N	natural linewidth
$\hbar$	reduced Planck's constant
I	electrical current supplied to rubidium source
I_{las}	laser intensity
I_{sat}	saturation intensity
Kn	Knudsen number
k	laser wavenumber
$\vec{\mathbf{k}}$	laser propagation unit vector
k_b	Boltzmann constant
$L(\omega)$	Lorentzian lineshape function
λ	laser wavelength
m	mass of atomic species
$\dot{m}$	mass flow rate
m_e	mass of the electron
$\dot{m}_{getter}$	mass flow rate from getter vapor source
N	number density of atomic vapor
N_A	area-integrated number density
NA	Numerical Aperture
n	complex refractive index
n_{clad}	refractive index of the cladding for a step-index fiber optic
n_{core}	refractive index of the core of a step-index fiber optic
ω	laser angular frequency

ω_0	atomic resonance angular frequency
P_{EM}	power of an electromagnetic radiation beam
P_{las}	laser power
P_P	power of a particle beam
Π	area divergence product
R_L	reflectance to an incident laser beam
R_P	reflectance to an incident particle beam
$\mathbf{r}$	radial vector in combined beam
r_{shroud}	radius of atom vapor flow limiting shroud hole
r_{source}	radius of atom vapor emission source
s	saturation parameter
T	temperature
T_{EM}	thrust from an electromagnetic radiation beam
T_r	recoil temperature
T_P	thrust from a particle beam
T_{total}	combined beam total thrust
$T_{\perp Cold}$	radial divergence temperature of cold atom vapor
$T_{\perp Hot}$	radial divergence temperature of hot atom vapor
θ	measurement angle
θ_{cold}	divergence angle for a cold atom vapor jet
θ_{couple}	maximum angle at which light can be coupled into a step-index fiber

θ_{las}	laser divergence angle
θ_{perp}	atom jet divergence half angle
U_{dip}	dipole potential
V	V Parameter (strength of refractive index)
v	velocity
v_b	velocity of the particle beam
v_{sc}	velocity of the spacecraft being accelerated
$v_\perp$	radial velocity
$v_\parallel$	axial velocity
w_0	laser beam waist radius
z_{sep}	source and aperture separation distance
CAD	computer-aided design
CF	ConFlat
$CMOS$	complimentary metal oxide semiconductor
CNC	computer numerical control
DAQ	data acquisition (system)
EM	electro-magnetic
GUI	graphical user interface
ND	neutral density (optical filter)
$PEEK$	polyether ether ketone
$PTFE$	polytetrafluoroethylene
RGA	residual gas analyzer

SAS	saturated absorption spectroscopy
$TDLAS$	tunable diode laser absorption spectroscopy
TRL	technology readiness level
UV	ultraviolet
$UVFS$	ultraviolet-grade fused silica
VDF	velocity distribution function

TABLE OF CONTENTS

Page

LIST OF FIGURES

FIGURE Page

LIST OF TABLES

TABLE Page

1. INTRODUCTION

Space missions to distant celestial bodies within our solar system, extrasolar objects [2], the solar gravity lens point [3, 4], or the nearest star system [5], must all reach substantial speeds to reach their target within a reasonable mission duration. Traditional chemical propulsion offers large total impulse, but is not very efficient (low specific impulse), thus not well-suited for deep space missions. Developments in ion thrusters and plasma propulsion systems have yielded significant increases in specific impulse, which has extended the reach of feasible missions. However, for the most distant celestial objects and locations, new forms of space propulsion are required. An appealing candidate for these challenging missions is directed energy propulsion.

1.1 Directed Energy Space Propulsion

Directed energy propulsion removes the requirement for thrusters and reaction mass systems from the science spacecraft, and instead harness momentum from a form of energy directed toward the craft. One main benefit of using directed energy is that the emission source can often be located on Earth or near Earth [6]. Developing structures for Earth orbit often affords a greater mass budget than for systems bound for deep space. For this reasons, the emission sources can be readily serviced, store greater amounts of propellant (or energy), and be located near an energy source. The most common concepts for directed energy propulsion are radiation pressure and mass momentum beams.

1.1.1 Radiation Pressure

Within the category of radiation pressure propulsion, a large effort has been primarily focused on electromagnetic (EM) radiation pressure [7, 8, 9, 10, 11, 12, 13, 14, 15]. Concepts usually involve either Earth-based laser systems [11] or near-Earth laser systems [16] to transmit the EM beam to the spacecraft. Assuming all incident light is either absorbed or reflected, the pressure exerted on a surface by an EM wave, P_{EM} is [17],

$$P_{EM} = (1 + R_L)\frac{I_{las}}{c}, \tag{1.1}$$

where R_L is the reflectivity of the surface ($R_L = 1$ for fully reflective), I_{las} is the laser intensity incident on the surface, and c is the speed of light. Equation 1.1 can be reduced to get the EM thrust, T_{EM}, by multiplying both sides of the equation by the craft incident area,

$$T_{EM} = (1 + R_L)\frac{P_{las}}{c}, \tag{1.2}$$

where P_{las} is the cumulative EM power on the craft area. Equation 1.2 uses the assumption that there is no transmission through the spacecraft, only absorption and reflectance. A spacecraft that absorbs all incident radiation would have a reflectance of $R_L = 0$, but a fully reflective craft would have a reflectance of $R_L = 1$, thus doubling the thrust. From Equation 1.2, the thrust to input power ratio is heavily reduced by a factor of the speed of light, thus requiring high laser intensity, spacecraft area, or both to achieve substantial thrust. The benefit of using laser-based EM pressure is that spacecraft are able to be fairly lightweight but require unique reflective "sail" material over a large area to be effective [8]. A drawback to laser beam propulsion is the inherent diffraction, meaning a laser cannot stay collimated indefinitely. For the fundamental Gaussian laser mode, the divergence angle , θ_{las}, is,

$$\theta_{las} = \frac{\lambda}{\pi w_0}, \tag{1.3}$$

where λ is the laser wavelength and w_0 is the beam waist radius [17]. This beam divergence yields a substantial loss mechanism for thrust on the science spacecraft as it propagates. Due to the spreading laser, the incident power on the sail area is gradually diminished, thus limiting the maximum acceleration distance/time that can be achieved. There have also been concepts proposed that utilize the EM pressure provided by our Sun at close distances to receive greater final velocities or orbital station keeping [18, 19, 20]. However, these sail concepts rely only on a relatively short acceleration period due to the solar flux. Methods for reducing the impact of laser divergence

through large-scale laser arrays or larger laser sails [16, 11] have been proposed. There have been alternative concepts that consider the use of lens arrays spaced along the propagation to refocus the beam [21]. However, concepts that require substantial in-space infrastructure development often coincide with significant engineering challenges.

1.1.2 Mass Momentum Transfer

Another form of directed energy space propulsion being considered is particle beam propulsion. The term particle, in this context, is used to encapsulate atoms, molecules, and ions [22]; any particle which has mass that is being used to transfer momentum to the spacecraft. The benefit of using particles to propel a spacecraft is the higher momentum to energy ratio imparted to the craft and energy efficiency in the emitter compared to laser propulsion [23]. Assuming all particles are either absorbed or reflected, the thrust imparted to the spacecraft by the particle beam, T_p, in terms of beam power, P_p, is,

$$T_p = \frac{2(1+R_p)P_p}{v_b}\left(1-\frac{v_{sc}}{v_b}\right)^2, \tag{1.4}$$

where R_p is the particle reflectivity and v_b and v_{sc} are the velocities of the beam and spacecraft, respectively [24]. For the case of $v_b >> v_{sc}$, the thrust to power ratio is high; providing a peak value that is greater than laser propulsion system with equivalent power by a factor of $\frac{2c}{v_b}$ [24]. However, the thrust to power ratio drastically declines as the spacecraft accelerates to near the particle beam velocity, thus providing a limit to the maximum obtainable velocity.

Similar to the laser-based EM propulsion concepts, particle beams also have a degree of divergence. As the particles are emitted from a source, they have some inherent axial velocity, $v_{\parallel}$, and a transverse velocity, $v_{\perp}$. The group of atoms can be consider to have a most probable transverse speed, C_{mp}, given a certain temperature, T, which is described by [25],

$$C_{mp} = \sqrt{\frac{2k_bT}{m}}, \tag{1.5}$$

where k_b is the Boltzmann constant and m is the mass of the atom. As with laser divergence,

this "thermal" spreading of the particle beam leads to significant losses and is often more prominent than laser divergence. The divergence of the particle beam is simply the ratio of $v_\perp/v_\parallel$ (for small divergence angles). Since particle beams provide greater thrust efficiency but suffer from a larger divergence, effort has been spent evaluating concepts for minimizing the divergence, such as guidance beacons [26] and laser cooling [27] .

The two concepts of directed energy space propulsion discussed previously each have their unique benefits. Radiation pressure propulsion typically has less divergence but a lower momentum transfer efficiency. Particle beam propulsion offers greater thrust efficiency but often suffers from greater divergence unless divergence mitigation efforts are employed. Additionally, the EM beams are not as velocity limited as the particle beam propulsion, which degrades in thrust as the spacecraft velocity approaches the velocity of the particles. The common pitfall between both methods is the divergence of the beams, which lowers the incident flux on the science spacecraft as it accelerates. A concept for a significant reduction in the beam divergence would yield a more efficient propulsion system for deep space and interstellar missions.

1.1.3 Self-Guiding Beam Concept

Through the combination of a neutral atom beam and a laser beam, Limbach and Hara theorize that a mutual guiding effect can be generated that will significantly reduce the divergence of the beams over millions of kilometers [24]. This self-guiding beam concept spatially overlaps a high power laser beam with an alkali atom beam in a space-based transmitter. This combined beam is then directed to a science spacecraft which would then reflect, redirect, or absorb both the neutral atoms and incident laser to harness the momentum from the beam. The resultant thrust, T_{total}, would be the cumulative sum of the constituents,

$$T_{total} = T_{EM} + T_P. \tag{1.6}$$

The operating principles behind this mutual guiding effect will be discussed in detail in Chapter 2, but in brief, the laser is guided through the heightened index of refraction generated inside

the atom beam compared to the outside vacuum. Likewise, the atom beam is guided through a dipole potential trap, generated by the overlapped laser being detuned from atomic resonance, which is able to confine the atoms in the transverse direction. The laser will be guided unless diffraction overcomes the refractive guiding strength. Whereas, the atoms are able to maintain confinement so long as their transverse temperature does not overcome the depth of the dipole potential trap generated by the laser. Atom temperature increase presents a primary loss mechanism for the combined beam system through scattering or stochastic heating. An atom in an EM field experiences two primary optical forces: the dipole force and the scattering force stemming from the real and imaginary components of the atomic polarizability, respectively. The dipole force yields the confinement of the atoms, whereas the scattering force, contributes to re-radiation of the absorbed field, causing an increase in the atomic temperature. Significant increase in the transverse temperature of the atoms could generate a kinetic energy that exceeds the dipole potential energy, thus causing the atom to escape confinement. Chapter 2 will provide insight into how to reduce this scattering effect and maintain a strong dipole potential.

During their initial study, Limbach and Hara determined that the combined beam brightness, B_T, was a figure of merit of the self-guided beam [24]. The beam brightness is a metric for quantifying the mass flow rate that can be directed to a spot size at a distance and is defined in terms of beam parameters as,

$$B_T = \frac{e\dot{m}}{m\Pi E_K}. \tag{1.7}$$

Here, E_K is the kinetic energy of the atoms, $\dot{m}$, is the atom mass flow rate, and Π is the area divergence product of the beam. Maximizing the combined beam brightness through increasing the mass flow rate and lowering divergence is an area of consideration in developments of the self-guided beam concept.

1.2 Previous Demonstration of Guiding Phenomena

These self-guiding phenomena are not new to the field of physics and have individually been reported on extensively in literature. However, the concept is novel through its combination of the

two beams and tailoring the system parameters to yield a mutually collimated beam over millions of kilometers. The Hara group at Stanford University has produced multiple simulation studies of the combined beam with increasing fidelity [28, 29, 30]. The simulation effort thus far has been primarily focus on verifying their findings with publications of the individual guiding effects, such as the work with sodium atoms preformed by Bjorkholm et al. [31].

1.2.1 Laser Guiding

Light and laser guiding through a refractive index gradient is a common phenomenon used in fiber optics for data transfer and other waveguides [32]. Unlike in a solid fiber optic media, the refractive index consider here stems from and atomic vapor. The index of refraction of a vapor, discussed at detail in Section 2.2, has a strong dependence on the laser frequency and atomic density. As the laser is tuned closer to the atomic resonance frequency, the index of refraction experiences an increase as does the amount of laser attenuation experienced [33]. This attenuation, or laser absorption, is the fundamental principle behind laser absorption spectroscopy, which is used to study the parameters of a gaseous species [34]. The refractive index is a complex value and the laser attenuation stems from the imaginary component. The refractive guiding strength, required for the self-guiding beam, is a measure of the real component of the refractive index. As discussed previously, re-radiation of the absorbed EM field leads to heating of the atoms. This effect has been considered in studies of cold gasses and Bose-Einstein condensates that require optical probing which will not substantially heat the subject [35, 36, 37].

1.2.2 Atom Guiding

Guiding or trapping of atoms via a dipole potential is less commonplace than the light guiding phenomena, but still well discussed in literature [38, 39, 31, 40, 38, 41, 42, 43]. Partially due to their short excited state lifetimes, alkali atoms have been used in dipole trapping schemes to generate cold vapors and Bose-Einstein condensates [44, 45, 46]. There are two primary methods for manipulating the atoms with an EM field, the radiation pressure trap which functions near atomic resonance and the optical dipole trap which utilizes far laser detunings. Radiation pressure traps

work by imparting momentum from the photon to the atom upon absorption. Through the precise direction of multiple beams the temperature of the atoms can be significantly reduced. The temperature limit of the radiation pressure trap is associated with the balance between optical drag and photon re-radiation; this is known as the Doppler temperature. Optical dipole traps have a much lower temperature limit associated with the re-radiation of a single photon, known as the recoil temperature (Section 2.1). Optical dipole traps can be used in complex schemes to directly generate Bose-Einstein condensates by continually reducing temperature through confinement [39].

Of primary relevance to this work, optical dipole traps have been shown to focus a jet of neutral alkali atoms [43, 31]. In their work, Bjorkholm et al. was able to demonstrate a significant atom focusing effect for a red detuned overlapped laser on a length scale of 55 cm [31]. While the focusing effect was quantified for the atoms, no literature has shown the consequential influence on the overlapped laser. Understanding the behavior and effect of both constituent beams in the self-guiding beam concept is critical to predicting future behavior and for further manifestations of experiments.

1.3 Studies of the Self-Guiding Beam

The self-guiding propulsion concept has seen recent advancement through developments in simulations and analysis of the theory. However, these simulations need to be validated with experimental data to prove they can accurately model the self-guiding phenomenon. Once these simulations have been validated with small-scale experiments, they can attempt to predict the behavior of larger-scale tests, and ultimately be used to generate accurate mission profiles for a space-based demonstration or use case. However, this ladder of advancement, or technology readiness levels (TRL), must first start with laboratory scale experiments. The focus of the work enclosed in this dissertation is the design, construction, and analysis of infrastructure and apparatus required to study this self-guiding beam. To validate simulation data, the system input parameters must be well quantified. For the particle beam, these initial parameters are the mass flow rate, density distribution, axial velocity, and transverse velocity/temperature. The initial overlapped laser intensity profile, frequency, focal point, and beam size are important data to quantify but are fairly trivial

to measure. From this initial set of input parameters, the behavior of the combined beam will be analyzed as the input parameters are swept. Each parameter variation yields a test case to validate simulations. The behavior of the combined beam can be quantified using non-intrusive laser diagnostic techniques to measure the density, temperature, and axial velocity of the alkali atom beam. Additionally, the final overlapped laser profile can be extracted after the propagation and any changes to the profile due to refractive effects can be analyzed.

This dissertation will cover the course of two fundamental experiments used to test and develop the infrastructure for initial experiments of the self-guiding beam. The first experiment is a jet characterization study that served to quantify the initial input parameters of the atom jet into the experiment while also testing the effectiveness of the laser diagnostic technique and other experimental equipment. The second experiment tested infrastructure improvements from findings in the first experiment as well as introducing the overlapped laser to test the guiding behavior. The experimental facilities and design rationale for both experiments are discussed in Chapter 3. The findings as well as some insight to sources of error in each study are provided in Chapter 4. Lastly, Chapter 5 focuses on what was learned through these studies and what are the next steps toward laboratory studies of self-guided beam propulsion.

2. BACKGROUND*

This chapter discusses the physical basis for the mutual guiding phenomena as well as the behavior of the jet source utilized in the experiments. There are two primary mechanisms that give rise to the self-guiding behavior of the combined beam: optical forces on the atoms in an electromagnetic (EM) field and refractive effects on laser propagation in a gaseous medium. Both are fundamentally related to the electric dipole response of neutral atoms to an electromagnetic wave.

We begin by considering the dipole response within the semi-classical quantum picture of a two-level atom [47]. In this framework the atom is treated quantum mechanically while the applied electric field is treated as a classical, continuous wave. For a simple two-level atom with decay rate, Γ, the steady-state response to a harmonic wave is obtained by solution of the time-dependent Schrodinger equation [47]. A key parameter emerging from this analysis is the saturation parameter, s, which quantifies the extent of ground state depletion. Higher intensity lasers tuned closer to atomic resonance can generate substantially high saturation, which reduces the strength of the optical dipole response and therefore the atomic forces and refractive index (dipole moment). The saturation parameter for a two-level atom is given by, [48],

$$s = \frac{\frac{I_{las}}{I_{sat}}}{1 + 4\left(\frac{\Delta}{\Gamma}\right)^2}, \tag{2.1}$$

where I_{las} is the laser intensity, I_{sat} is the saturation intensity of the atom, Δ is the detuning of the overlapped laser, ω, relative to the central resonant frequency of interest, ω_0, and Γ is the excited state decay rate. For a rarefied flow, collisional quenching can be neglected, resulting in Γ becoming effectively the spontaneous emission coefficient or Einstein A coefficient of the transition, A_{21} [48]. Under these assumptions the saturation intensity can be expressed as [42, 48,

*Part of the information in this chapter is reported in "Design and Characterization of an Atomic Rubidium Jet Source for Particle Beam Space Propulsion" by Morgan, H.P., Morales, D., Hodges, W.L., Jillapalli, R.D., and Limbach, C.L. 2020. *AIAA Propulsion and Energy Forum*, Copyright 2020 by Texas AM University and reprinted with permission.

49],

$$I_{sat} = \frac{\hbar \omega_0^3 A_{21}}{4\pi c^2}, \tag{2.2}$$

where $\hbar$ is the reduced Planck constant.

The influence of saturation on optical forces and refractive effects will be discussed in their respective sections. It is critical to consider these effects for laboratory-scale experiments as it may be necessary to operate the combined beam at high saturation in order for guiding effects to manifest in the rarefied media. Additionally, near-resonance regimes where saturation is non-negligible provide another useful point of validation for simulations.

2.1 Optical Forces

For neutral atoms inside an EM field, such as a laser, there are two fundamental forces acting on the atom. The first is the well-known scattering force that stems from conservation of momentum during the photon-atom scattering process [47]. For a two-level atom with negligible saturation and collisional quenching, the expression for the scattering rate at small detuning is [40],

$$\Gamma_{sc}(\mathbf{r}) = \frac{3\pi c^2}{2\hbar \omega_0^3} \left(\frac{A_{21}}{\Delta} \right)^2 I_{las}(\mathbf{r}). \tag{2.3}$$

Here, $\mathbf{r}$ is the radial position vector of the beam. The scattering force acts in the laser propagation direction as a result of recoil from the incident photon momentum. However, the re-emission and scattering of these photons results in a random walking behavior that leads to an increase in the random thermal motion (kinetic temperature) of the atom. The characteristic temperature rise of a single scattering event is known as the recoil temperature, T_r, which is defined as,

$$T_r = \frac{\hbar^2 k^2}{m k_b}, \tag{2.4}$$

where k is the wavenumber of the overlapped laser. From Equation 2.3 and 2.4, it can be determined that an overlapped laser tuned close to resonance (i.e. Δ is small) can result in a significant rise in atom temperature over time. For a jet of atoms, an increase in temperature results in an

increase in the jet's divergence.

The second fundamental force on an atom in an EM field is the optical dipole force (see a classical derivation provided by Demtroder [49]), which is a critical component in the self-guiding interaction. The optical dipole force, F_{dip}, acts in the gradient of the intensity of the EM field and can be written as [40],

$$\mathbf{F}_{dip}(\mathbf{r}) = -\nabla U_{dip}(\mathbf{r}) = \frac{1}{2\epsilon_0 c} Re(\alpha) \nabla I_{las}(\mathbf{r}), \tag{2.5}$$

where ϵ_0 is the vacuum permittivity constant, α is the complex polarizability of the atom, and U_{dip} is the dipole potential. The dipole potential will confine an atom if the transverse kinetic energy of the atom is less than the dipole potential depth. Under the same assumptions of negligible saturation, two-level atom, and negligible collisional quenching, the dipole potential be expressed as [40],

$$U_{dip}(\mathbf{r}) = \frac{3\pi c^2}{2\omega_0^3} \frac{A_{21}}{\Delta} I_{las}(\mathbf{r}). \tag{2.6}$$

Depending on the sign of laser detuning, the dipole potential will either pull atoms toward the high intensity regions of the laser (behaving as a potential well for red detunings) or away from the high intensity regions of the laser (behaving as a potential hill for blue detunings). The dipole potential can be equated to an effective temperature by dividing U_{dip} by the Boltzmann constant, k_b. It is often useful to consider the potential depth as a temperature to directly quantify the trapping time as the atoms are heated via scattering. Additionally, it is important to note the dependence on laser detuning for the scattering rate and dipole potential in Equations 2.3 and 2.6. The dipole potential decays as Δ^{-1}, whereas the scattering rate decays as Δ^{-2}. For this reason, dipole trapping schemes are typically operated far-off resonance to drastically decrease the primary loss mechanism (scattering) while still providing a strong enough dipole potential to trap the atoms. Kumar et al. evaluated the optimal detuning for long propagation overlapped laser and atom beam systems in ordered to maximize density amplification. For negligible saturation effects, the optimal

detuning, Δ_{opt}, is approximated as [28],

$$\Delta_{opt} = \left(\frac{A_{21}^2}{6\pi m^2 c}\right)^{\frac{1}{2}} \left(\frac{P_{las}}{|\vec{v_{\parallel}}|^3 \theta_{\perp}^2}\right)^{\frac{1}{2}}, \tag{2.7}$$

where $\vec{v_{\parallel}}$ is the initial axial velocity of the atoms and $\theta_{\perp}$ is the divergence half-angle of the atoms.

While Equations 2.3, 2.6, and 2.7 assume negligible excited state saturation, it may be beneficial to operate close to resonance and/or at high laser power in which the saturation parameter (Equation 2.1) becomes non-negligible. In these instances, the equations for scattering rate and dipole potential must be adjusted to account for saturation by using the following formulas [48],

$$U_{dip}(\mathbf{r}) = -\frac{\hbar\Delta}{2} \ln\left(1 + s(\mathbf{r})\right), \tag{2.8}$$

$$\Gamma_{sc} = \frac{A_{21}}{2} \frac{s(\mathbf{r})}{1 + s(\mathbf{r})}. \tag{2.9}$$

Figure 2.1 shows the trends of the dipole potential with detuning including the influence of the saturation parameter. This enhancement of the dipole potential illustrates a potential benefit of operating in a higher saturation regime.

Since the scattering rate also sees significant increase in higher saturation regimes, this is not a desirable regime for the full-scale space transmitter to operate in. However, with laboratory scale lasers and power budgets saturated regimes offer a way of increasing the dipole potential. Additionally, quantifying the guiding interaction while saturation is non-negligible yields a more comprehensive understanding of the guiding interaction throughout the range of viable detunings.

2.2 Refractive Effects

In addition to optical forces, the self-guiding beam interaction requires laser confinement through the increase in the refractive index, n, of the atom vapor beam compared to the surrounding vacuum. This guiding effect is fairly common and is the fundamental principle behind fiber optics and other waveguides. The varying refractive index of a vapor media has also been used for

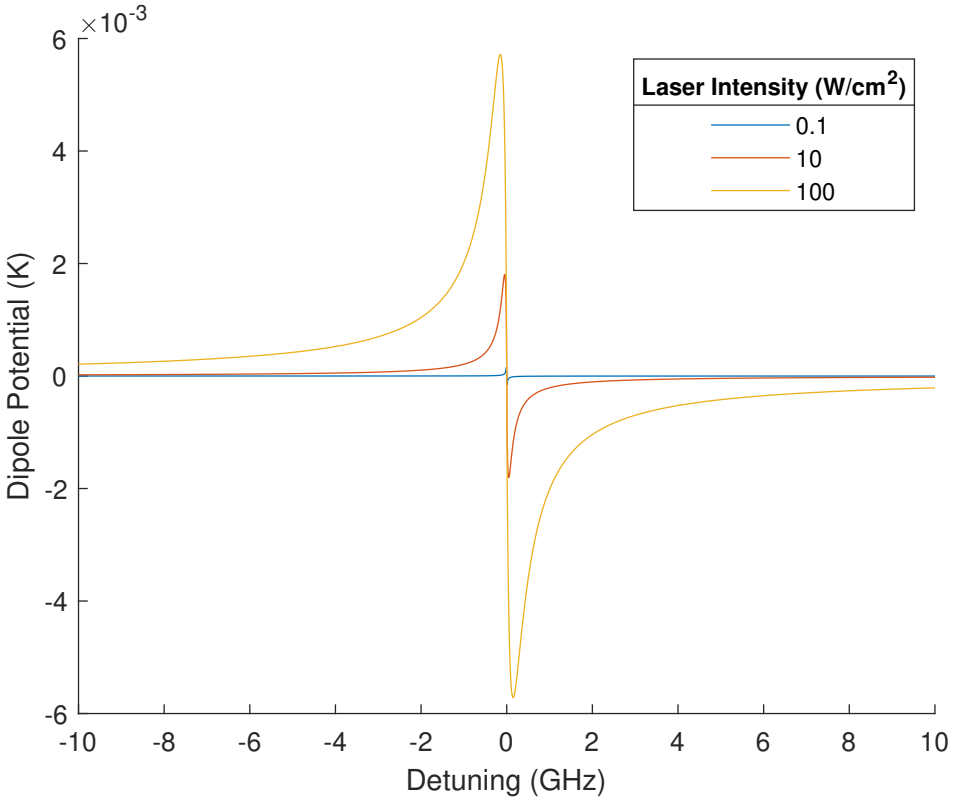

Figure 2.1: Dipole potential with saturation effects considered for various laser detunings and intensities.

diagnostics of cold atomic vapors [35]. Just as the atom confinement phenomenon has a guiding aspect and dissipation, the refractive index is a complex property where the real component leads to light guiding and the imaginary component leads to absorption/attenuation due to the scattering process. The complex refractive index, n, for a diffuse atomic vapor medium with negligible saturation effects and collisional quenching can be described as [49],

$$n = 1 + \frac{N\alpha}{2\epsilon_0}, \tag{2.10}$$

$$\alpha = \frac{\frac{e^2}{m_e}}{\omega_0^2 - \omega^2 - iA_{21}\omega}, \tag{2.11}$$

where N is the gas number density, m_e is the mass of the electron, and e is the charge of the

electron. From Equations 2.10 and 2.11, it is important to note that the real component of the refractive index is above unity for red laser detuning but below unity for blue detuning. This relationship means that a vapor beam can only couple a red detuned laser beam for guiding when surrounded by vacuum.

The refractive index of the vapor medium has a direct impact on the maximum divergence angle of light that can confined in the vapor. While not a direct comparison to a gaseous vapor beam, the step-index optical fiber illustrates the importance of increasing the refractive index. The numerical aperture, NA, of an step-index optical fiber is the largest angle of incidence that can be coupled into the fiber core. The numerical aperture is defined as [17],

$$NA = \sqrt{n_{core}^2 - n_{clad}^2} = \sin\theta_{couple}, \tag{2.12}$$

where n_{core} is the refractive index of the core of the optical fiber (the greater refractive index), n_{clad} is the index of refraction for the cladding surrounding the core, and θ_{couple} is the maximum angle that can be coupled into the optical fiber. If the density distribution of the atoms in the jet can be approximated as a flat-top profile, then the behavior would more closely resemble a step-index fiber. However, Section 2.3 will discuss the cross-section density distributions and it is found that a more appropriate analogy would be that of a graded-index fiber. Another critical metric for the fiber waveguides is the V Parameter, V, which is a direct ratio between refractive strength and inherent diffraction. The V Parameter can be used to quantify the number of guiding modes that can be guided in a waveguide. The fundamental mode is a pure Gaussian profile, however, with a higher V Parameter, more spatial modes are able to propagate in the fiber. The V Parameter can be calculated as [50],

$$V = \frac{2\pi a}{\lambda} NA, \tag{2.13}$$

where a is the fiber radius. If the amount of spatial modes able to propagate is limited, the power of an initially coupled laser beam will ultimately become restricted to the modes which can be

sustained in the fiber. Castillo et al. discusses that for the self-guided beam interaction, a V Parameter of 2 is optimal [29], which corresponds to a critical atom density for the interaction [24].

Similar to the optical forces, the refractive index is heavily influenced by the effects of saturation. For overlapped/coupled lasers tuned to have high saturation, the refractive index equation would need to be modified from Equation 2.10 to the following [49, 48]:

$$n = 1 + \frac{N\alpha}{2\epsilon_0(1+s)}. \tag{2.14}$$

The refractive index relative to vacuum decays on the order of $(1+s)^{-1}$, which is shown in Figure 2.2. For this reason, saturation effects can significantly reduce the light guiding capability of a low density vapor beam.

2.3 Effusive Flow Behavior

The self-guiding beam concept relies on the generation of a high mass flux, low divergence jet of atoms. Supersonic atom sources typically offer greater mass flux and less divergence, however, the complexity of a supersonic source design can pose challenges for laboratory scale experiments. To focus the area of study to the self-guided beam interaction, an effusive source geometry was chosen and will be described in detail in Chapter 3. Regardless of the source regime chosen, minimizing collisions in the particle beam is an important design consideration to prevent collision losses. For a gaseous flow expanding into vacuum, it will likely enter the free-molecular flow regime ($Kn > 10$) at some point beyond the emission source. As the flow continues to expand, collision events between particles become more rare and the particles will travel on their ballistic trajectories if left unperturbed. The emission of the gaseous jet is a significant consideration; the particles can be emitted in a supersonic plume, without collisions in an effusive flow, or a regime in between these two. The particle emission regime greatly impacts the flow behavior in the particle beam. Cai and Boyd provide an analytical relationship for the density, axial velocity, and transverse velocity of a collisionless gas expanding into vacuum [1]. Using these analytical

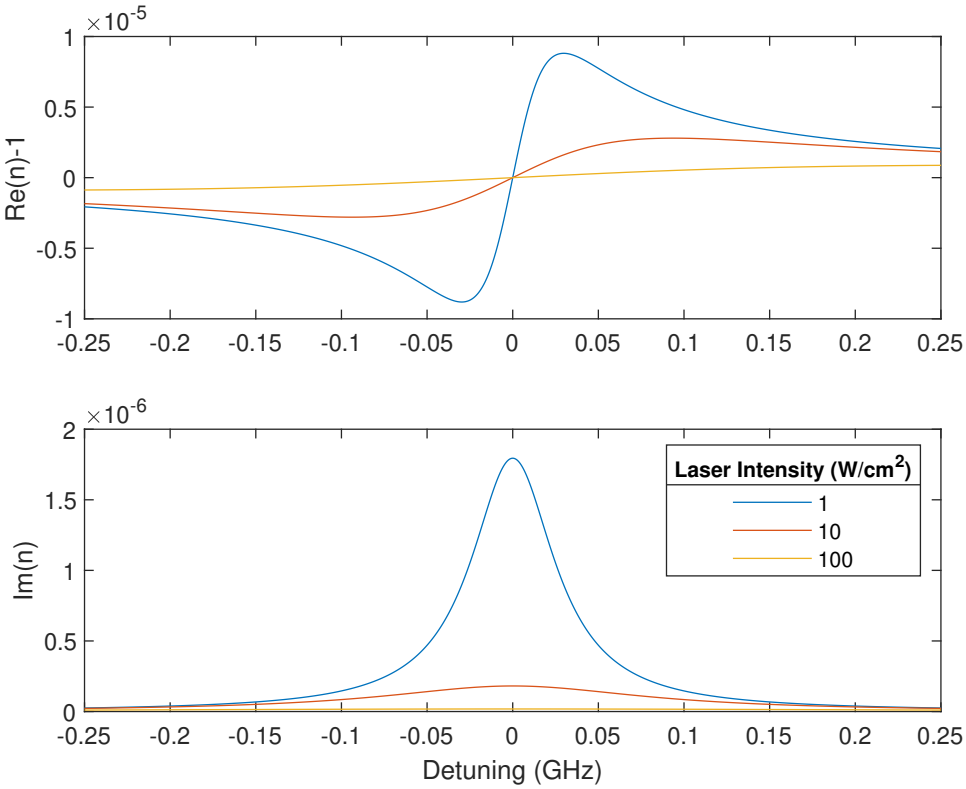

Figure 2.2: Real component of refractive index - 1 and imaginary component including saturation effects as a function of detuning and laser intensity. The plot shown uses an arbitrary gas density of 10 $^{16}m^{-3}$. The important trend to note is the decrease in the refractive index effects as the saturation parameter is increased.

solutions and basic source geometry discussed in Section 3.2.1, previous work modeled the flow field from a collisionless source in these experiments [51]. These flow fields are shown in Figure 2.3.

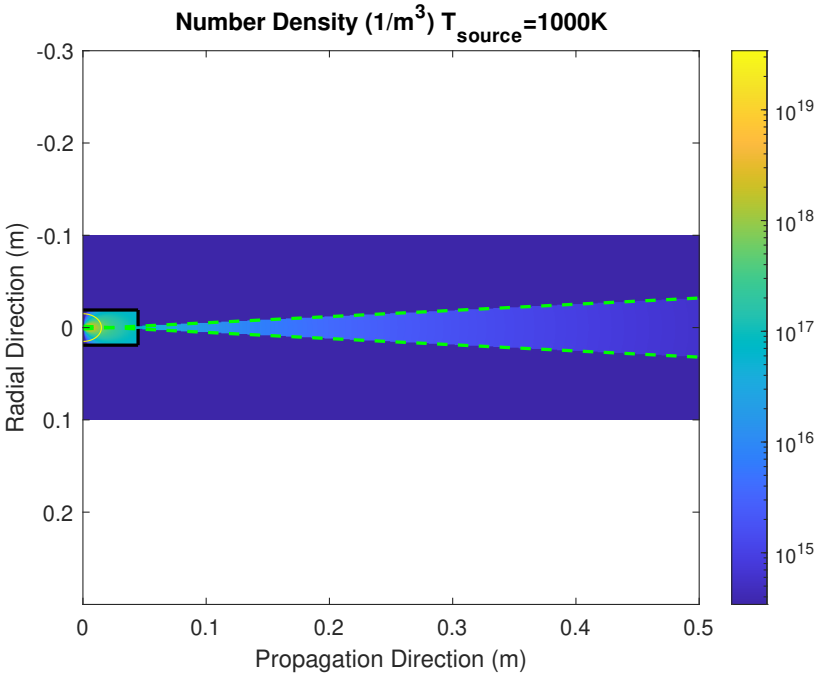

(a) Number density flow field

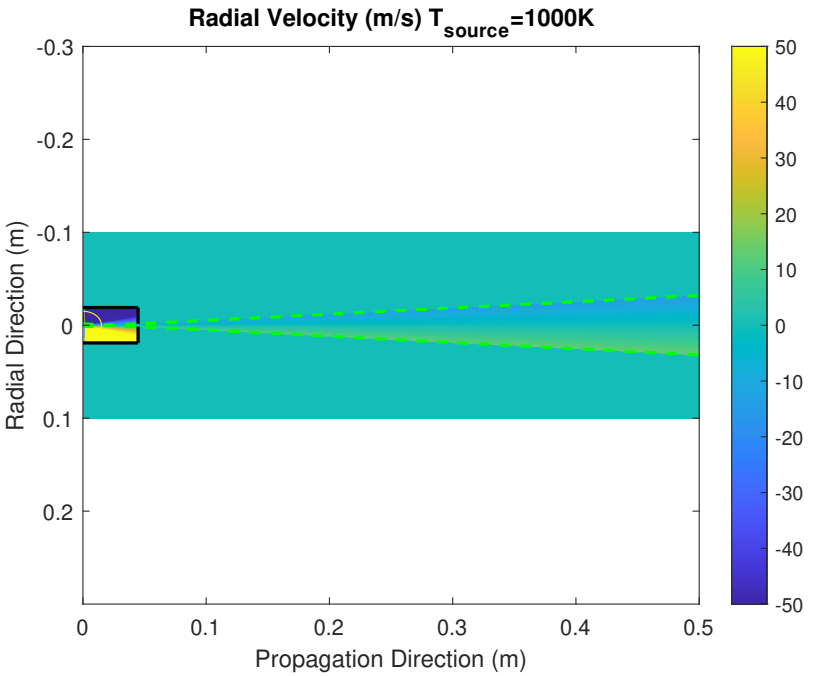

(b) Radial velocity flow field

Figure 2.3: Number density and radial velocity flow fields from a collisionless source using far-field equations provided by Cai and Boyd [1]. Green dashed lines show maximum subtended angle from circular emission source and flow-limiting shroud (black lines). Yellow line indicates the boundary beyond which the far-field assumption is valid.

For reference, a 45 mm separation between the circular Ø3 mm emission source and the flow-limiting shroud/aperture Ø3 mm hole, the maximum transverse velocity that can escape the shroud is approximately 14 m/s for an axial flow rate of 218 m/s. The transverse velocity can be equated to a most probable speed, C_{mp}, of atom with some temperature, T, by using Equation 1.5. This results in a temperature equivalent of approximately 1 K for the geometry described above. Therefore, if a red-detuned dipole potential (Section 2.1) has a depth greater than 1 K across this region of the flow, the whole jet will be confined within the potential, barring any collisions or heating events. It is important to note the geometric trade-off between divergence and mass flow rate in this effusive source configuration. If the shroud/aperture is moved closer to the emission source, more atoms flow through the shroud, however, there will be a larger divergence of the jet.

Another aspect of the flow behavior expected in the experiment is that which is discussed by Sanna and Tomassetti on the "bi-modal distribution" [52]. The bi-modal distribution is a combination of two primary groups of atoms with differing temperatures and densities which are co-propagating in the beam. This phenomenon occurs when the jet source exists in the quasi-free molecular regime and some atomic collisions may be present near the emission source. The atoms which experience a final collision within the emission source and propagate out are limited by the geometry of the source (i.e. flow-limiting shroud through-hole). This angle subtended by these "cold" atoms, θ_{cold}, can be described by,

$$\theta_{cold} = \tan\left(\frac{r_{source} + r_{shroud}}{z_{sep}}\right) \tag{2.15}$$

where r_{source} and r_{shroud} are the radius of the source and shroud through-hole, respectively. z_{sep} is the separation between the shroud through-hole and the emission source. Figure 2.4 illustrates the geometric influence on the vapor's divergence angle. The atoms that diverge with this angle are the coldest group in the bi-modal distribution.

The hot group of atoms in the bi-modal distribution stems from the imperfect free-molecular flow regime from the source emission resulting in atom collisions within the plume. These atoms

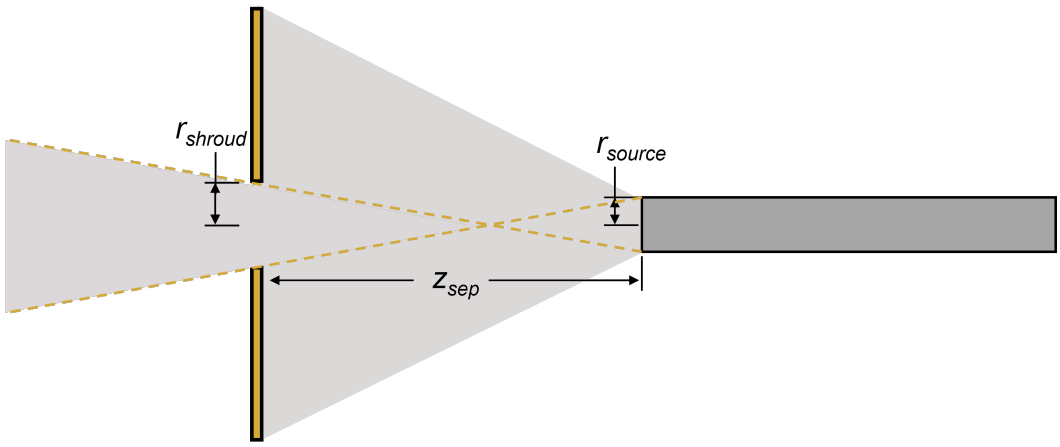

Figure 2.4: Flow emission diagram from an effusive source with a radius r_{source}. The central region of the emitted plume is then selected by a flow-limiting shroud with a passing radius of r_{shroud}. If the atoms do not experience further collisions in the plume, then the radii and separation distance, z_{sep}, determine the maximum divergence angle, shown as green dashed lines.

typically then travel on their ballistic trajectories from the point of the final collision. This new collision point can then be thought of as a proxy emission source. Since the separation distance between the shroud and final collision point is less than z_{sep}, these atoms will diverge with a greater subtended angle. The point at which these collisions diffuse from was evaluated by Beijerinck and Verster for supersonic beams [53]. In Sanna and Tomassetti's discussion, the expected perpendicular temperature variation between the two groups is $\frac{T_{\perp Hot}}{T_{\perp Cold}} \approx 25$ [52]. Therefore, if an exactly free-molecular flow source is not obtained, a bi-modal distribution can be expected with a colder group defined by a the geometry governed angle of the source and another hotter group which is 25 times hotter than the transverse temperature of the cold group.

2.4 Rubidium Absorption Spectroscopy

Alkali atoms are the primary candidate for this self-guided propulsion concept for a variety of reasons, including their short excited state lifetime, strong resonant transitions, and the ease of generating a magnetic dipole in the atom. Limbach and Hara completed a design study to determine which alkali candidates were the most useful for the propulsion concept [24]. Rubidium showed optimal behavior in several areas such as efficiency, spacecraft mass, and time remaining

in optical confinement. For these reasons, rubidium was chosen as the primary atomic species of interest and will be used throughout as the particle beam media.

The laser frequency and intensity at which a vapor will absorb light passing through it is dependant on several factors that influence the absorption lineshape. Of these factors, there are three primary contributors for a jet of atoms expanding into vacuum (neglecting pressure effects): the atom number density, temperature, and any line of sight velocity Doppler shift. These three factors manifest themselves in the absorption spectrum in different ways. The atom number density, N, is a direct multiplicative factor to the amount of absorption in the vapor. Therefore, the depth of an absorption feature relates to the number density of atoms in the probed region. The bulk velocity is also fairly trivial: for atoms traveling at some bulk velocity, $\vec{v_{\parallel}}$, if the propagation vector of the laser light, $\vec{\mathbf{k}}$, is not completely orthogonal to $\vec{v_{\parallel}}$, there will be a resultant Doppler shift in absorption spectrum. The Doppler shifted frequency, f_{shift}, from the static frequency, f_0, is calculated as,

$$f_{shift} = f_0 \frac{1}{1 + \frac{\vec{v_{\parallel}} \cdot \vec{\mathbf{k}}}{c}}. \tag{2.16}$$

From Equation 2.16, if the bulk velocity is directed toward the emission source of the laser, the atom will experience a blue shift (higher frequency). Whereas if the atom is traveling away from the laser source the laser source, it will experience a red shift (lower frequencies). Since the static resonant frequencies of the rubidium atom are well known, any deviation from these frequencies can be primarily attributed to a bulk velocity Doppler shift (in rarefied flows with little pressure influence). If the angle of the laser propagation vector to the propagation axis is known, then a single measurement of the Doppler shifted absorption spectrum can ascertain the axial velocity. Varying degrees of Doppler shift can be seen by modifying the angle between the laser propagation vector and axial velocity.

The atomic temperature influence on the absorption spectrum is slightly more involved and first requires an understanding of the absorption feature shape in frequency space. All atomic transitions experience natural broadening which is governed by a Lorentzian lineshape, $L(\omega)$,

$$L(\omega) = \frac{1}{2\pi} \frac{\gamma_N}{\Delta^2 + (\frac{\gamma_N}{2})^2} d\omega, \tag{2.17}$$

where γ_N is the natural linewidth which is related to the excited state lifetime. This natural broadening results in having some finite probability of an atom going to the excited state even if the excitation laser is not tuned exactly on resonance. Introducing temperature into the interaction yields another broadening mechanism: thermal Doppler broadening, which is modeled by a Gaussian lineshape, $G(\omega)$, in a static vapor,

$$G(\omega) = \frac{\lambda}{\sqrt{\pi} C_{mp}} \exp\left[- \left(\frac{\lambda \Delta}{2\pi C_{mp}} \right)^2 \right]. \tag{2.18}$$

Thermal Doppler broadening works similarly to the bulk velocity Doppler shift discussed above. For a static atomic vapor at a given temperature, there exist atoms traveling toward the laser emission source, away from the laser emission source, and orthogonal to the laser. These atoms can be considered to have a speed related to their temperature (Equation 1.5). Each of these atoms experience a Doppler shift depending on the orientation of their velocity relative to the light propagation vector. Thus, some atoms may experience a blue shift and others a red shift. The static vapor which is experiences sufficient collisions to be considered in equilibrium and has no constraints in the direction of motion of the atoms results in a Maxwellian velocity distribution function (VDF). The Maxwellian VDF corresponds to a Gaussian profile [25] in the absorption spectrum. To accurately model the combined absorption lineshape, a convolution of the natural (Lorentzian) and thermal broadened (Gaussian) spectra must be performed. This convolution produces the Voigt profile. An important item to note here is the interplay between temperature and density in the absorption spectrum. As the temperature thermally broadens the features, the integral of the lineshape must remain constant so the absorption depth of a significantly thermal broadened feature would decrease relative to a cold vapor of the same density. In other words, a cold and dense atom vapor would show very low transmission when the laser is tuned close to resonance, and a hot vapor with the same density would experience higher transmission near resonance than the cold vapor

but slightly less further away from resonance. Density, temperature, and bulk velocity produce detectable perturbations to the absorption spectrum that can be quantified using frequency tuned absorption spectroscopy to extract the transmission of the vapor as a function of laser frequency.

The rubidium atom has a particularly useful absorption spectrum at the $5^2S_{\frac{1}{2}} \longrightarrow 5^2P_{\frac{3}{2}}$ transition, also known as the D_2 transition. There are two naturally occurring isotopes of rubidium ^{87}Rb (27.83%) and ^{85}Rb (72.17%) with their D_2 central frequency < 80 MHz apart from each other. Each of these isotopes also have a ground state degeneracy of two and excited state degeneracy of four. These state degeneracies lead to hyperfine states in the transition. The hyperfine structure of the transition stems from the differing energies in the ground and excited states from the variation in the nuclear spin and electron angular momentum. This physically manifests by having two separate hyperfine ground states and four separate hyperfine excited states each with their own energies. The hyperfine states are denoted by the F quantum number. These state degeneracies lead to a total of 12 allowed dipole transitions which have sufficient frequency spacing that they can be differentiated in the absorption spectrum. The specific properties of the hyperfine transitions is provided by Steck [54, 55].

Isotope	Ground F State	Excited F State	Separation from Central Frequency (GHz)
85	2	1	1.657 636
	2	2	1.687 009
	2	3	1.750 409
	3	2	-1.348 720
	3	3	-1.285 320
	3	4	-1.164 680
87	1	0	3.969 603
	1	1	4.041 825
	1	2	4.198 765
	2	1	-2.792 858
	2	2	-2.635 917
	2	3	-2.369 265

Table 2.1: Hyperfine transition frequencies relative to the D_2 central frequencies for both respective isotope. ^{87}Rb central frequency is 384.230484469 THz and ^{85}Rb central frequency is 384.230406373 THz.

As shown in Table 2.1, the hyperfine structure of the rubidium atom is significantly dispersed in frequency such that, if the hyperfine peaks were visible in the spectrum, they could be discerned from one another. Each of these hyperfine transitions has their own relative strength factor that ultimately relates to the absorption depth at each hyperfine feature. The D_2 transition is of primary interest over the D_1 transition because of the absorption oscillator strength; for ^{85}Rb the absorption oscillator strength for the D_2 transition is 0.69577 and the D_1 transition is 0.34231. ^{87}Rb has very similar absorption oscillator strength ratios to the ones provided for ^{85}Rb. These absorption oscillator strengths correspond to a greater amount of absorption in the vapor for a given density at the D_2 transition than the D_1.

2.4.1 Saturated Absorption

Saturated absorption begins when the optical pumping rate to the excited state is greater than the total relaxation rate [49]. Upon saturation, the density of the excited state relative to the ground state approaches the ratio of the degeneracies of the two states. If the optical pumping power still increases, the medium will appear transparent as very little attenuation occurs relative to the strength of the laser and the vapor cannot absorb anymore photons. This behavior is utilized in saturated absorption spectroscopy (SAS) in order to resolve the hyperfine frequency locations in the absorption spectrum. An example of an experimental SAS setup is described in detail in Section 3.3.1. However, to explain the fundamental theory of operation, it is sufficient to say that a frequency tuning laser is divided into a high power pumping beam and a low power probe beam. A probe beam passing through an atomic vapor cell without the addition of a pump beam would simply experience the thermally Doppler broadened absorption spectrum corresponding to the density and temperature inside the vapor cell. However, if the pump beam is spatially overlapped with the probe beam, such that they interact with the same spatial ensemble of atoms, the probe beam will experience frequencies of increased transmission across the spectrum. The thermal Doppler broadening often dominates the spectrum compared to the natural broadening of the hyperfine features. However, once the pump laser is turned on, the hyperfine transitions of the atom vapor become saturated, meaning they can no longer absorb photons, which yields a

frequencies of greater transmission for the probe beam as it is not attenuated. If the pump and probe beam are counter-propagating, they interact with atoms of inverted velocities. In other words, if a probe beam is tuned to the red of resonance by some arbitrary amount that it interacts with the group of atoms traveling at some velocity, v, the pump beam which is counter-propagates interacts with the group of atoms traveling at $-v$ velocity. This interaction with two different atom groups occurs unless the laser is tuned directly on the resonance, which then allows for the pump beam to saturate that group of atoms which no longer absorb as much of the probe beam. With this technique, the very narrow naturally broadened hyperfine features can be seen. An example of a measured saturation absorption spectrum for rubidium is shown in Figure 2.5

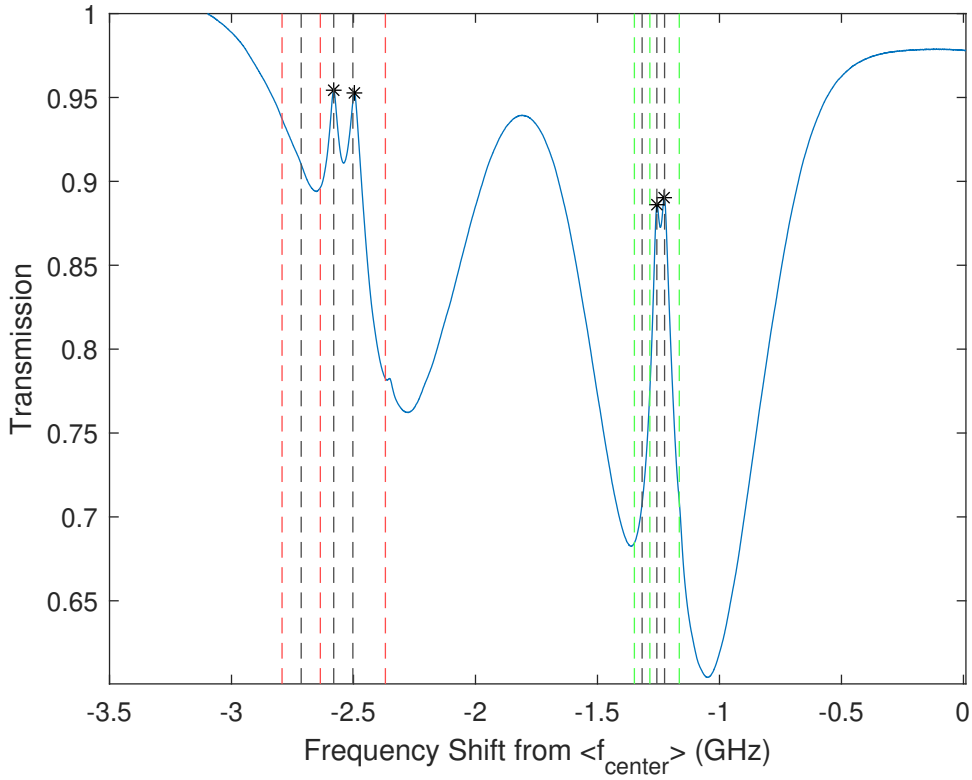

Figure 2.5: Saturated absorption spectrum for rubidium atom at D_2 resonance. Hyperfine transition frequencies of ^{87}Rb shown as red dashed lines, and ^{85}Rb hyperfine lines are shown as green dashed lines. Black dashed lines represent crossover resonance frequencies. The left major trough are the ^{87}Rb F = 2 ground state transitions and the right major trough are the ^{85}Rb F = 3 ground state transitions.

Figure 2.5 shows an artifact the particular SAS setup used to extract the spectrum called crossover resonances. Crossover resonant frequencies occur directly between two transitions from the same ground F state (e.g. halfway between F = 2 $\longrightarrow$ 2 and F = 2 $\longrightarrow$ 3). For the rubidium atom on the D_2 line, each ground F state can go to three allowed excited F states, resulting in three cross-over resonances per ground F state transitions per isotope. Each trough in Figure 2.5 is generated from the combination of six features (three hyperfine resonances and three crossover resonances). To understand how these crossover resonances manifest and result in an increased probe beam transmission, we must think of the experimental setup with a counter-propagating pump and probe beam. If the laser is tuned directly between hyperfine transition 1 and transition 2 (ranked in order of increasing frequency) and the spacing between the two transitions is less than the Doppler broadening, then the cross-over resonances can be seen [42]. While the laser is tuned directly between the two transitions, there exists two velocity groups of atoms, v and $-v$, which experience a blue shift and a red shift, respectively, and causes them to align with the resonant frequencies for transition 1 and 2. Which velocity group gets Doppler shifted to which transition is not important, except for the realization that the red and blue shift are opposite for the counter-propagating pump and probe beams. At this precise frequency point, both lasers are acting on the same two velocity groups (v and $-v$). Thus, the pump beam is able to saturate both transitions and allow greater transmission for the probe beam. The crossover resonances are an artifact of the experimental setup. SAS setups that remove these crossover resonances have been demonstrated [56]. However, since crossover resonances can be prominent features in the absorption spectrum and they also occur at very well known frequency values, they too can be used as a reliable frequency reference to determine the precise laser frequency during the experiment.

3. EXPERIMENTAL METHODS*

Before the combined laser and atom beam space propulsion concept can be used for deep space missions, ground experiments in laboratory-scale facilities must first demonstrate the self-guiding interaction. The theory and simulation of the combined beam propagation behavior has been the subject of extensive work by Limbach, Hara, and others [24, 57, 30, 29, 28, 58]. However, these simulations need to be validated with experiments to prove them as effective resources for predicting behavior of the space propulsion method. There are three main elements to the self-guided combined beam propulsion concept: combined beam emission, mutual propagation, and momentum transfer to the science spacecraft. The laboratory-scale experiments discussed primarily focused on developing and characterizing the emission in order to study the mutual propagation behavior with the overlapped laser and atom beam. The infrastructure built to study the combined beam is shown in Figure 3.1 and illustrates the need for four main areas in the experimental facility:

1. A method for generating the combined beam by spatially overlapping a laser with a rubidium vapor jet.
2. An area that conducts an analysis of the combined beam and allows this beam to propagate such that guiding effects can manifest. The data from this analysis will be used to validate simulations.
3. Apparatus for separating the combined beam back into the constituent systems such that the overlapped laser can be analyzed.
4. Extraction and analysis of the overlapped laser which will also be used to validate simulations.

This dissertation focuses on two distinct experiments: a rubidium jet source characterization study and an overlapped rubidium and laser beam experiment. While Figure 3.1 describes the

*Part of the information in this chapter is reported in "Characterization of an Effusive Rubidium Atomic Jet Source by Tunable Diode Laser Absorption Spectroscopy" by Morgan, H.P., Hodges, W.L., Jillapalli, R.D., and Limbach, C.L. 2021. *AIAA Scitech Forum*, Copyright 2021 by Texas AM University and reprinted with permission.

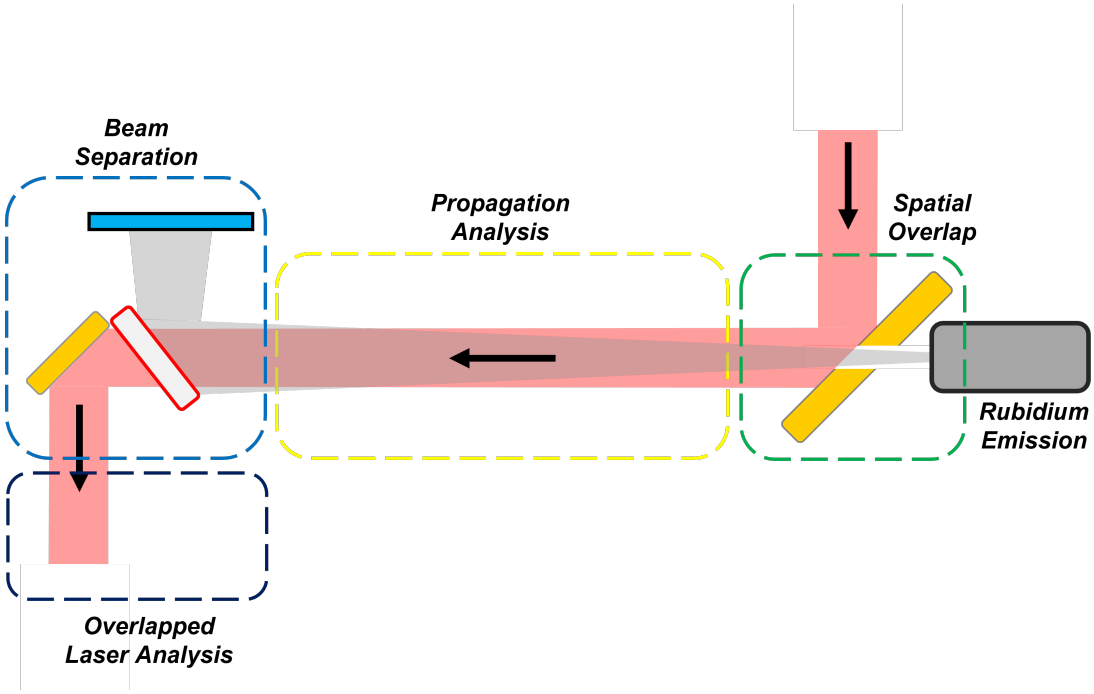

Figure 3.1: Proposed combined beam experimental architecture requiring a method for generating a jet of rubidium vapor, laser spatial overlapping infrastructure, a method for studying the combined beam as it propagates, and finally an apparatus for separating the two beams such that the overlapped laser can be analyzed.

architecture for the combined beam study, several elements remain the same across these experiments. For the jet characterization study, the spatial overlapping, beam separation, and overlap laser analysis infrastructure are all omitted. The jet characterization study serves as a risk-reduction predecessor to the combined beam experiment. This initial study also provided a test of the vacuum infrastructure and monitoring equipment, laser diagnostics, and rubidium jet source. From this initial study, many components of the experiment were modified to improve functionality in the overlapped beam experiment. The goal of the overlapped beam experiment is to vary the following input parameters:

- Laser input parameters:
  - Laser frequency
  - Laser power

  - Laser focal length

- Atomic vapor jet input parameters:
  - Emission divergence angle
  - Supplied electrical power to the source

While these input parameters are varied, the density and temperature distributions of the atom jet and the final overlapped laser intensity profile are extracted. In order to conduct the jet characterization and overlapped beam experiments, several critical components needed to be designed, manufactured, and tested. Each of the following sections will describe the component configuration for both experiments, where applicable.

3.1 Experimental Vacuum Chamber

The experimental facility housing the overlapped beam experiment is shown in Figure 3.2 and consists of four vacuum chambers attached in tandem. The primary octagonal chamber houses the atomic rubidium vapor source and the optics for spatially overlapping the laser beam with the atomic jet. The first laser diagnostic station is also located on the octagonal main chamber in an attempt to study the atoms close to the laser overlap. A 8" ConFlat (CF) Tee section and a 4-way reducing cross provide two additional laser diagnostic stations while having the added benefit of extending the beam propagation distance. Lastly, an 8" CF 6-way cross chamber is at the end of the tunnel section to house the beam decoupling mechanism and atomic beam dump. This 6-way cross section also houses several instruments to monitor vacuum systems such as the residual gas analyzer (RGA), thermocouples, and vacuum pressure gauge. The vacuum chamber configuration for the jet characterization experiment is similar to the one shown in Figure 3.2 except the Tee section was omitted and there was only one laser diagnostic station through the 4-way reducing cross.

3.1.1 Vacuum Pumping Equipment

The vacuum chamber shown in Figure 3.2 utilizes two turbomolecular vacuum pumps backed by a roughing pump to reach the ultra-high vacuum levels required for the experiment. This flow

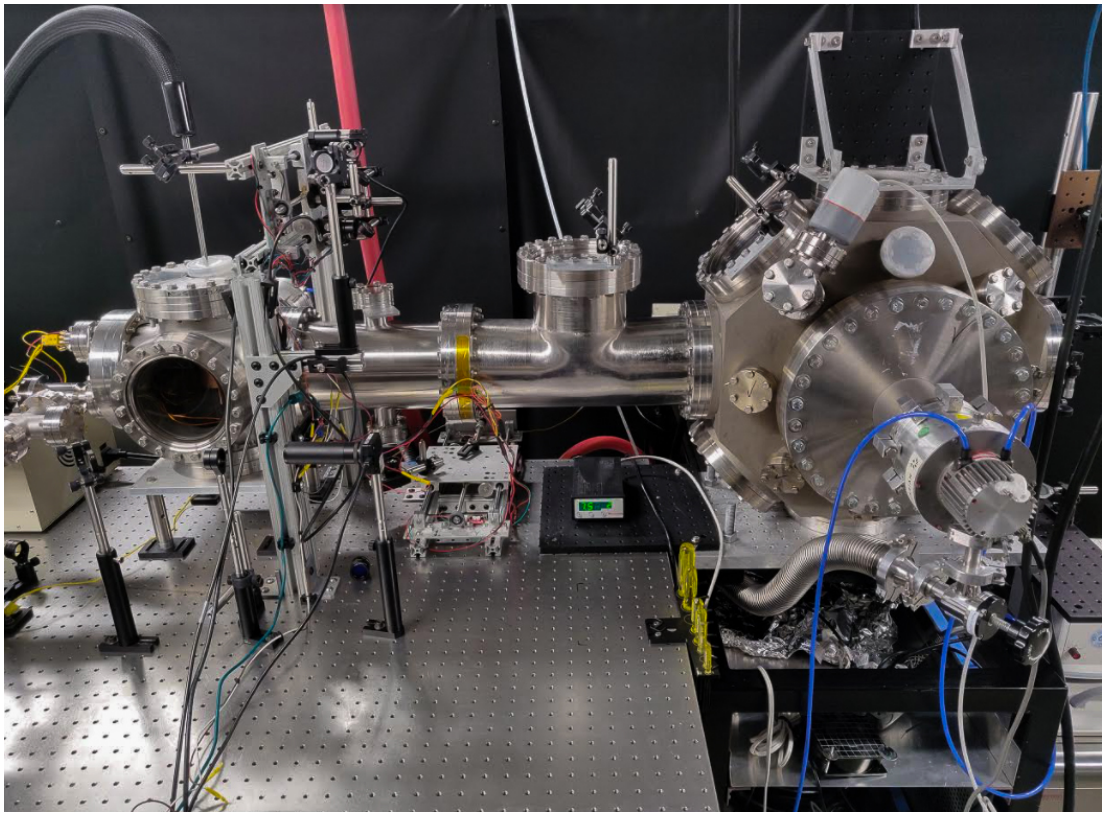

(a) Overlapped beam experimental chamber

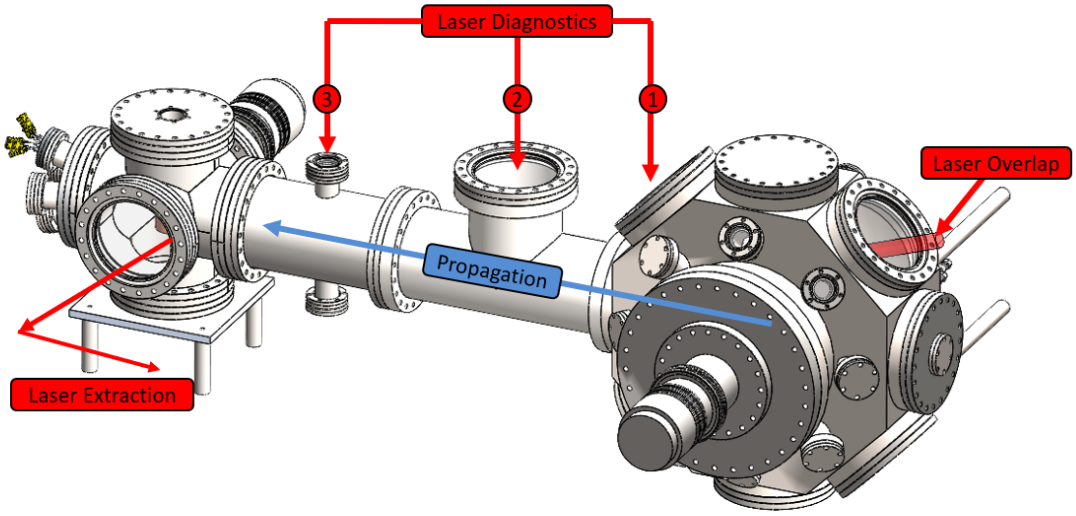

(b) 3D CAD rendering of the experimental chamber with illustrations for laser overlap and extraction and laser diagnostic stations

Figure 3.2: Experimental vacuum chamber for beam overlap, conducted in the octagonal main chamber, laser diagnostic study during propagation, and beam separation in the 6-way cross chamber on the left

diagram of pumping equipment and the dry air inlet purge system is shown in Figure 3.3. The Ebara EV-A10-3U dry rotary pump is used to initially bring the vacuum chamber to low pressure. Utilizing a roughing pump is necessary due to the turbo-pumps requiring <1 Torr chamber pressure before activation. The roughing pump has been shown to produce a base pressure in the chamber on the order of 10^{-2} Torr. Once the chamber has reached this lower pressure, the turbomolecular pumps can be engaged. The Varian V150HT and V250 turbo-pumps typically operate between 40-60 krpm and have been shown to produce a base pressure in the chamber of 10^{-8} Torr.

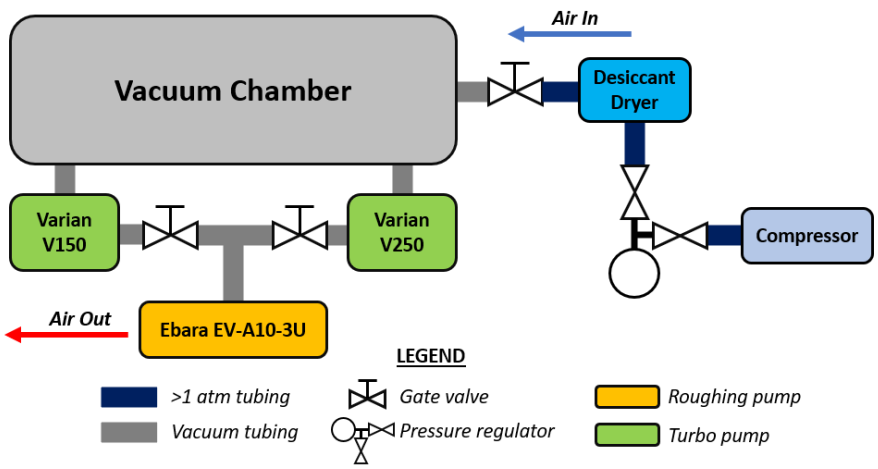

Figure 3.3: Vacuum facility flow diagram including vacuum side equipment and dry-air purge line hardware.

The air inlet system is critical for two reasons: dry air will allow oxygen to bond with rubidium atoms and passivate them, and it provides a method for safely bringing the chamber back up to atmospheric pressure. The first stage of this line utilizes the laboratory air compressors which have in-line dryers installed; this line provides air pressure at 8 bar. The air is then regulated down to 1 bar where it is then passed through an in-line desiccant dryer to further remove water vapor in the flow. Once the vacuum compatible gate valve is opened, this dry air can then flow into the chamber, oxidize the rubidium, and bring the chamber up to atmosphere. It is important to note the stringent requirement of drying the air prior to injection into the chamber. Moist ambient air contains water

vapor that could be sufficient enough to react with the volatile water-reactive rubidium and cause ignition.

3.1.2 Vacuum Monitoring Equipment

Several instruments are installed throughout the vacuum chamber to monitor the vacuum and critical systems. Due to consistent issues with ultra-high vacuum compatible pressure gauges, two gauges are used in the chamber simultaneously. One of the gauges is an Edwards Wide Range Gauge, capable of monitoring 1 atm down to 10^{-9} mbar. This gauge is installed on the primary octagonal chamber. The second gauge is a Granville-Phillips Micro-Ion ATM gauge with the same range as the Edwards gauge. The Micro-Ion gauge is installed on the 6-way cross region. This configuration of gauges offers the ability to calculate conductance between the octagon and 6-way cross, which is useful for longer propagation experiments where the flow might become limited by conductance. However, the Edwards gauge continually entered a failure state during testing and would not yield proper readings. Therefore, the Micro-Ion gauge was the primary pressure measurement. This gauge failure is predicted to stem from heat transfer fluid contamination from a leak in the vacuum side cooling lines causing oil deposition on the instrumentation of the pressure gauge.

Another useful instrument installed in the chamber is a Stanford Research Systems Residual Gas Analyzer (RGA). This RGA utilizes a quadrapole mass analyzer to determine the partial pressure of gasses in the chamber as a function of their atomic mass. The RGA is primarily useful during chamber construction to conduct helium leak testing. The analyzer can be set to continually monitor for 4 au, which corresponds to helium, and an operator can blow a low velocity jet of helium on the vacuum flange seals. Any leaks in the vacuum seals will allow helium to pass through and reach the RGA. The RGA can be used to measure gasses from 1-100 au which yields another method of analysis during the experiment by setting the RGA to monitor for rubidium. It is critical that rubidium which is not in the primary jet be immediately condensed on chilled surfaces to prevent it from entering the propagation region and contaminating diagnostic measurements. Setting the RGA to monitor for 85 and 87 au, the two naturally occurring rubidium isotopes, will quantify

the partial pressure of these gasses during testing. This information can be used to determine the effectiveness of the condensation surfaces.

3.2 Testing Hardware

While Section 3.1 discussed the enclosure and basics of the vacuum facilities, this section will discuss the unique equipment that was developed to generate an atomic rubidium jet source, manage the rubidium at the end of the propagation, spatially overlap a laser with the atomic beam, and separate the combined beam for analysis.

3.2.1 Atomic Rubidium Jet Source

The rubidium atomic jet source has been the subject of immersive study throughout the development of these experimental facilities. Between the jet characterization study and combined beam experiment, the sole difference in the atomic jet source has been the mounting method for the rubidium getter, a component which houses the metal and heats it to produce the rubidium vapor. The principle jet source design was inspired from the work by Moore et al. [59]. Both sources utilize a rubidium getter cartridge and a chilled condensation shroud. The rubidium getters used in this experiment are from AlfaVakuo in a 3C configuration. The "3C" code refers to a getter that is 3 mm in diameter and has a front and back tab that extend downward. AlfaVakuo offers different rubidium fill quantities. For the jet characterization study, a 50 mg fill was used while the combined beam experiment utilized a 250 mg fill.

3.2.1.1 Condensation Shroud

The rubidium getter emits a large solid angle plume of rubidium atoms. However, the atoms outside of a small central cone are not viable for use in the experiment, as their divergence is too large to be confined in the dipole trap. The lower-divergence central cone of atoms has a low transverse velocity (temperature, see Equation 1.5). The optical dipole trap potential predicted for the experiments is sub-Kelvin in depth. Any atoms with a larger transverse kinetic energy than the dipole potential depth will not be effectively confined by the overlapped laser beam. To prevent rubidium accumulating as a background gas in the chamber, it is necessary to only allow a small

region of interest to propagate. The chilled condensation shroud has a Ø3 mm through-hole on axis to allow the central cone of atoms to propagate through while condensing any atoms that collide with the walls. Figure 3.4 shows the condensation shroud during initial open air testing prior to vacuum integration.

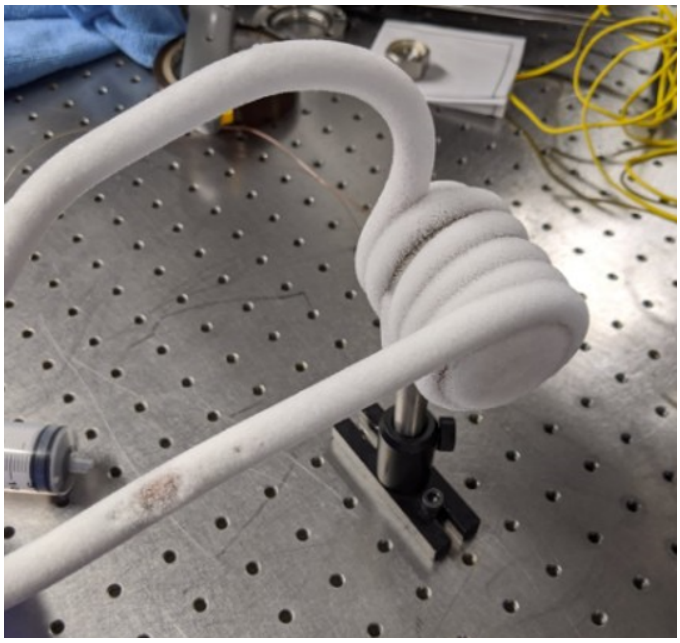

Figure 3.4: Actively pumped chilled condensation shroud shown in open air testing prior to installation. A refrigerated circulator flows low temperature silicon-based oil through the copper lines brazed to the body to reach temperatures as low as -50°C

A Thermo Scientific AC200 Glacier G50 refrigerated circulator is used to actively pump low temperature fluid throughout the copper tubing which is brazed to the cylindrical body of the shroud. Copper is utilized to increase thermal conduction through the shroud and into the fluid. The G50 is typically set to a temperature of -50°C during testing but has the added benefit of also being able to heat the fluid to above ambient temperature. Raising the temperature of the working fluid provides the option to melt the condensed rubidium in the shroud to ease clean-up, if desired.

3.2.1.2 Jet Characterization Study Rubidium Source

The rubidium jet source for the jet characterization study, shown in Figure 3.5, was the first iteration of the effusive source. This experiment served as a test of the use of the rubidium getter as the primary source, the condensation shroud, and mounting method for the getter. A primary goal of the design for the jet source was to align the jet's central axis with that of the propagation region of the chamber. This alignment centralizes the laser diagnostic method to the jet axis. To start mounting the source, a pair of custom fabricated struts is attached via vented bolts to one of the primary 14" CF flanges on the face of the octagonal chamber. The source-side infrastructure uses these struts as the primary attachment point. It is necessary in the design to include methods for position adjustment of the shroud and rubidium getter. The getter axis and shroud axis need to be aligned as well to maintain the central region of the plume exhausted by the getter as the region that propagates into the chamber. Another constraint for the system is the need to maintain the temperature differential between the getter and the shroud. The shroud must maintain at a low enough temperature (-30°C [59]) to achieve a significant sticking probability when atoms collide with the wall . The getter source is expected to reach up to 1000 K. With this temperature range between close proximity components, it is ideal to maximize the path length for thermal conduction in an attempt to make radiation the primary form of heat transfer. The alignment and temperature constraints are the reason behind two separate alignment systems for the shroud and getter which are shown in an exploded view in Figure 3.5

The rubidium getter is activated via electrical resistive heating, therefore passing a current through the getter will result in a rise in temperature. The alligator clip and ring terminal connector shown in Figure 3.6 complete the electrical circuit through the getter and route out of the vacuum chamber through an electrical feedthrough into a constant current power supply. The getter vendor, AlfaVakuo, supplied data for the relationship between current supplied to the getter and resultant temperature for an optimally mounted getter. The getter is clamped in place via a vacuum-compatible Macor ceramic V-block. Two button head cap screws with a compression spring between the head and the top Macor block provide the clamping compression force while

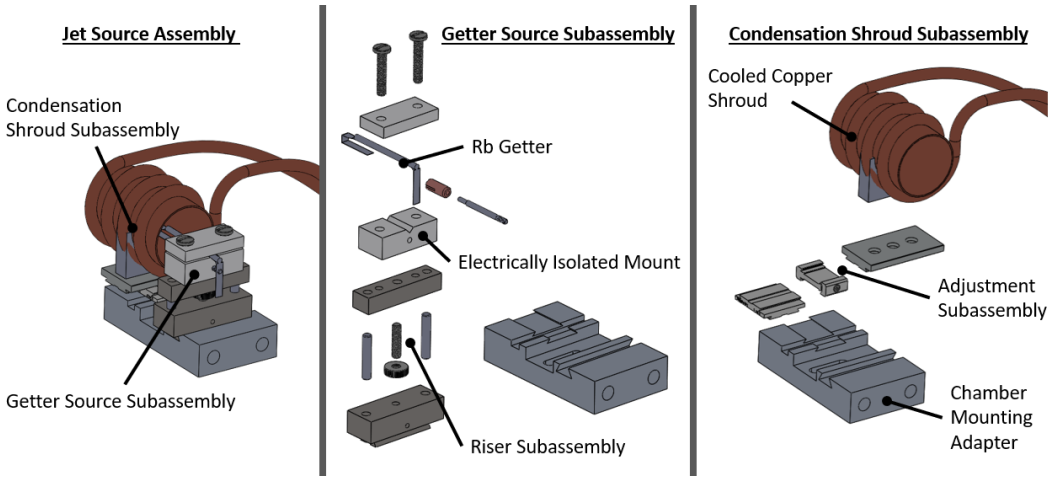

Figure 3.5: 3D rendering of the jet characterization atomic rubidium jet source. Left: collapsed assembly showing in-use configuration. Middle: rubidium getter subassembly with method for adjusting the getter on all three primary axes. Right: condensation shroud subassembly with two axis degree-of-freedom.

still allowing room for thermal expansion without cracking the ceramic. The rationale of mounting the getter via the cylindrical body was to rigidly control the central axis of the source to ease alignment with the shroud.

The results from the jet characterization study, discussed in detail in Chapter 4, showed that the method of holding the getter, by clamping the body with a ceramic block, thermally sapped the reservoir. This ultimately led to a stark difference between the manufacturer's specified mass flow rate as a function of temperature and what was measured during the experiment. In other words, more current was needed to produce the same mass flow that the manufacturer expected. These findings spurred the change in getter mounting for the combined beam study jet source.

3.2.1.3 Combined Beam Study Rubidium Source

Applying lessons learned from the initial effusive source characterization study, a new source was designed that utilizes the tabs of the getter for mounting. Mounting via the getter tabs instead of the main body provides less thermal sapping of the reservoir. However, this new mounting yields additional degrees of freedom that complicate alignment. This new source design, shown in Figure 3.7, uses two stainless steel electrodes with pronged ends and tapped holes such that a screw

Figure 3.6: First iteration of the atomic rubidium source which utilized a clamped rubidium getter, chilled condensation shroud, and dovetail alignment blocks.

can keep the getter tabs locked in place. To prevent electrical shorts, the electrodes are insulated with PTFE plastic bushings in the stainless steel housing block. The PTFE is a vacuum-compatible plastic and electrical insulator. To clamp the electrodes in place, two PEEK plastic screws are used per electrode which clamp on a machined flat section of the electrode.

It is important to elaborate on the drawback of this design when compared to the previous iteration. Moving from using a rigid mounting (body mounted) to a greater degree of feedom mounting method (tab mounted) complicates the alignment between the getter and the shroud. The vertical height of the getter can be varied by the height adjustment screw, shown in Figure 3.7, but also where along the length of the tab the getter is clamped. In addition to the height variation, the getter can have some inherent pitch due to inconsistencies with clamping of the tabs between the front and back. In other words, if the front tab is clamped higher up than the back tab, the mouth of the getter may appear centered, but this pitch would yield a skewed atomic jet emitted from the shroud. Figure 3.8 shows the visual inspection for alignment between the getter mouth,

the shroud through-hole, and the beam overlapping mirror through-hole.

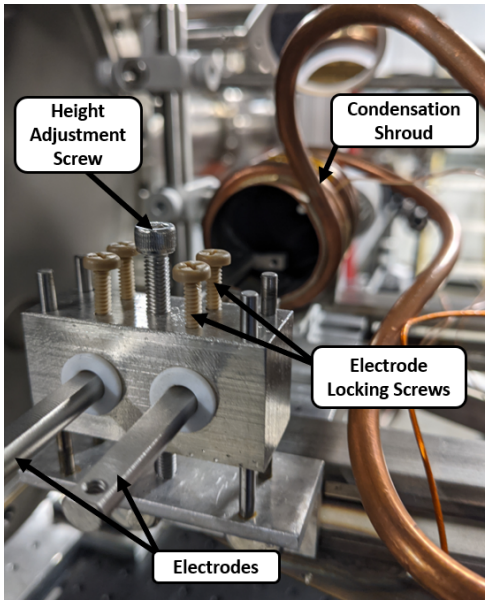

Figure 3.7: Combined beam study atomic rubidium source utilizing a new method of getter mounting with pronged electrodes passing through a riser block. Electrodes are adjustable in insertion depth into the shroud, thus providing adjustment in the solid angle of extracted rubidium jet.

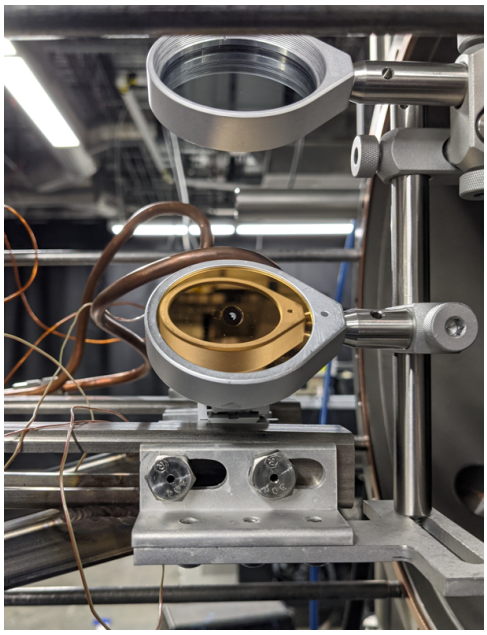

Figure 3.8: Alignment of rubidium getter, condensation shroud pinhole, and through-hole mirror. It is necessary to have the central axis of all three of these components co-linear to produce a more uniform atomic jet.

3.2.2 Atomic Beam Dump

The atomic beam dump plays a critical part in the experiment: condensing the rubidium atoms in the jet at the end of the experiment. Without a centralized location for the emitted rubidium to condense, this vapor would fill the vacuum chamber and contaminate the laser diagnostic measurement. The goal of the design of the beam dump is to optimize atoms sticking probability to the surface of a plate obstructing the flow. To accomplish this, an IP-60 Immersion Probe Chiller is used in conjunction with an ethanol fluid reservoir to create a heat removal system. A vacuum-side copper plate is then mechanically fixed to the fluid reservoir to conduct heat away from the plate. This system is shown in Figure 3.9 and Figure 3.10. Since the heat flux from the atoms condensing on the copper plate is minimal, the system is able to be passively chilled (fluid is not pumped directly to the hardware), as opposed to the condensation shroud which sees a direct, high-intensity radiative heat load from the getter during activation and needs to be actively pumped with coolant.

This atomic beam dump design has been tested individually to identify the time required to

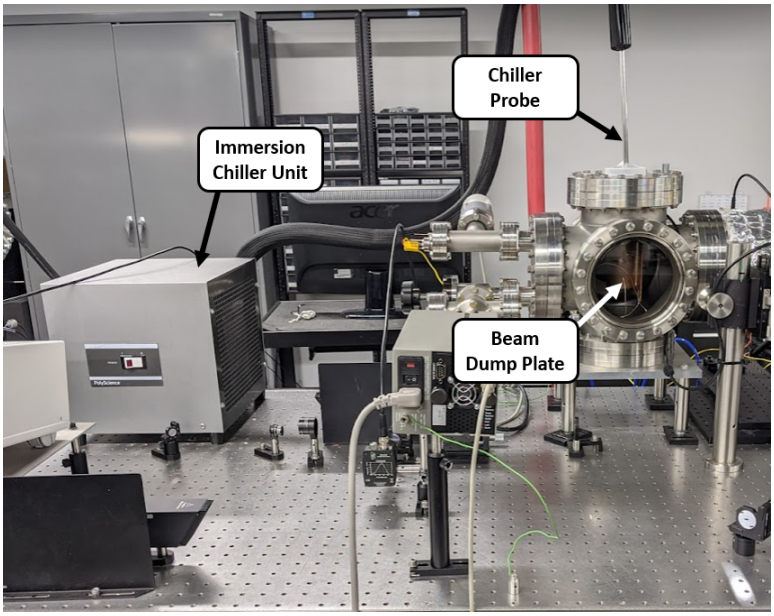

Figure 3.9: Atomic beam dump chiller system using an IP-60 immersion probe chiller immersed in an ethanol fluid reservoir and conducting heat from a vacuum-side copper plate.

reach an approximate steady state temperature; this temperature vs. time plot is shown in Figure 3.11. From Figure 3.11, the vacuum-side copper plate reaches a steady state temperature of -40°C after about 30 minutes of run time.

For the overlapped beam experiment, a slight modification was made to the atomic beam dump due to the addition of the combined beam decoupler, which will be described in detail in Section 3.2.4. To accommodate the rubidium reflected from the heated beam decoupler system, an orthogonal wing is brazed to the side of the plate. This new configuration is shown in Figure 3.12.

3.2.3 Laser Beam Overlap

To demonstrate a mutual guiding effect, a high power Gaussian laser must be generated and spatially overlapped with a co-propagating atomic jet of rubidium atoms. This section will discuss the overlap of the laser with the rubidium source discussed in Section 3.2.1.3. Generation of the overlap laser is shown in Figure 3.13. The laser is first generated with a continuous wave Ti:Sapphire M Squared Laser System (utilizing a Solstis and Equinox unit) tuning about the rubid-

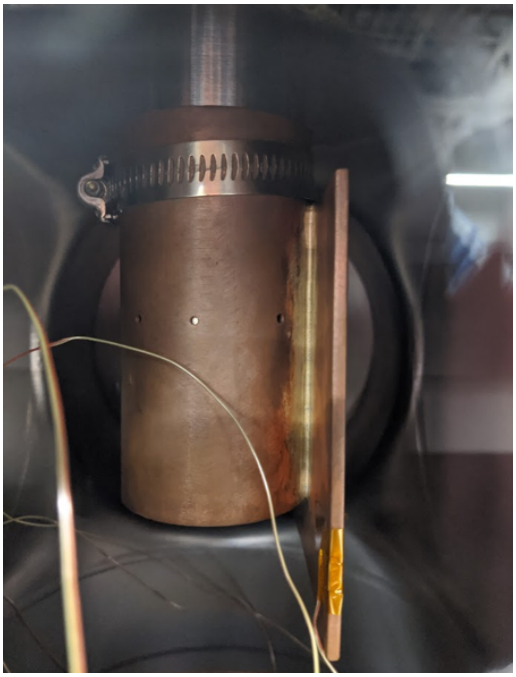

Figure 3.10: Side profile of installed atomic beam dump consisting of a copper plate brazed to a split section of copper tubing clamped to a stainless steel fluid reservoir. The copper plate is kept at sub-zero temperature to condense rubidium vapor on contact.

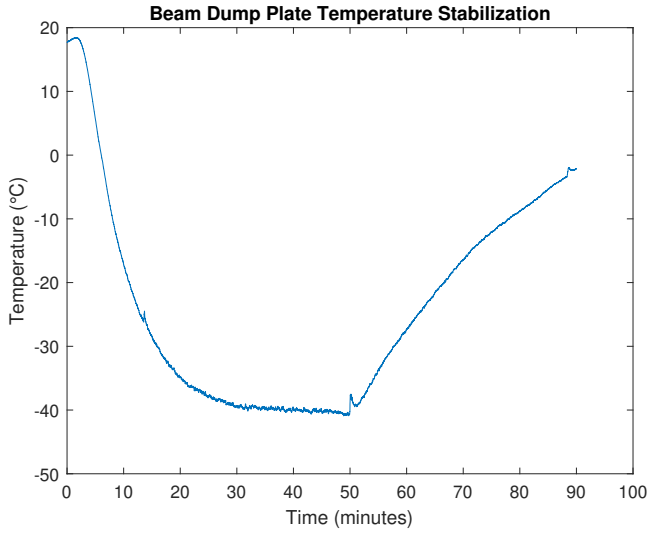

Figure 3.11: Temperature vs time plot for the atomic beam dump. The immersion probe chiller unit is turned on at 2 minutes and turned off at 50 minutes. The plot shows the steady state temperature occurs at approximately -40°C and reaches this point at about 30 minutes of run time.

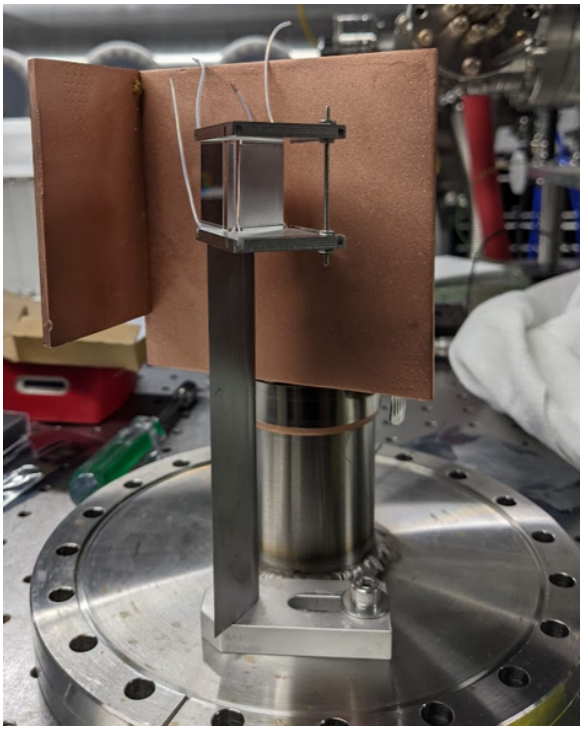

Figure 3.12: Second iteration of the flat plate atomic beam dump. The plate is modified with a secondary orthogonal wing to catch rubidium atoms reflected off of the heated beam decoupler.

ium D2 resonant frequency, with a maximum output power of 10 Watts, and a beam diameter of approximately 1 mm. After emission, this beam is sent to a combined half-wave plate and polarized beam splitter to vary the power directed to the experiment. The reflected beam is sent to a laser sampling system which uses a fiber-coupler to direct the beam to a HighFinesse wavelength meter (Type WS7). During the experiment, the wavelength meter is conducting a dual measurement to record the wavelength of both the overlap and laser diagnostic beams. While the diagnostic laser frequency is measured with a precise saturated absorption technique, discussed in Section 3.3.1, it is co-recorded in the wavemeter as a point of reference in the event of some inherent offset of the wavelength meter. After the polarizing beam splitter, the laser is directed to an expansion telescope which produces a collimated beam with a waist of approximately 20 mm. The beam is not expanded to the final desired size at this point in order to reduce cost by using standard Ø25 mm optics for the majority of the beam routing. The next stage utilizes another beam expansion telescope with one of the plano-convex lenses mounted on a translation stage. By varying the po-

sition of the lens, the post-expansion laser beam is no longer collimated and this focal point can be adjusted to various points in the jet propagation and used as a variable for study.

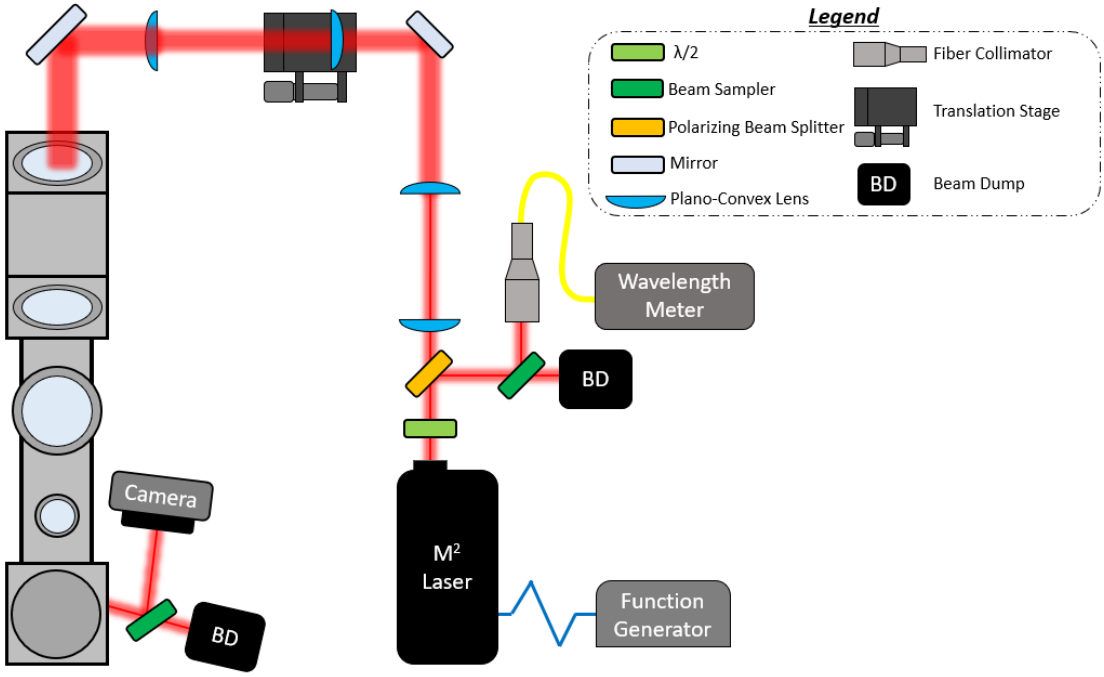

Figure 3.13: Top view of overlap laser diagram for all hardware that is external to vacuum. The beam is initially generated with a M Squared laser system which is frequency tuned via an external function generator. This beam is then sampled to send to a wavelength meter to measure the output laser wavelength. The beam is then redirected and sent through a series of two expansion telescopes, the last of which is adjustable such that the resulting focal point of the resultant beam can be varied inside the vacuum chamber. Lastly, the laser is extracted and analyzed with a CMOS camera.

The distance at which the overlapped laser comes to a focus is an important metric because at the focal point, the laser intensity is greatest, thus the resulting dipole potential is also at a maximum at that point. If the overlapped laser is collimated, the dipole potential will remain constant during propagation. For a focusing beam, the dipole potential will gradually increase as it propagates, but the area of atoms being influenced decreases. This trade-off is an area interest for this study and future experiments.

Spatially overlapping the atomic rubidium jet with the laser beam such that the two systems

co-propagate is conducted with a specialized mirror. This mirror includes a Ø6 mm through-hole drilled at a 45° relative to the surface and the exit hole is centered on the optically coated face. The mirror is gold-plated to provide good reflectance in the near-infrared wavelength range. This mirror can be seen in Figure 3.14 with an additional redirecting mirror above it. The redirecting mirror is required if the laser incident to the overlapping mirror is non-orthogonal to the propagation axis. Figure 3.2 shows the position at which this overlap laser is introduced into the vacuum chamber which illustrates the need for the secondary mirror in the vacuum-side overlapping optics.

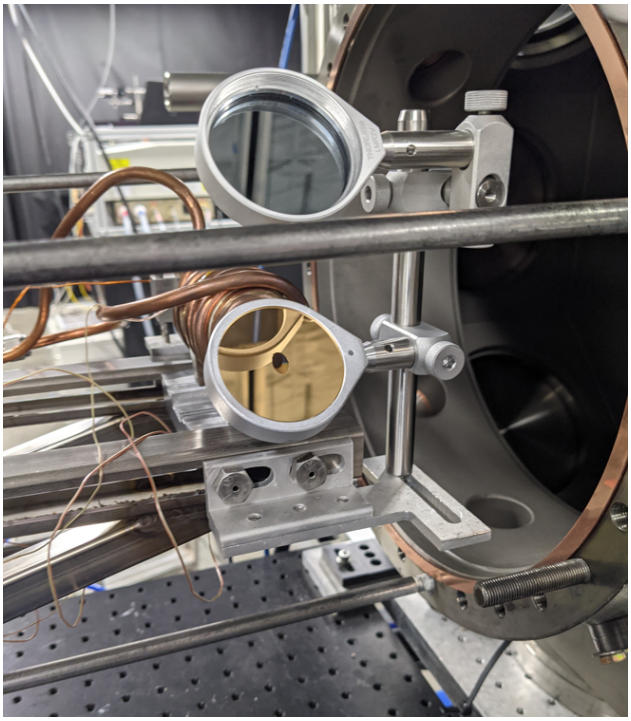

Figure 3.14: Vacuum-side laser overlapping optics. The lower gold-plated mirror is the primary overlapping mirror with a through-hole for the atomic vapor to pass through. The upper mirror is a protected silver mirror to redirect the incoming beam orthogonal to the propagation axis. Both mirrors are 50 mm in diameter and mounted with vacuum-compatible optomechanics.

An additional consideration for where to position the focal point of the overlap beam now comes from the power loss associated with the overlapping mirror through hole. If the laser is focused very close to this mirror, a greater portion of the laser beam power is removed by the Ø6

mm hole. This has the potential to greatly reduce the dipole force as the highest power region of the beam is removed. It may be necessary for future work to develop a method pre-conditioning the overlapped laser into a donut shape via axicon pair optics such that the power lost to the overlap mirror through hole is minimized.

The laser profile after the overlapping mirror can be seen in Figure 3.15. The laser is aligned using the paper template shown in Figure 3.15. The template is generated using the 3D CAD models to identify the central axis of the chamber. This alignment method can be used to solve two adjustments: the laser alignment with the overlapping mirror and the orientation of the mirror to the central axis of the chamber. The latter of these adjustments is quite trivial, with the goal being to have the laser centered in the cross point of the two dotted lines in the template. The alignment of the laser relative to the overlapping mirror manifests as the position of the circular shadow in the laser beam. The laser regions around the shadow should be uniform, indicating the central region of Gaussian beam is clipped. Additionally, the shadow should be centered in the resulting beam profile. With all three of these checks passed, a uniform starting overlapped laser profile can be assumed and the combined beam decoupler will be mounted directly in the center of the laser propagation.

The power of this overlap laser can be varied to evaluate the effects of the dipole force or the refractive guiding. To evaluate the effect of the dipole potential on the atom jet, it is beneficial to use maximum laser power. However, for quantifying the effects of the refractive index of the atom jet on the laser, it is necessary to reduce the beam power such that Beer-Lambert attenuation and laser profile perturbations are visible.

3.2.4 Combined Beam Decoupler

The final component of the overlapped laser experiment hardware is the combined beam decoupler. This system provides a novel aspect to the field of study. The overlapped laser profile after co-propagation with an atom jet has not previously been analyzed. The combined beam decoupler has the requirements of receiving a high intensity laser beam overlapped with an atomic jet of rubidium atoms. The goal of the decoupler is to then redirect those atoms to the atomic beam dump,

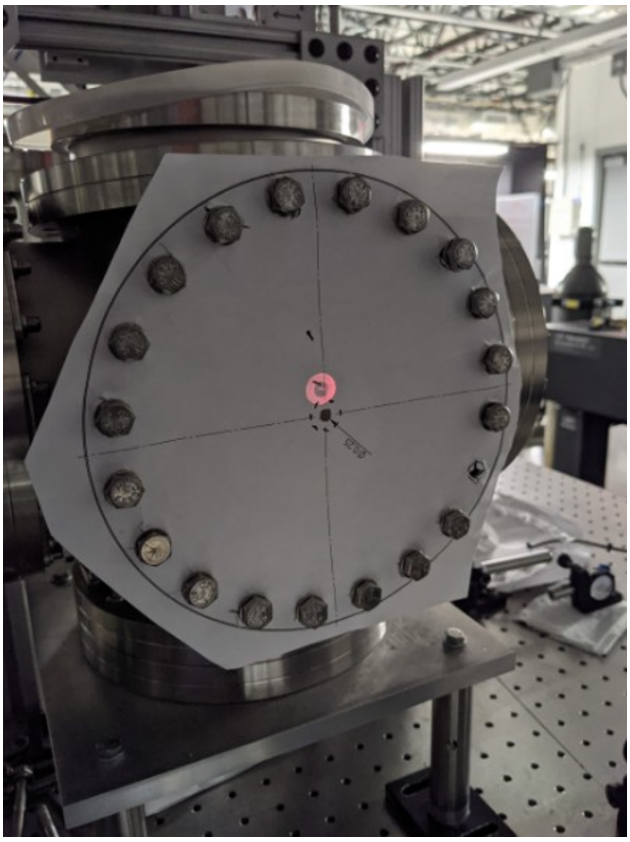

Figure 3.15: Overlap laser alignment process showing the propagating laser profile without the influence of a rubidium jet. The donut laser profile is created through the loss of the central region due to the overlap laser through hole. Without the beam dump and combined beam decoupler system installed, the laser is directed through the entire chamber. Thus a template can be used to align the laser with the central axis.

described in Section 3.2.2, where the atoms can condense. In tandem, the decoupler must simultaneously route the overlapped laser out of the vacuum chamber for analysis. The chosen design for conducting this is shown in Figure 3.16. The beam decoupler uses a heated optical prism to prevent rubidium condensation and allow light to transmit through, experience total internal reflection on the back leg and transmit out of the hypotenuse side. The reflected atoms are then directed to a slightly modified version of the atomic beam dump, which is discussed Section 3.2.2.

The beam decoupler is centered about a UV fused silica right-angle prism (Thorlabs #PS611) heated by metal ceramic resistive plate heaters on the top and bottom faces (Thorlabs #HT24S2). A custom mounting system is designed to minimized cross sectional area in the rubidium flow

such that the atoms will still hit the primary face of the chilled atomic beam dump rather than relying on the newly added wing to catch and condense all the atoms. The prism mounting system includes a tapered mounting sting that positions the prism directly in the center of the flow. This manufactured beam decoupler is shown during an open-air test in Figure 3.17.

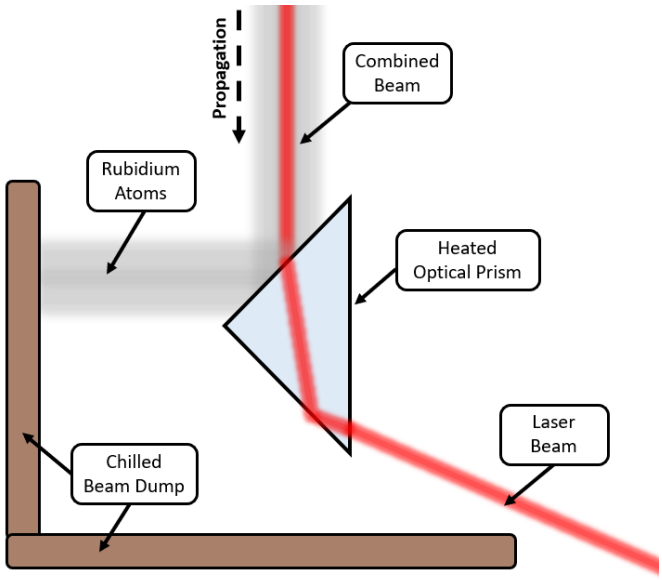

Figure 3.16: Simplified diagram of method for separating the spatially overlapped atom and laser beam using a heated optical prism to reflect atoms and reroute the laser.

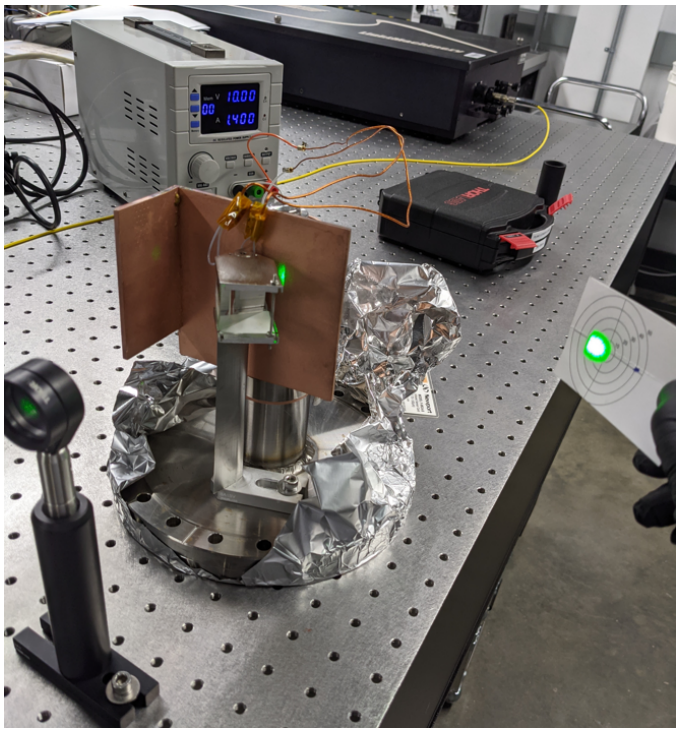

Figure 3.17: Simplified diagram of method for separating the spatially overlapped atom and laser beam using a heated optical prism to reflect atoms and reroute the laser.

It is important to note here the dependence of the refractive index of UVFS on temperature, approximately $10^{-5\circ}C^{-1}$ [60]. Due to heating effects from both plate heaters, the optical prism will experience both an average temperature increase as well as a thermal gradient across the height of the prism. This non-uniformity in the refractive index will induce distortions in the laser wavefront. However, these effects can be accounted for with a baseline measurement by passing the laser through the heated prism in vacuum without the influence of a rubidium jet. The average temperature increase in the prism results in a bulk translation of the laser beam output due to the changing internal refraction angles inside the prism.

3.3 Laser Diagnostics

Studying the atomic jet during propagation requires a non-intrusive method of evaluation. Previous literature has used a hot-wire detector to measure the atomic density profile [31]. This hot-wire detector cannot be used in this experiment because it would impede the path of the laser

and terminate or redirect the atoms out of the jet. For this reason, a tunable diode laser absorption spectroscopy (TDLAS) laser diagnostic technique is utilized to characterize the atomic jet. Additionally, to properly analyze the data from the TDLAS measurement, it is necessary to provide a frequency reference while the diagnostic laser is tuning. To achieve this laser frequency measurement, a saturated absorption spectroscopy (SAS) setup is used from a pick-off of the diagnostic laser. The diagnostic laser chosen for this experiment is a Toptica TA Pro 780 amplified tunable diode laser with a functional range from 765-795 nm. This laser is ideal for the rubidium D2 resonance at 780.2415 nm. Lastly, due to the overlapped laser tuning about the atomic resonance, the final laser profile provides valuable insights into the parameters of the atoms in the jet and will be discussed in detail.

3.3.1 Saturated Absorption Spectroscopy

The measured absorption spectrum in the experimental chamber is thermally Doppler broadened and potentially bulk Doppler shifted, therefore there is no method for discerning a true frequency scale for this absorption measurement on its own. A precise and accurate frequency axis for the absorption diagnostic is critical to extract the proper density and temperature of the atoms. Utilizing a pick-off from the diagnostic laser, the beam is frequency measured in real time using saturated absorption spectroscopy (SAS). The SAS setup, shown in Figure 3.18, takes an incoming laser beam, diverts it into two low power probe beams and a high power pump beam which counter-propagates relative to the two probe beams. These probe and pump beams are separated via polarization optics such that the power ratio can be tuned and the optics that loop the pump beam can transmit the probe beam. All beams travel through a vapor cell of the same atomic species being studied in the experiment, which is rubidium. The pump beam is spatially overlapped with one of the probe beams to deplete the ground state for this transition. After the vapor cell, both probe beams are directed to a photodiode balance which subtracts the two signals.

Section 2.4.1 discusses the fundamental physics behind the prominence of the hyperfine and cross-over resonance peaks in the saturated absorption spectrum. These hyperfine lines and cross-over resonance locations provide Doppler-free peaks at at well-known frequency locations.

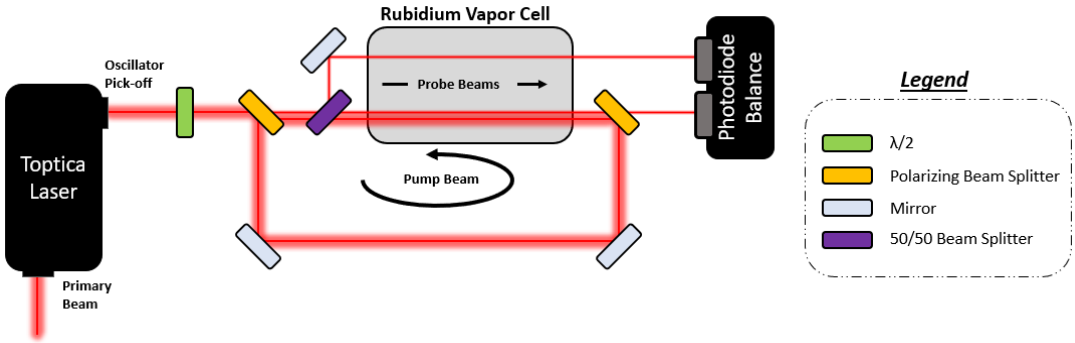

Figure 3.18: Diagram of saturated absorption spectroscopy diagnostic for rubidium. The laser is split into a high power pump beam and two equal power probe beams. One probe beam is spatially overlapped with the counter-propagating pump beam, therefore this absorption profile will appear saturated. The other probe beam is the unsaturated absorption profile. By using a photodiode balance, these two probe beams can be compared and the hyperfine features of the transition can be extracted and used as a well-known and precise frequency reference for the laser.

By using the SAS from a pick-off of the diagnostic laser, these precise hyperfine peaks can be used to generate a frequency scale that directly applies to the TDLAS diagnostic measurement. Section 3.4 will discuss how the saturated spectrum measurement is analyzed to generate the frequency axis. The primary considerations for the SAS system is that the probe beams maintain a relatively low power (well below the saturation intensity of the atomic species) and the pump beam has sufficient power to deplete the ground state. If the diagnostic laser is running at high power, this may require the use of ND filters prior to the SAS setup.

3.3.2 Tunable Diode Laser Absorption Spectroscopy

The primary parameters of interest for these experiments are the density and temperature distributions as well as the axial velocity of the atoms in the jet. Tunable diode laser absorption spectroscopy (TDLAS) uses a laser tuning about a resonance of the rubidium atom to quantify the amount of absorption compared to laser frequency. The measured absorption spectrum will be altered by any velocity relative to the laser propagation vector, path length in the vapor, vapor density, and atom temperature.

3.3.2.1 Jet Characterization TDLAS

For the rubidium jet characterization study, the TDLAS optics are shown in Figure 3.19. The base setup included a method for attenuating diagnostic beam power with a half-wave plate and polarizing beam splitter system, a similar set of optics used to extract a reference beam to evaluate any laser power fluctuations during tuning, and lastly a simple plano-convex lens telescope to reduce the beam size.

This experiment involved two sub configurations of the TDLAS measurement. The first configuration utilized an adjustable height periscope to precisely locate the laser path in the flow in order to extract the density and temperature cross sections. The window for the diagnostic measurement in the jet characterization experiment is a 2.75 CF viewport, so a linear travel of approximately 30 mm is sufficient to reach the bounds of the viewport. This configuration also utilized an arm mounted on the translation stage to span over and around the chamber to mount a photodiode that

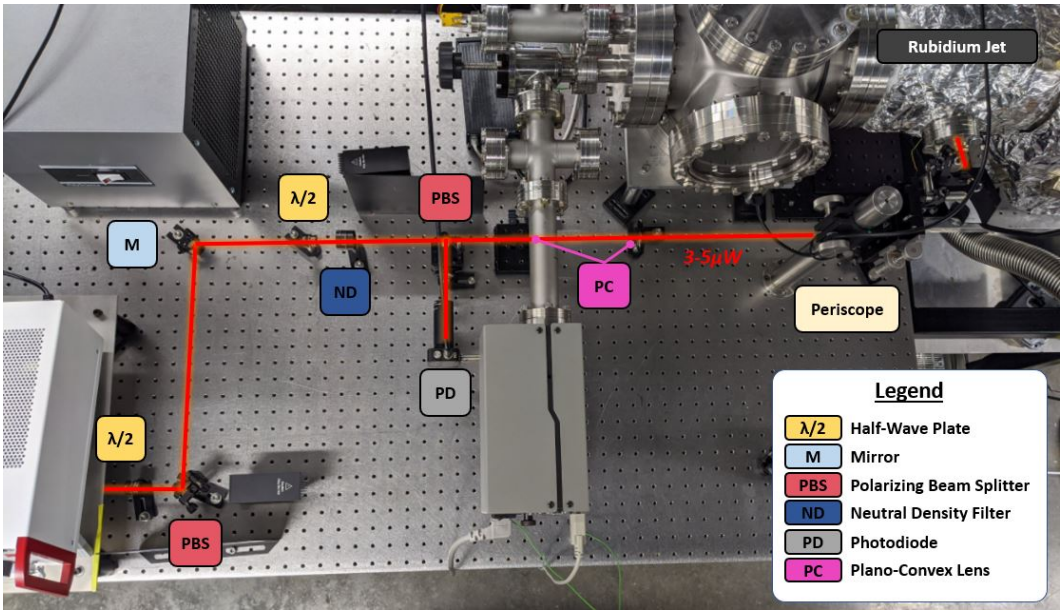

Figure 3.19: Jet characterization study TDLAS setup with reference pick-off of the diagnostic beam to account for laser power variability and an adjustable periscope to generate a density and temperature cross-section measurement.

would passively follow the laser path, shown in Figure 3.20. From Figure 3.20, it can be assumed that a long cantilever arm such as the one holding the photodiode would be highly susceptible to vibrations. Testing did reveal that table vibrations from sharp impulses or direct contact of the translation stage/arm manifested as photodiode signal fluctuations. However, it was found that if a bracing structure was placed next to the arm with a foam pad, the vibrations from adjustment of the micrometer damped out fairly quickly.

The second configuration of the TDLAS measurement in the study involved fixing the height of the periscope and precisely adjusting the angle of the beam relative to the rubidium jet axis. The goal of this configuration is to extract the axial velocity via known angle increments detecting various amounts of bulk Doppler shift in the absorption signal. The angle is swept using the kinematic mount adjustment screw, shown in Figure 3.21. Paper templates were mounted to the vacuum viewports to ensure the periscope was fixed at the vertical mid-plane and to determine the angle for test cases. The kinematic mount was first adjusted such that the beam was directed straight through the center point on both templates, then the yaw adjustment screw on the kinematic

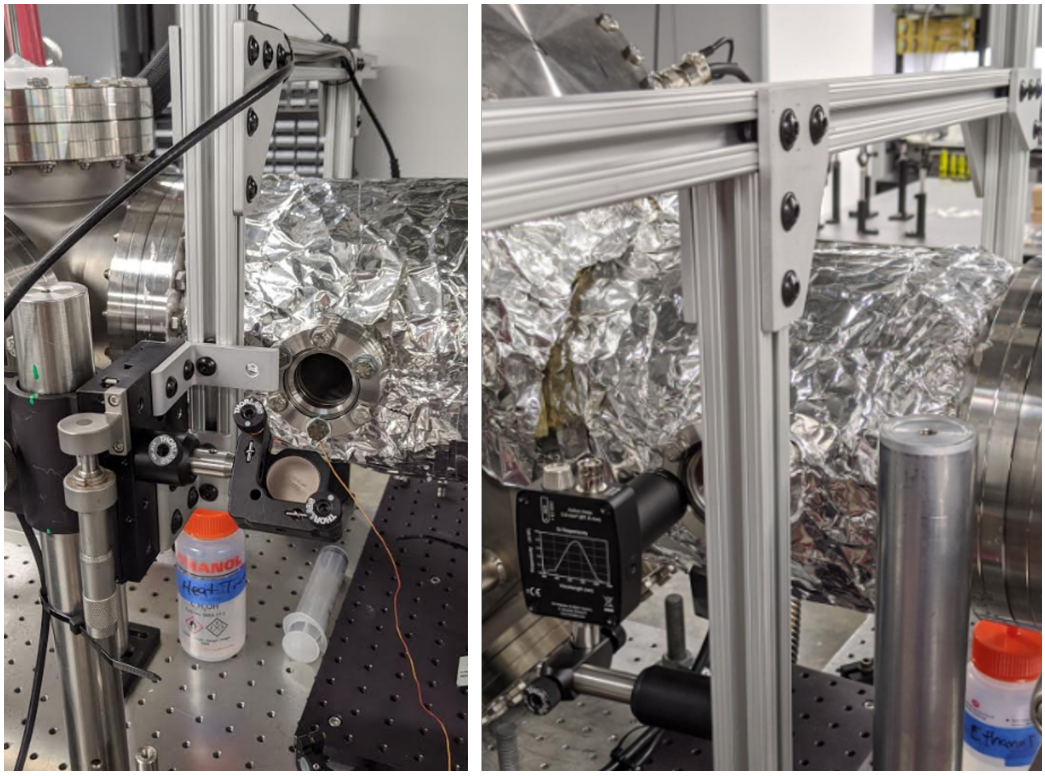

Figure 3.20: Left image shows the emission side of the TDLAS density and temperature cross-section scanner. The adjustable translation stage utilizes a micrometer to precisely adjust the height of the beam path through the chamber. Right image shows the receiving photodiode mounted to an aluminum extrusion arm which is mounted to the translation stage to passively track motion.

mount was rotated half a revolution, the resulting location on the far template was marked and later used to calculate an angle for the measurement. It should be noted here that the angles used for reference were based on the chamber axis, which cannot be entirely assumed to be aligned with the rubidium jet propagation axis. However, Section 4.1.2 describes how the data provided a factor of misalignment between the two axes.

This study also required a receiving photodiode on the far side of the vacuum chamber. However, the previous arm could not be used as it does not track with the mirror angle adjustment screw. Thus, a photodiode was mounted on an optical post fixed to the correct vertical height for the laser, then the whole optical post was re-positioned by hand to maximize the transmission signal. Once the transmission was maximized, the optical post was clamped to the table and measurement data was taken.

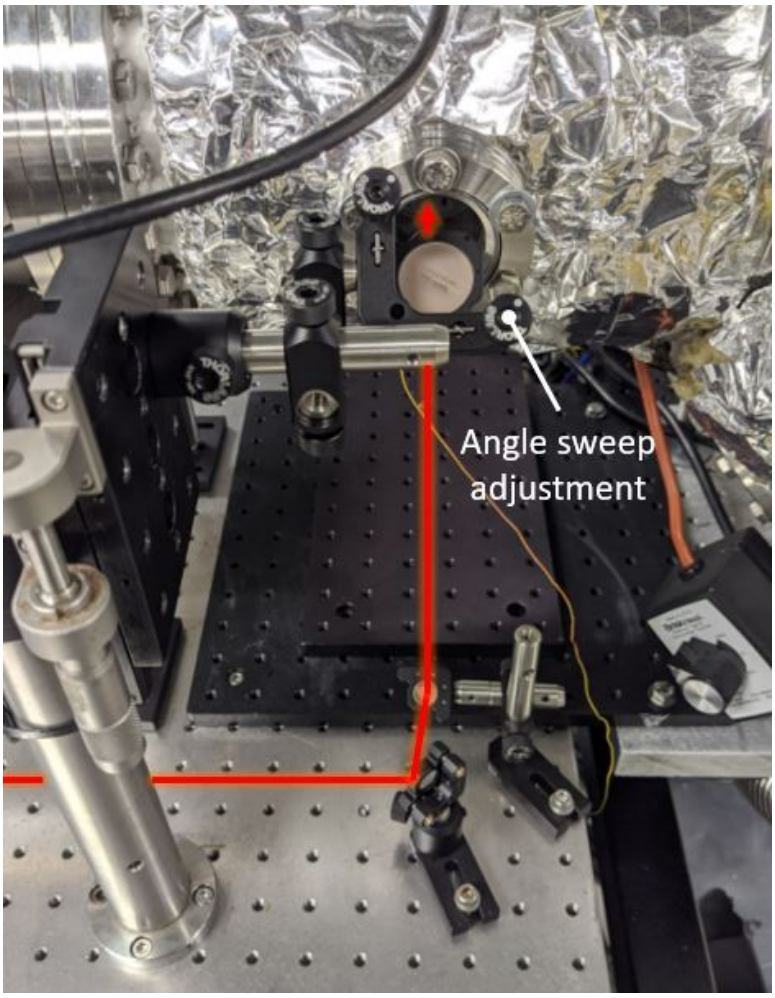

Figure 3.21: Jet characterization study TDLAS setup to analyze the bulk velocity by generating an angle sweep to vary the net Doppler shift of the absorption signal by a component of the axial velocity.

3.3.2.2 Combined Beam TDLAS

During the jet characterization study, it was determined that the time to adjust the micrometer position for the height of the TDLAS beam and save the data on the oscilloscope was too inefficient. Since the rubidium source is active for the duration of the experiment to avoid start-up transients, setup time between measurements results in wasted rubidium. With a finite amount of rubidium in the source (250 mg), it was necessary to optimize the scanning procedure. Additionally, the overlapped beam experiment included three total TDLAS stations that all needed

to be spatially synchronized. For these reasons, advancement to the diagnostic infrastructure was required. The chosen solution was to automate the spatial scanning of the TDLAS beam with a computer numerical control (CNC) gantry, shown in Figure 3.22.

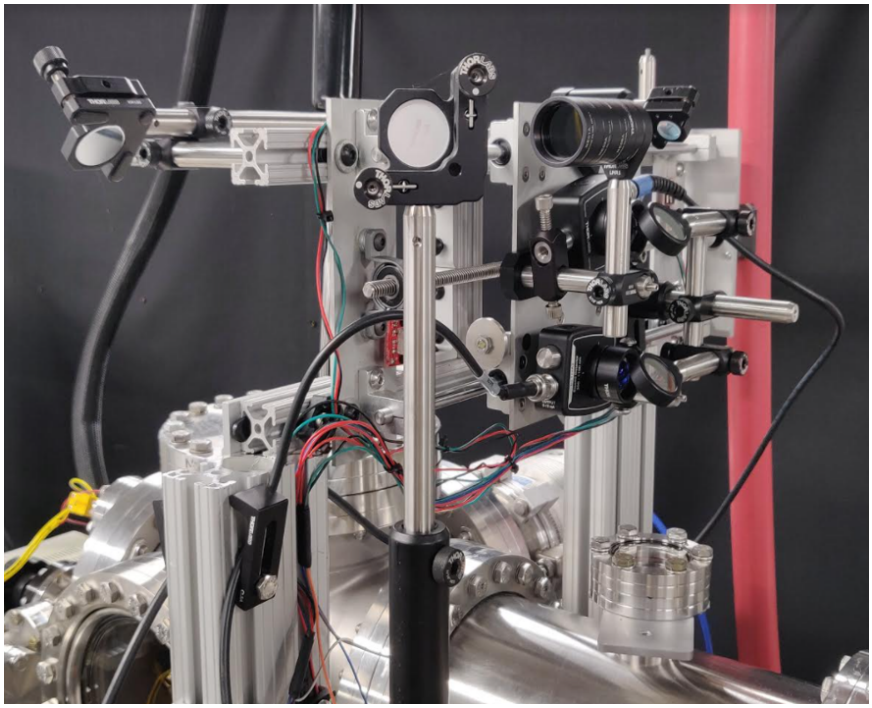

Figure 3.22: TDLAS spatial cross-section scanning gantry for the overlapped beam experiment. The scanning gantry splits an incoming diagnostic beam into three separate beams with 50/50 beam-splitters to route to three diagnostic locations in the flow. Two diagnostic stations are a retro-reflecting double-pass measurement which directs the beam back to the gantry where it passes through the beam-splitter again and into a photodiode for analysis. Station #3 is a single-pass with a photodiode mounted below the chamber on a synchronized gantry so the photodiode stays in step with the diagnostic beam.

The optical layout for the TDLAS spatial scanning gantry is shown in Figure 3.23. The frequency scanning TDLAS laser is first directed parallel to the gantry travel axis. It is critical that the beam comes in contact at the same position on the gantry optics while it spatially scans, if the beam is not aligned with this axis, it may not read on the photodiode as the beam shifts. After the beam is redirected, it is attenuated with several ND filters as to not saturate the atoms in the jet. Next, the beam is directed vertically downward to a 50/50 beam-splitter where the reflection

goes to Diagnostic Station #1 and the transmission continues to another 50/50 beam-splitter. This second reflection goes to Diagnostic Station #2. The residual transmission is directed downward to Diagnostic Station #3 and passed through the chamber to a photodiode which is mounted on a second synchronized gantry. The synchronized gantry allows the photodiode to travel in step with the diagnostic beam. All three diagnostic beams are directed toward the diagnostic station at the same point in the jet cross-section. In other words, if one of the diagnostic beams is right in the center of the viewport, the other two are as well. If one laser is 5 mm to the left of the center, the other two stations are also 5 mm to the left of center. This is critical because the position of the gantry will be used as a reference for each diagnostic, thus once the diagnostic has reached the center-line of the viewport, all three diagnostics should be centered in their respective viewports. The gantry is controlled via a custom LabView GUI which commands an Arduino Uno with a CNC Shield attached. The CNC shield allows for the easy integration of multiple stepper motors and limit switches. The CNC control LabView GUI also actively tracks the position of the gantry via the stepping increments. Once the spatial cross-section scan is started, the LabView GUI outputs a sinusoidal signal with a frequency that corresponds to the current position of the gantry (e.g. 1 mm corresponds to a signal of 10 Hz and 2 mm yields a 20 Hz signal). This waveform is designed to assist in automating the data processing; rather than recording the spatial location in the filename on the data acquisition system, the sinusoidal signal can be Fourier transformed and the position extracted automatically.

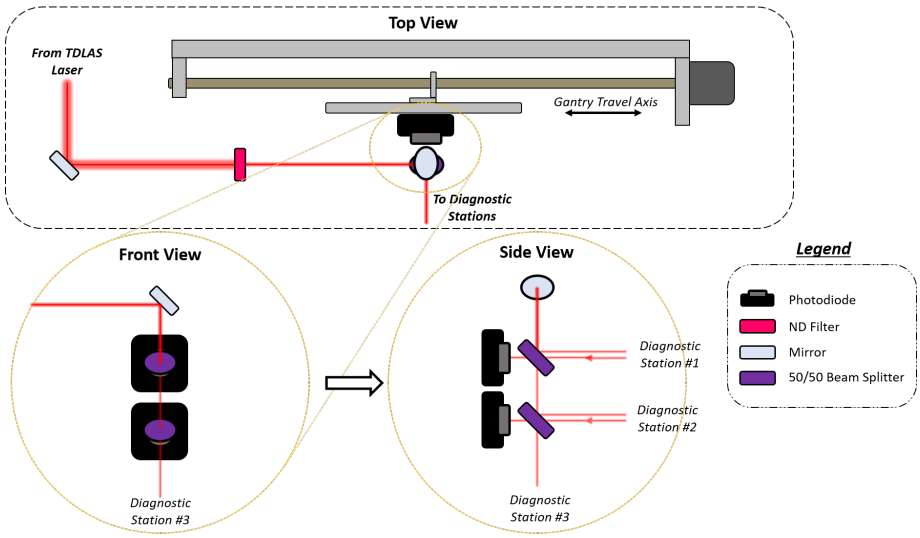

Figure 3.23: Diagram of TDLAS spatial scanning gantry optics used to separate the incoming beam into 3 separate measurements. It is important to note that there is some measurement "cross-talk" from Station 2 to Station 1 due to the use of the 50/50 beam-splitter.

Diagnostic Stations #1 and #2 are both retro-reflecting double-pass measurements that have their measurement photodiode housed on the gantry such that it maps with the back-reflected beam. Figures 3.24 and 3.25 show the vacuum-side mirrors which provide the back-reflection for Station #1 and #2, respectively. Both stations use a 75 mm x 75 mm square protected silver mirror to provide good reflectance in the near-infrared spectrum. An inherent issue with the TDLAS spatial scanning gantry optic configuration is that the back-reflection from Station 2 not only gets transmitted through to the photodiode, but also gets reflected back up to the beam splitter which separated the beam for Station #1. A portion of this reflected signal also goes to photodiode reading for Station #1. However, it should be noted that due to separations from the beam-splitters, the photodiode from Station 1 receives approximately 25% of the initial beam power as a signal and this unwanted back-reflection is 6% of the main beam power. While the unwanted back-reflection contains a non-negligible amount of power, it was found that if the optics are very slightly misaligned, the back-reflection from Station #2 measures in the noise-floor on the Station #1 photodiode. The slight misalignment of the optics results on the back-reflection from Station #2 no longer directly striking the photodiode sensor chip on Station #1.

Figure 3.24: Diagnostic Station #1 retro-reflecting mirror positioned on a 45° octagonal face. The custom mirror mount has a main cylindrical body ,which is adhered to the vacuum flange via vacuum-compatible epoxy, and an outer cylindrical housing with a 45° section milled out of the cylinder such that mirror remains horizontal when installed. The mirror is also adhered to the mount with vacuum-compatible epoxy. The two cylindrical bodies allow a rotation that can help adjust the back-reflection. Set-screws are used to lock in the rotation position.

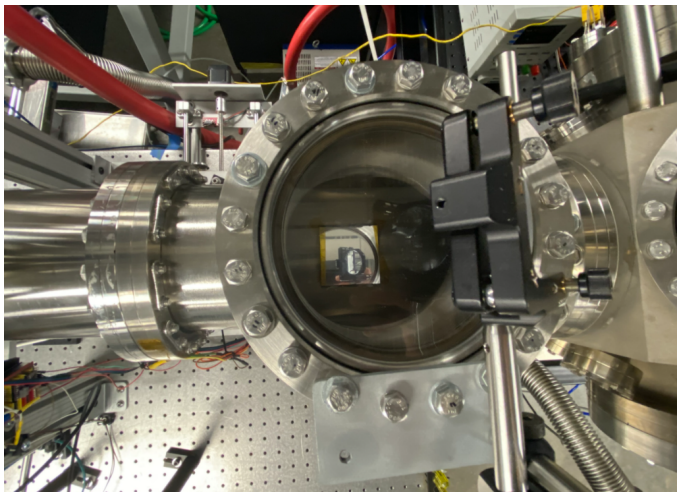

Figure 3.25: Diagnostic Station #2 retro-reflecting mirror positioned inside a vacuum Tee. The mirror is placed loosely in position with Kapton tape adhering the mirror in place while any back-reflection adjustments are made. Once the alignment is confirmed, the mirror is locked in place with vacuum-compatible epoxy.

These double-pass diagnostic measurements are used to increase the measured absorption signal and used in areas where a single-pass through the chamber is prohibited or not practical. With three TDLAS diagnostic stations along the propagation axis, the divergence of a jet can be quantified with and without the addition of the overlapping laser. Chapter 2 describes the relationship of the dipole potential as a function of the detuning from atomic resonance. From this relationship, a higher dipole force is expected as the overlapped laser is tuned closer to resonance. This presents a unique aspect for the TDLAS measurements: the depletion of the ground state atoms in the jet. If the overlapped laser is continually exciting atoms in the jet, the TDLAS diagnostic, which is tuned to measure the ground state density, will not experience absorption from these atoms. The interaction from the overlapped laser must be considered when evaluating the TDLAS transmission spectra and determining the total atomic density.

3.3.3 Overlapped Laser Analysis

Previous work by Bjorkholm et. al [31] has demonstrated the focusing effect an overlapped detuned laser has on atomic jet, however, the effect this atomic jet had on the laser was not evaluated. For the combined beam propulsion concept, quantifying and understanding the influence on each constituent beam is critical to the total system tuning parameters. Using the combined beam decoupler system outlined in Section 3.2.4, the overlapped laser is extracted at the end of the propagation section. The laser is refracted out of the chamber via the optical prism, passed through the vacuum viewport, sent to a beam sampler to attenuate, sent through ND filters to further attenuate, and passed through a lens where it is focused onto the sensor of a Thorlabs CMOS camera (Model Number: DCC1545M). An image of the laser profile is then taken at discrete time intervals during the experiment which can be traced back to overlapped laser frequency.

The expected image extracted from the experiment is an elliptical beam with a circular hole in the middle from the overlapping beam system described in Section 3.2.3. The trivial form of analysis that can be performed on these images is relative intensity as the overlapped laser tunes across the resonance. As the overlapped laser approaches the atomic resonant frequency, the overlapped laser will be absorbed more by the atoms and the final extracted profile will become

increasingly attenuated. By calculating the intensity of these collected images and plotting them against the overlapped laser frequency, the axial velocity distribution of the atoms can be extracted from their Doppler shift relative to the static resonant frequency. A second analysis that can be conducted on the images is quantification of the elliptical beam profile dimensions. By finding the major and minor axis of the ellipse, these dimensions can also be tracked with overlapped laser frequency. For an overlapped laser detuned to the red, the laser light is expected to be guided inside a dense vapor media, however, for blue detuning, the refractive index is less than the surrounding vacuum and we expect the laser light be diverted from the atomic vapor. If the images show a change in the elliptical profile dimension, this could indicate refractive effects from the rubidium jet are influencing the laser divergence.

3.4 Data Analysis and Model Fitting

The critical information of the rubidium vapor jet, that is the density, temperature, and axial velocity, are measured by their influence to the rubidium absorption spectrum. To extract these parameters from the absorption spectrum, the follow data analysis routine is used (Note: signals are all analyzed in MATLAB):

1. Triangle voltage waveform is supplied to tunable diode diagnostic laser to frequency scan. This signal is recorded in the data acquisition system.

   Note: The scanning range of the tunable diode laser should be large enough to include sufficient data outside the absorption frequencies (i.e. where transmission is equal unity).

2. The output of the tunable diode diagnostic laser is split into a main TDLAS diagnostic beam and power reference beam. The low power reference beam is directed to a photodiode and is recorded. This information will be used to normalize the transmission spectrum based on power fluctuations in the laser while it frequency scans.

3. The TDLAS absorption profile is read from a photodiode as the laser frequency scans and

recorded. This provides a diagnostic transmission signal with a y-axis of volts and an x-axis of some arbitrary time scale.

4. Simultaneously the SAS profile is recorded. As the laser scans, natural-broadened hyperfine peaks are visible in the spectrum. This SAS transmission signal also has y-units of volts and x-units of an arbitrary time scale.

5. The hyperfine and cross-over resonance peaks are located using the findpeaks command in Matlab. The ratio of the spacings between these peaks is calculated and compared to the ratio of spacings between the hyperfine and cross-over resonances provided by Steck [54, 55]. This process matches the SAS peak with the correct hyperfine or cross-over resonance line.

6. A frequency axis is generated that places each SAS peak on their correct frequency location. This frequency axis can then be used for any diagnostic data taken at the same instance. It is important to note that due to frequency drift in the tunable diode laser, the frequency axis needs to be computed for each unique dataset.

   Note: Applying the newly generated frequency axis from the SAS to the TDLAS signal, the data is now of photodiode voltage vs. frequency.

7. To convert the photodiode voltage signal to a transmission through the chamber, it simply needs to be normalized. While normalization may appear trivial, experimental testing revealed several challenges:

   (a) The reference beam split-off from the TDLAS needs to be normalized by dividing the whole signal by its maximum, thus yielding values at or below unity.

   Note: It is beneficial at this stage to fit a curve to this reference data such that noise levels do not compound in the next stage.

   (b) Once this fit to the power variation inherit to the laser scanning is created, it can be divided from the TDLAS diagnostic measurement.

(c) During experimental testing it was found that the vacuum viewport had its own transmission function that was dependant on both space and laser frequency. Thus a sufficient background profile is needed that goes through a spatial and frequency scan without a rubidium jet. This background profile can then be subtracted from TDLAS signal during the experiment. By using a background subtraction method, the reference photodiode can be ignored as power fluctuations are captured in the background.

8. After normalizing the voltage signal to become a transmission signal, it is now transmission vs. frequency data and a rubidium absorption model can be used to fit to the data. Using a modified rubidium absorption model code developed by Rekhy et al. [61], the density, temperature, and frequency Doppler shift are input as parameters and the convolution of the natural and thermal Doppler broadening produces a model to compare with the data.

9. Using the lsqcurvefit function in Matlab, this process can be automated to perform a least squares regression and determine the most likely density, temperature, and Doppler shift to the data.

   Note: It should be noted that the absorption also depends on the path length through the medium, for this reason, the density is actually the path integrated number density and the path length is set equal to unity.

   Note: Errors in the normalization process may produce transmission spectrum data with non-physical artifacts (e.g. some areas where the transmission is above unity but the area of interest around the absorption feature is still fit correctly). The region of the model fitting might need to be adjusted to solely focus on the absorption feature in order to prioritize finding a minima of the residuals for the absorption feature.

10. This analysis can then be done for the TDLAS signal at discrete locations in the jet cross section and/or discrete frequency values of the overlapped laser (if applicable).

11. This will yield a path integrated density cross section which can then be integrated again

across the translation stage dimension to effectively produce $N \cdot A$ for the mass flow rate calculation.

12. The Doppler shift from the model fitting can be transformed to a velocity component that is aligned with the propagation vector of the laser. From taking the Doppler shift measurement at several discrete angles relative to the propagation axis, a linear fit relation can be applied to the $\sin\theta$ vs. effective Doppler shifting velocity where the slope is the actual bulk velocity of the jet and the y-intercept is the degree of misalignment off of the anticipated central propagation axis.

13. Lastly, this axial velocity and integrated density can back out a mass flow rate from the atomic source.

4. RESULTS

As mentioned throughout Chapter 3, the work discussed in this thesis spans the breadth of two primary experiments: a rubidium jet characterization study and an initial overlapped beam experiment. The goal of the rubidium jet characterization study was to evaluate the effectiveness of the jet source, laser diagnostic technique, and chamber infrastructure. From the results of this study, changes were applied to the component design where necessary, to prepare for the introduction of the overlapped laser. The overlapped laser experiment introduced several new and modified hardware components (Section 3.2). The goal of the latter overlapped beam experiment was to identify if the overlapped laser could focus the jet of atoms, and if the refractive index of the jet could alter the laser profile in a quantifiable way. The overlapped beam experiment also expanded on the number of laser diagnostic stations which caused the need to evaluate the new infrastructure for these stations during testing (Section 3.3.2). This chapter is divided into two primary areas to provide the results for both of the two fundamental tests.

4.1 Jet Characterization Study

The jet characterization study utilized the body-clamped rubidium jet source, shown in Section 3.2.1 Figure 3.6, a single TDLAS measurement station halfway along the propagation length, and the original flat plate beam dump. To effectively characterize the rubidium jet in this study, two separate measurements needed to be conducted: an orthogonal TDLAS cross-section scan to extract density and temperature and an angle sweeping scan to quantify the axial velocity. With the density cross-section and axial velocity, a mass flow rate can be determined. These studies could have been conducted with an angled cross-section scan, however, due to the size of the viewport, the vertical scanning height became severely limited with the introduction of any non-orthogonal angle.

4.1.1 Density and Temperature Cross-Sections

Density and temperature cross-section scans were conducted through two tests over two days. The first testing period utilized a slightly angled cross-section scan while the second test attempted to be completely orthogonal to the viewport. Between the first and second day of testing, the rubidium getter was deactivated and the vacuum chamber systems (cooling equipment and vacuum pumps) remained active. During the cross-section scan studies, the micrometer on the adjustable height periscope was incremented in half-millimeter denominations. With a Ø1 mm diagnostic beam at approximately 4.5 μW, this laser beam is scanned across the vertical cross-section of the rubidium jet and an example portion of the measured transmission spectrum is shown in Figure 4.1.

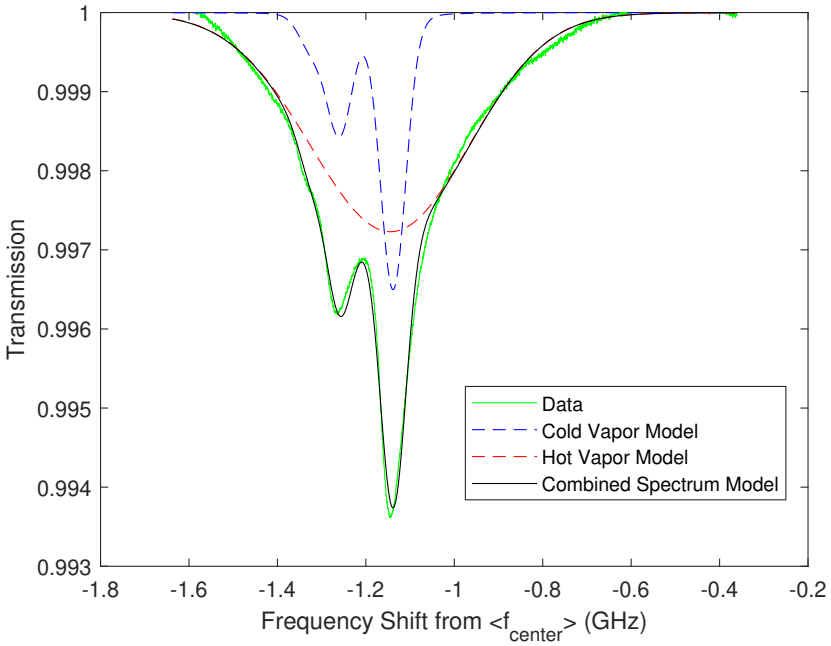

Figure 4.1: Measured transmission data through TDLAS diagnostic, compared to fitted rubidium transmission model for a cold vapor, hot vapor, and their combination. The data shown is sampled from a vertical height 14 mm down from the top of the vacuum viewport for a getter current at 12.13 A, which is near the maximum recommended current.

From Figure 4.1, the wings of the measured transmission spectrum appear to be dominated by a greater thermally broadened vapor, whereas the center of the feature is less thermally broadened. The center of the feature is cold enough where the hyperfine absorption features are prevalent. Thus the measured spectrum is hypothesized to stem from a combination of absorption from a hot and cold vapor. This "bi-modal" distribution behavior has been predicted by Sanna and Tomassetti [52] and is discussed in Section 2.3. At lower getter current settings the bi-modal distribution was less prevalent, and instead the absorption spectrum was predominately indicative of only a cold vapor present. This behavior indicates that the decrease in mass flow rate from the getter likely pushes the flow regime to free-molecular flow very close to the mouth of the getter such that the divergence between the two groups is minuscule.

Due to the combination of absorptions from these two atom groups in datasets for higher getter currents, the analytic methods needed to be modified to include the input parameters of two separate densities, temperatures, and bulk Doppler shifting velocities. This combined transmission model is then fit to the data as discussed in Section 3.4. The jet parameters are then fit for all vertical height increments to get a density, temperature, and bulk Doppler shifting velocity for the discrete vertical locations in the beam.

In the data processing method, the measured absorption spectrum is first normalized through background subtraction for the corresponding frequency range and window position. However, even with a background subtraction, there exists residual transmission variation (not generated by rubidium) with frequency and spatial dependence in the viewport that heavily influenced the transmission spectra near the top and bottom of the viewport. Therefore, the spectra near micrometer positions before 1 mm and after 24 mm present non-physical alterations to the spectrum that should be neglected for analysis. A potential source of error in the background subtraction technique is the method relies on the assumption that the laser did not experience any frequency drift and the laser position is exactly constant between the measurement and background (or transmission perturbations across the spatial gradient is minimal). Since the transmission variations after background subtraction have an influence on the shape of the absorption features, a method was

required for determining how to exclude datasets that were heavily perturbed. To identify spectra that are effected by these non-rubidium perturbations, the sum of the squared residuals between the final model fit and the data for that location is calculated. For reference, Figure 4.2 shows the sum of the squared residuals for each fit across the vertical height scan. The accuracy of the fit sees a sharp decrease in the initial two locations and approximately the last 6 mm of the scan range. These results will be excluded from curve fitting for the density and temperature profiles as these fitting inaccuracies are likely attributed to inconsistencies in the background subtraction.

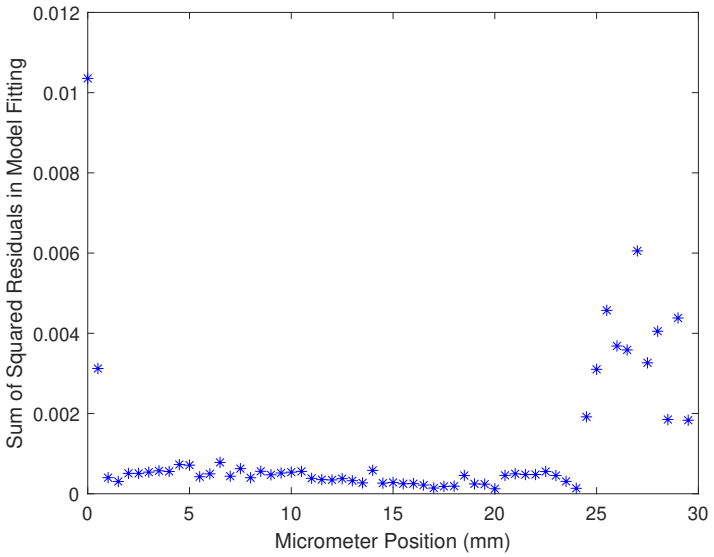

Figure 4.2: Sum of the squared residuals in the model fit to the data near the ^{85}Rb F = 3 ground state transition. The case shown is for a rubidium getter current set to 12.13 A. The residuals are higher near the start and near the end of the vertical height scan due to inconsistencies in the background subtraction that manifested in non-physical transmission in the spectra.

Once the ideal spectra have been chosen for further analysis, the density data for the hot and cold vapor are fit with parabolic curves. An example of the parabolic fit for the cold vapor density is shown in Figure 4.3. Since the vacuum viewport provided insufficient optical access to cover the entire cross-section of the atom jet, an axisymmetric assumption is utilized to quantify the cross-section parameters of the jet.

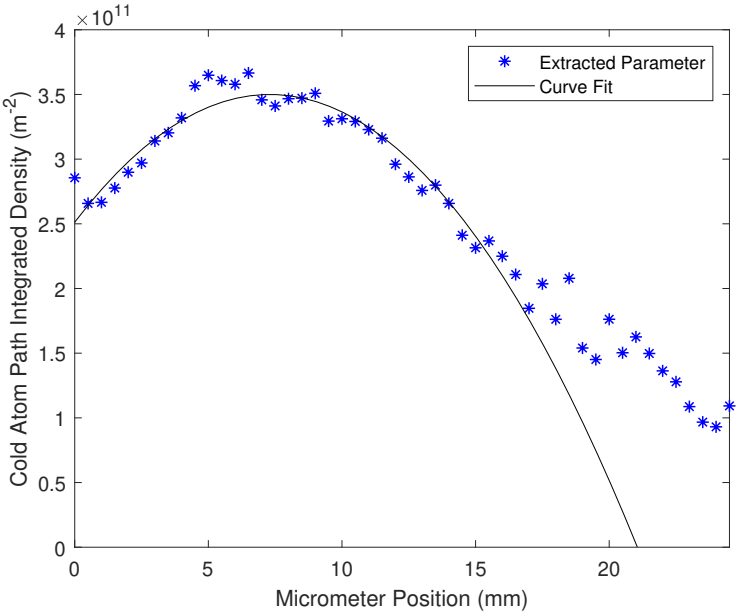

Figure 4.3: Path integrated atomic number density as a function of micrometer position height in the flow and the parabolic curve fit. The curve fit neglects data which has model fitting residuals which were considered significant. Data shown is for getter current of 11.66 A.

The fitted density parabola can then be integrated along the vertical axis between the roots of the function to extract the area integrated number density, N_A. This area integrated number density is provided for several getter currents in Table 4.1. From the data in Table 4.1, a sharp fall-off in measured density between the two tests is apparent. This behavior is attributed to depletion of the 50 mg of rubidium alloy in the getter reservoir from the first day of testing to the second.

Current (A)	Test #1 N_A Cold	Test #1 N_A Hot	Test #2 N_A Cold	Test #2 N_A Hot	Test #1 N_A Total	Test #2 N_A Total
10.26	0.42	0.90	0.13	0.06	1.32	0.19
11.10	0.80	0.74	0.48	0.44	1.54	0.93
11.66	0.81	0.88	0.64	0.42	1.70	1.06
12.13	1.36	1.46	0.91	1.90	2.82	2.82

Table 4.1: Extracted area integrated number density, N_A, for the cold vapor, hot vapor, and their cumulative sum over two tests for various getter currents. All area integrated number densities are in units of $\times 10^{10} m^{-1}$. Note: lower getter current values for hot vapor density are highly susceptible to errors as the hot vapor absorption spectrum approaches the noise floor.

The temperature cross-sections were more trivial to process. As the model was fitted to the data, the temperature of the hot and cold vapors were determined. The relationship between temperature and beam position in the flow appeared to be fairly constant when neglecting data with high model fitting errors. The average temperature for the same four getter currents is provided in Table 4.2.

Current (A)	Cold Atom Average Temperature (K)	Hot Atom Average Temperature (K)	$T_{\perp Hot}/T_{\perp Cold}$
10.26	4.85	57.1	13.4
11.10	4.45	85.6	19.2
11.66	5.78	150	26.0
12.13	5.72	202	35.3

Table 4.2: Average atom temperature results for model fitted parameters from the jet characterization study for four unique getter electrical currents. Data provided is from density and cross-section Test #2.

The temperature information from these cross-sections serve to determine the required dipole potential trap depth to confine the atoms. However, from Section 2.3, the ballistic trajectories the atoms travel on after they are emitted results in the central atoms being at a fairly low divergent temperature. For clarification, the temperature here primarily serves as a quantification of the maximum divergence. At this point it is important to recognize the rubidium absorption model developed by Rekhy et al. [61] used for this work, assumes a Gaussian profile for the thermal Doppler broadening. This assumption relies on the presence of a Maxwellian velocity distribution function (Section 2.4). Since the atoms are not experiencing collisions and travelling on their ballistic trajectories, the Maxwellian VDF cannot be assumed. Future work would need to generate a method of velocity broadening the spectrum based on the velocity distribution function actually exhibited in the jet, such as the one presented by Cai and Boyd [62]. It is also important to note that the coupled relationship with density and temperature in the absorption spectrum will contribute to inaccuracies in the density measurement as well.

4.1.2 Axial Velocity

The axial velocity study for the jet characterization utilized the setup described in Section 3.3.2.1. The setup for this study involved determining the angle of the diagnostic beam relative to the central axis of the vacuum-chamber. Once the angle change for each rotation of the kinematic mount adjustment screw was determined, the absorption spectrum is measured at each angle. These absorption spectra are then fit using the process outlined in Section 3.4 with particular focus on the bulk Doppler shifting velocity.

Section 4.1.1 discussed a decline in the measured density due to rubidium reservoir depletion. This effect was more prominent on the third day of testing for this axial velocity study. To generate enough flow to detect the absorption signature, the getter current was required to increase beyond the values tested for the density and temperature cross-sections. This getter current mismatch requires extrapolation in the axial velocity data to determine a mass flow rate. The depletion of the rubidium reservoir continued to influence the axial velocity testing as the absorption features gradually diminished and full angle sweeps needed to be reduced in order to obtain more getter current sample points.

The bulk Doppler shifting velocity as a function of measurement angle and getter current is presented in Table 4.3 and an example of how the axial velocity is determined is plotted in Figure 4.4. It should be noted that during the $I = 14.07A$ test case, the rubidium remaining in the reservoir was fully depleted and the spectra measured during this test case were near the noise floor and are highly susceptible to errors.

Figure 4.4 shows a linear relationship between the sine of the measurement angle and the Doppler shifting bulk velocity detected in the absorption spectrum. The slope of this linear relationship is considered to be the actual jet axial velocity. Additionally, the x-intercept of the plot can be considered to be the degree of misalignment with the jet propagation axis and the vacuum chamber central axis. This axial velocity and jet misalignment angle is provided in Table 4.4. Section 4.1.3 will discuss how the axial velocity determined for these elevated getter currents is extrapolated for the lower getter currents tested during the density studies.

Current (A)	Measurement Angle (°)										
	-3.3	-2.7	-2.1	-1.4	-0.7	0	0.7	1.4	2.1	2.8	3.1
12.13	-60	-50	-49	-45	-38	-27	-20	-13	-8.1	-6.2	0.0
13.01	-61	-56	-44	-39	-36	-28	-20	-12	-6.7	-	-
13.50	-66	-53	-49	-41	-33	-29	-	-	-	-	-
14.07*	-54	-63	-46	-47	-32	-28	-	-	-	-	-

Table 4.3: Doppler shifting velocity (m/s) for each absorption spectrum at varying angles relative to the vacuum chamber central axis and getter current supplied to the rubidium source. Note: missing data entries are due to rubidium reservoir depletion resulting in incomplete angle sweeps.

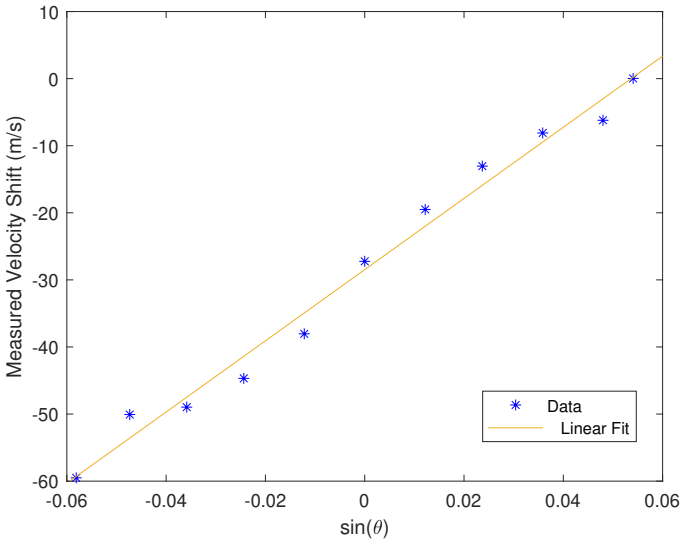

Figure 4.4: Measured velocity shift of the absorption spectrum for varying diagnostic beam measurement angles relative to the vacuum chamber central axis. The resulting linear fit has the a slope of 531 m/s and a y-intercept of -28.5 m/s.

Current (A)	Axial Velocity (m/s)	Jet Axis Misalignment (°)
12.13	531	3.07
13.01	579	2.65
13.50	619	2.48
14.07*	549	2.99

Table 4.4: Axial flow velocity jet axis misalignment determination for various high current settings based on linear fit relationship between measured velocity and measurement angle.

4.1.3 Mass Flow Rate Determination

As discussed in Section 4.1.1, the rubidium reservoir quickly depleted during testing. To measure an absorption feature in the diagnostic, the getter source current needed to be increased. Consequently, this requires the extrapolation of the axial velocities from trends discovered at higher getter currents. Utilizing a linear fit between getter current and axial velocity, the extrapolated axial velocities for the getter currents tested during the density and temperature cross-section studies are presented in Table 4.5. While the physical relationship between getter current and atom velocity is non-linear, the complexity of the dependence and the number of sample points required the approximation through a linear fit. The velocity of the atoms is assumed to be the most probable thermal velocity, thus making the relationship between getter current and getter temperature. The temperature of the getter relies on the heat balance between the input of the resistive heating and the output of radiation, conduction, and convection (escaping rubidium), all of which having various relationships with temperature. Due to the radiation consideration, the problem becomes a fourth order function between current and thermal velocity. Additionally, considering convection from emitted rubidium would require knowledge of the mass flow rate in advance. Furthermore, with only four data points of velocity as a function of current, a high order fitting function would be badly conditioned. For these reasons, the data is extrapolated with a linear fit, however, it is recognized as a source for error. On the final getter current test of $I = 14.07A$, the measured absorption spectrum was nearing the noise floor, and it is assumed at this point the reservoir was fully depleted. Due to the inconsistency with this test case, this data point has been excluded from the fitting relationship. The linear fit between axial velocity, $v_{\parallel}$, and getter current, I, was found to be:

$$v_{\parallel} = 63I - 236 \tag{4.1}$$

Using the estimated area integrated number density (Section 4.1.1) and the extrapolated axial velocity (Section 4.1.2), the mass flow rate, $\dot{m}$, is calculated as follows:

$$\dot{m} = m v_{\parallel} \iint_{A} N = m v_{\parallel} N_A \tag{4.2}$$

Modeling efforts discussed in Section 2.3 and published in Morgan et al. [51] estimated that for this effusive jet source geometry, 0.16% of the flow emitted from the getter passes through the flow-limiting shroud. With this flow ratio approximation, the full mass flow rate from the getter can be estimated from the mass flow rate that entered the experiment. The determined mass flow rate from the getter source, $\dot{m}_{getter}$, is provided in Table 4.5. To extract the mass flow rate of the emitted jet, the getter mass flow rate is multiplied by the flow pass ratio.

Current (A)	Test 1 N_A ($\times 10^{10} m^{-1}$)	Test 2 N_A ($\times 10^{10} m^{-1}$)	Axial Velocity (m/s)	Test 1 $\dot{m}_{getter}$ (μg/s)	Test 2 $\dot{m}_{getter}$ (μg/s)
10.26	1.32	0.19	411	0.48	0.07
11.10	1.54	0.93	464	0.63	0.38
11.66	1.70	1.06	499	0.75	0.47
12.13	2.82	2.82	529	1.32	1.32

Table 4.5: Mass flow rate determination for four getter current values. N_A is area integrated number density and $\dot{m}_{getter}$ is mass flow rate from the getter rubidium emission source. Data for testing over the span of two days is provided.

The results of the measured getter mass flow rate as a function of getter current are compared with several data points provided by the manufacturer for the getter used in Figure 4.5.

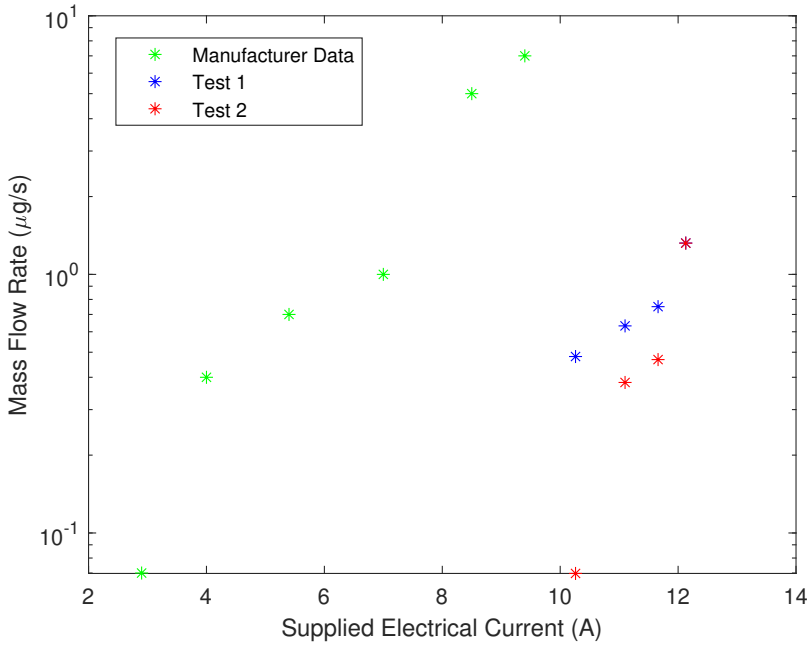

Figure 4.5: Mass flow rate from rubidium getter source for electrical current supplied calculated for each day of testing and compared against manufacturer data.

4.1.4 Jet Characterization Performance Discussion

An estimated V Parameter for the effusive source can be calculated by first using the area integrated number densities provided in Section 4.1.1, and dividing them by the area of the jet at the diagnostic location, which yields the average number density. The jet area is approximated through the average of the range between the roots of the polynomial fit for the four getter current settings. This resulted in an estimated jet diameter of 30 mm at the diagnostic station. This average number density is then used in the equations provided in Section 2.2 to calculate the V Parameter. This plot is shown in Figure 4.6. From the estimated V Parameter, this effusive jet source meets the minimum requirement for guiding of $V = 2$ (determined by Castillo et al. [29]) for overlapped laser red detunings less than 30 GHz for $I = 10.26$ and 60 GHz for $I = 12.13$. At these frequencies, the scattering rate is approximated to be 3 Hz. These calculations indicate that the rubidium jet source is capable of showing some amount of refractive guiding in a regime that does not result in significant atom heating through scattering.

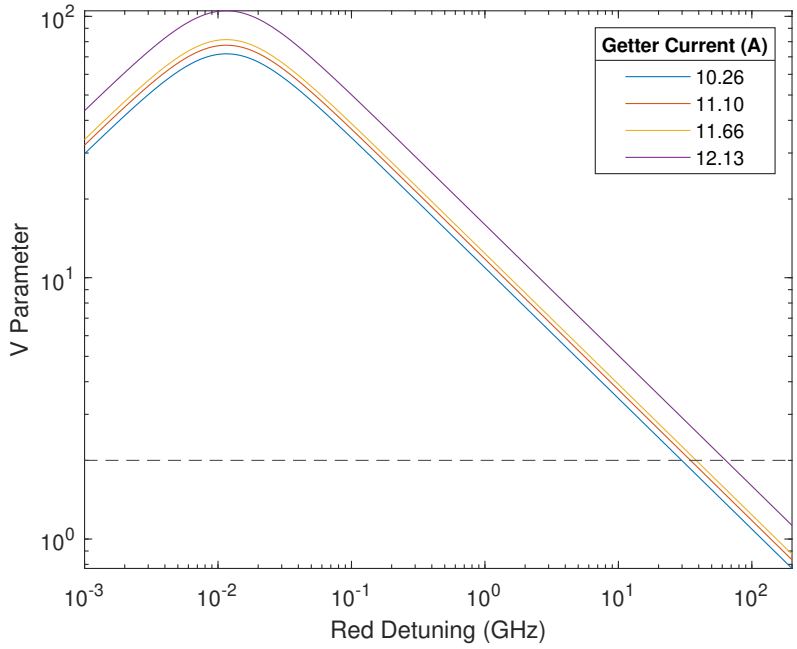

Figure 4.6: V Parameter as a function of laser detuning from calculated number density at various getter current settings. The plot assumes an overlapped beam diameter of 30 mm and laser power of 1 Watt. The horizontal dashed black line corresponds to V = 2. V Parameter reduction near resonance is caused by saturation effects.

From the mass flow rate metric calculated in Section 4.1.3, Figure 4.5 indicated that the effusive source under-performed when compared to the manufacturer's supplied values for mass flow rate. This is hypothesized to stem from the clamping method of the getter in the source design. The manufacturer's suggested mounting method utilizes the thin metal tabs on both ends of the getter to clamp it in position, through this thin material the heat from the reservoir does not experience much conduction and it can maintain more heat. However, the effusive source design for this experiment (Section 3.2.1) utilized a ceramic V-block to clamp the cylindrical reservoir body of the getter. Ceramic was chosen to minimize the conductivity from the reservoir while still rigidly constraining the axis of the getter relative to other experiment hardware. Since more current was needed to generate an equivalent mass flow rate to what the manufacturer specified, the energy balance in the getter can be assumed to have encountered more heat losses than it was tested for (e.g. conduction to the ceramic block). To optimize performance and obtain a more dense atom jet,

a new jet source was created that constrains the getter by clamping the designed tabs. The results of this new source design are discussed in Section 4.2.

Section 4.1.1 gave insight into a source of inaccuracy in the density and temperature measurements due to the parameter extraction technique used in the processing. The rubidium absorption model code requires the assumption of a Maxwellian velocity distribution function to develop the Gaussian thermal broadening in the absorption spectrum. In the case of a free-molecular flow expanding into vacuum, this VDF cannot be assumed and instead must use a VDF that is based on the source geometry which is discussed in more detail by Cai and Boyd [62]. This will be presented as an area for future work in Section 5.2.

A final area for improvement stems from the total time the rubidium getter was active during testing. Section 4.1.2 described the effect on getter reservoir depletion requiring higher supplied currents to generate flow. The density and temperature scanning procedure is very time intensive as it involves precisely adjusting the beam height micrometer, allowing the signal to stabilize, renaming the file prefix on the oscilloscope to indicate the position at which the data was taken, and stopping and saving out the waveforms. This process is repeated from 0 mm up to 29.5 mm in half millimeter increments. The time required to generate the 60 datasets is rather significant as the getter is left active the entire time. An initial consideration is to operate the getter in a "pulsed" regime so it is only active when data is ready to be taken. This pulsing was not used in order to avoid measuring thermal start-up transients in the absorption spectra. The time spent taking data spurred the development of the TDLAS scanning gantry discussed in Section 3.3.2.2. This scanning gantry automates the diagnostic beam positioning in an accurate and repeatable way. Additionally, this gantry utilized a GUI that monitored the total displacement and output a sine wave function with a frequency proportional to the displacement from the start of the scan. This sine wave output was used to circumvent the need to record the scanning position with each dataset saved. Instead, the sinusoidal signal can be measured and the position extracted in data processing via a Fourier transform.

While this jet characterization provided several areas for improvement, it also yielded multiple

successful findings. The experiment proved that a rubidium jet could be generated in the vacuum chamber facilities, be characterized by a TDLAS diagnostic technique, and condense at the end of the propagation on the beam dump and in the rejected region of the plume with the condensation shroud. These successes point to a capable vacuum infrastructure, a passively cooled beam dump plate having enough heat removal to condense the rubidium, and the actively pumped shroud preventing the rejected rubidium from filling the vacuum chamber and contaminating the diagnostic. All three of these areas were subject to concern prior to the experiment, and resolving them gave better confidence for the overlapped beam study. Additionally, the characterization of the flow in this experiment can be used in modeling and simulation efforts to determine if the rarefied flow could provide any refractive guiding effects to an overlapped laser or if a dipole trap would show a significant density distribution change.

4.2 Overlapped Beam Experiment

The overlapped beam experiment utilized a revision of the effusive jet source that had a fixturing method which was more ideal for heat retainment in the rubidium reservoir. Additionally, two more TDLAS diagnostic stations were added (for a total of three) to better characterize the rubidium jet as it propagates and study the evolution of the beam. This experiment was first test case for the laser spatial scanning gantry which took a single diagnostic beam and split it into three beams for each diagnostic station. These beams were all spatially synchronized as discussed in Section 3.3.2.2. Lastly, this experiment was the first use of the overlapped beam decoupler which reflected the rubidium atoms and refracted the laser out of the chamber via a heated optical prism.

4.2.1 Data Acquisition

With all of the advancements to the testing infrastructure, data acquisition became non-trivial and could not be conducted entirely on one 4-channel oscilloscope as with the jet characterization study. The data sources that needed to be captured during the experiment are:

1. Diagnostic laser tuning voltage waveform
2. Overlapped laser tuning voltage waveform

3. Saturated absorption spectroscopy photodiode
4. TDLAS Station 1 photodiode
5. TDLAS Station 2 photodiode
6. TDLAS Station 3 photodiode
7. Scanning gantry position waveform
8. Extracted overlapped laser image
9. Beam dump temperature
10. Heated beam separation prism temperature
11. Condensation shroud temperature
12. Getter current
13. Vacuum chamber pressure
14. Residual gas analyzer (monitoring for rubidium)
15. Diagnostic laser wavelength
16. Overlapped laser wavelength

Items 1-7 require the use voltage trace monitoring through an oscilloscope or equivalent data acquisition unit. Since seven voltage traces needed to be logged, a NI BNC-2110 data acquisition system was used in conjunction with a data acquisition LabView GUI to monitor the voltage traces and intermittently save the camera image of the extracted overlapped laser profile. The scanning rate of the diagnostic laser system is optimal when run at higher rates (e.g. 100 Hz) to shorten the time for data averaging and to reduce the influence from low frequency external noise sources. This high diagnostic scan rate required the sampling rate of the data acquisition to also be increased as sample resolution is critical for discerning the hyperfine and crossover features in the saturated absorption spectrum and accuracy in the TDLAS measurement. However, initial data analysis revealed cross-talk between adjacent channels on the data acquisition system that sufficiently contaminated the signals. For this reason, the voltage traces were split amongst a 4-channel oscilloscope (traces 2,4-6) and the NI BNC-2110 data acquisition system (traces 1-3,7) with adjacent ports left empty. The goal was to cross-reference the signals based on the overlapped laser

tuning voltage (trace 2) and the time since the start of the experiment. However, having to cross-reference two data acquisitions yielded a computationally burdensome data analysis process since the NI DAQ system saved out a continuous stream of data and the oscilloscope saved out single waveforms. Additionally, with the TDLAS diagnostic stations on one measurement device and the SAS signal on the other, the matching of these two systems is subject to error. The data acquisition system used for an experiment of this scale is a consideration that will need to be evaluated in future work.

4.2.2 TDLAS Results

A unique change for the laser diagnostic system in the overlapped beam experiment is the ability to measure the absorption spectra of the atom jet as a function of the overlapped laser detuning. By generating the transmission surface as a function of overlapped laser detuning and diagnostic laser detuning, which is shown in Figures 4.7 - 4.9, two key insights can be drawn: the axial velocity spread and the depletion of the ground state atoms as the overlapped laser tunes close to resonance. Through tuning the overlapped laser across the atomic resonance, and comparing the TDLAS spectra at one frequency, the axial velocity can be extracted. If the overlapped laser is sufficiently detuned to cover the entire width of the shifted transition, the absorption spectrum would indicate a uniform bulk velocity and also the variation in the bulk velocity, as some atoms in the jet might have a greater axial velocity while others have less. As discussed in Section 4.1.4, the typical Gaussian thermal broadening mechanism that assumes a Maxwellian VDF would not be appropriate for modeling this system and future work would be needed to determine an appropriate method for considering this spread in the absorption spectrum. The other key insight from Figures 4.7 - 4.9 is the depletion of the ground state from the overlapped laser intensity resulting in a lower density measurement from the TDLAS diagnostic. This is information is valuable because as the laser intensity regions change, the expected ground state density detected by the diagnostic will indicate this through more or less absorption. By tuning the overlapped laser far from resonance and minimizing that absorption, the total density of the jet can be calculated, however by tuning closer to the atomic resonance with the overlapped laser, this will provide insight to the intensity

of the overlapped laser profile. A more direct measurement of the overlapped laser intensity profile would utilize a second diagnostic beam tuned at an excited state transition to directly quantify both the ground and excited state densities at each discrete point in the flow. From comparison of these two densities, the laser intensity driving the population distribution can be quantified.

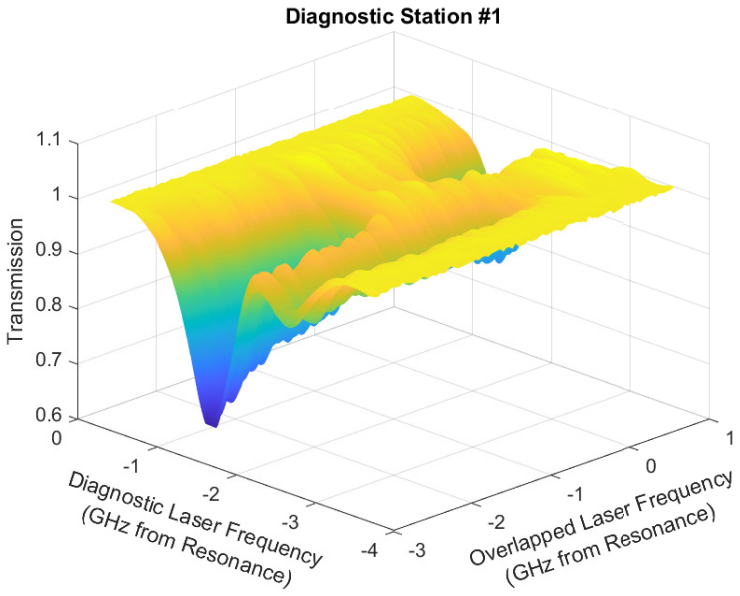

Figure 4.7: Diagnostic Station #1 (nearest to rubidium jet source - double pass measurement) transmission profile as a function of overlapped laser frequency and diagnostic laser frequency.

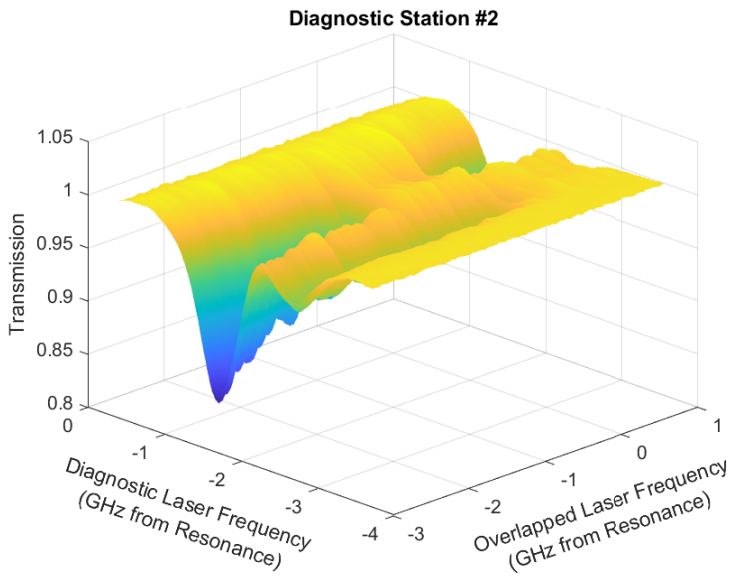

Figure 4.8: Diagnostic Station #2 (mid-propagation distance - double pass measurement) transmission profile as a function of overlapped laser frequency and diagnostic laser frequency.

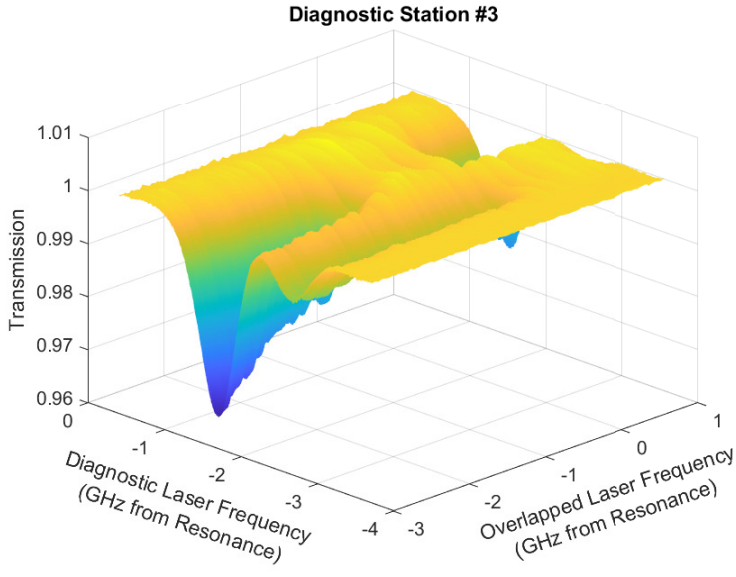

Figure 4.9: Diagnostic Station #3 (furthest from rubidium jet source - single pass measurement) transmission profile as a function of overlapped laser frequency and diagnostic laser frequency.

Unlike the transmission spectra seen in the jet characterization study, the ones encountered in this study did not appear to have any hyperfine features present. Upon model fitting to the TDLAS data it revealed that the average atom temperature was at or above ambient (300 K) conditions. Additionally, by using the estimated path length inside the chamber for each diagnostic system an average density at each station could be approximated from each absorption spectrum. This analysis revealed a spatial gradient in the density between the stations, however, it is still unlikely that this is due to a collimated jet. The results of this analysis are provided in Table 4.6. Both of these measurements indicate that there was substantial background rubidium in the chamber that completely dominated the absorption diagnostic. If there was a low divergence jet, it was completely overwhelmed in the TDLAS measurement. The root cause for the lack of a rubidium jet will be hypothesized in Section 4.2.4.

Diagnostic Station	Path Length (mm)	Rb Density (m^{-3})
1	716.5	2.99e14
2	475.7	1.65e14
3	257.9	0.61e14

Table 4.6: Estimated chamber density fit to diagnostic data after including the approximate diagnostic path length in the chamber for each station.

4.2.3 Overlapped Laser Extracted Profile

During the overlapped beam experiment, the extracted overlapped laser profile was imaged in five second intervals for the duration of the test. The laser profile image, shown in Figure 4.10, are primarily analyzed for low overlapped laser intensity studies as refractive effects will be more prominent in low saturation regimes (Section 2.2). The goal of analyzing the extracted laser profiles is to identify any spatial perturbations that could indicate refractive index light guiding as well as quantifying the overlapped laser attenuation in the jet.

While Section 4.2.2 indicated there was no substantial rubidium jet present, developing the techniques to analyze this information is still beneficial for future study. The first analysis is used

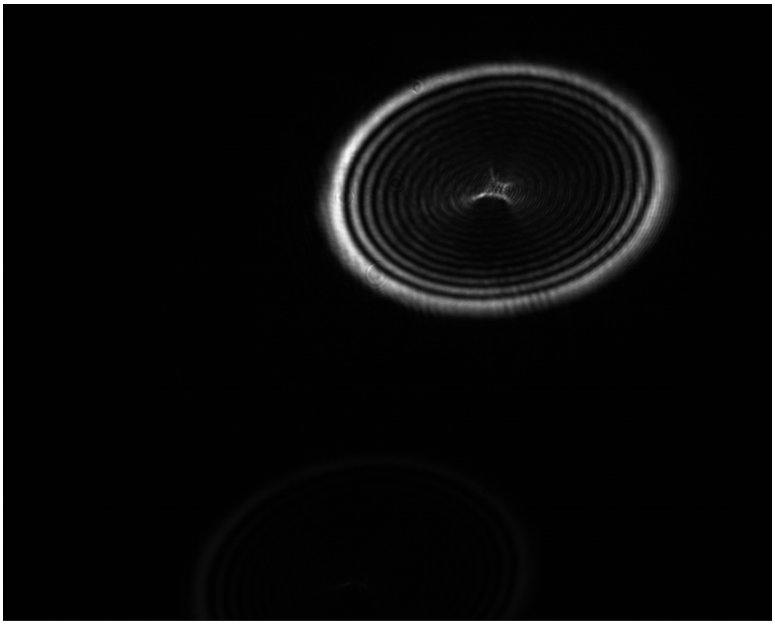

Figure 4.10: Extracted far-detuned overlapped laser profile during getter activation. Center diffraction pattern likely stems from edge clipping on the overlapping mirror with a Ø6 mm through hole.

to quantify overlapped laser attenuation by extracting the total image intensity and plot it as a function of overlapped laser frequency. Similar to using the ground state depletion in the TDLAS measurement as a function of overlapped laser frequency to measure the axial velocity, this image intensity as a function of overlapped laser frequency is a quantification of the same phenomenon. In order to utilize the images to quantify axial velocity, it must be certain that the camera is not saturated throughout the laser tuning range. Additionally, it is important to consider the images are highly susceptible to variation in lighting conditions.

Utilizing a modified code originally developed by Shockley [63], the length of the major and minor axes of the ellipses can be determined. The analysis code starts by setting all pixels with an intensity less than a declared threshold to 0 and all pixels greater than the threshold to 1. After this initial simplification process, the code sweeps through the columns to find the point at which it first encounters a 1 and the last time it encounters a 1. It then repeats this sweep over the rows to define the other axis of the ellipses. As long as the image simplification threshold value can be well defined, the image processing technique is able to find the bounds of the ellipse and can be used to

monitor for any major perturbations in the profile. An example of the image processing results is shown in Figure 4.11. However, since the overlapped beam experimented was contaminated with a substantial presence of background rubidium, there were no unique refractive index gradients that would lead to perturbation of the extracted laser profile. Small perturbations to the overlapped profile will require a more intricate and precise image processing technique.

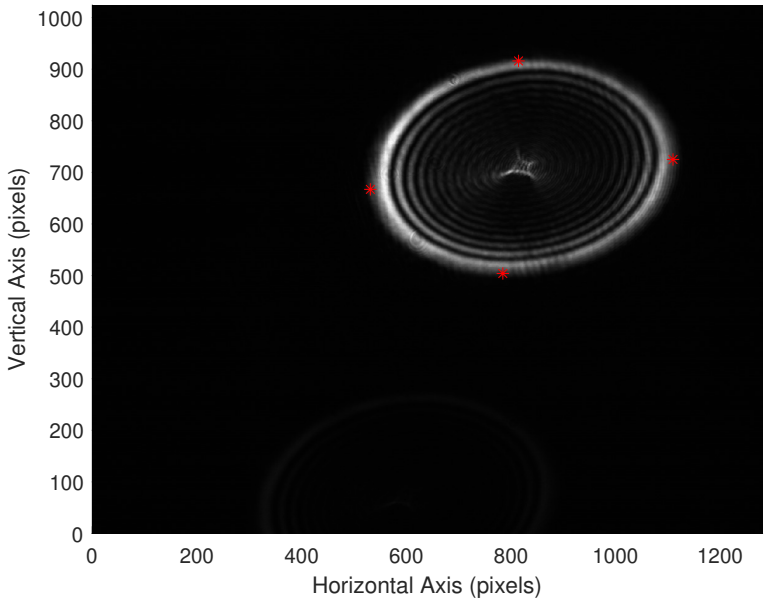

Figure 4.11: Analysis of an image of the extracted overlapped laser profile to identify the major and minor axes. The red points indicate identified sides of the ellipse.

4.2.4 Overlapped Beam Performance Discussion

As discussed throughout Section 4.2, this experiment did not yield a narrow divergence jet of rubidium as the jet characterization study did. Instead, diagnostic results (Section 4.2.2, indicated that the rubidium vapor present in the chamber was at ambient temperature with no uniform bulk velocity. This behavior could indicate two possible scenarios. The first possibility is that a low divergence rubidium jet was generated, but a condensation surface (either the beam dump or condensation shroud) did not perform well enough, thus allowing rubidium to accumulate in

the chamber and dominating the absorption spectrum. The second possibility is that no rubidium jet was generated and the rubidium from the source encountered some blockage/obstruction or other malfunction. Visual inspection upon chamber clean out after the test revealed a large pile of condensed rubidium in the shroud underneath the mouth of the rubidium getter. An image of the jet source with the condensed rubidium is shown in Figure 4.12. Additionally, there appeared to be substantial rubidium condensation on the shroud directly vertical of the lower rubidium pile. From this evidence, it is hypothesized that the getter was mounted in the holder with some inherent downward pitch angle. Upon activating the getter and melting the indium seal, the liquid rubidium alloy poured out of the getter where it condensed on the shroud. However, due to the high radiative heat loads from the activated getter relative to the conductive cooling from the shroud, the outermost rubidium in the pile was still evaporated. This new rubidium vapor then traveled out in all possible directions, with the most probable line of sight trajectory being the roof of the condensation shroud directly above where it recondensed. This also allowed some rubidium that did not collide with the shroud after evaporation to enter the vacuum chamber (e.g. through the back opening of the shroud). This rubidium vapor reached ambient conditions through collisions with the chamber walls and became visible in the diagnostic measurement as soon as the rubidium partial pressure in the chamber became sufficient. The getter manufacturer, AlfaVakuo, confirmed any downward pitch of the getter during activation would result in loss of the rubidium in the reservoir. This indicates an area for improvement or consideration in future effusive source designs. A method for mechanically fixturing the getter such that it cannot be mounted any a downward angle, or simply evaluating the slope of the getter after mounting with a level will be required to avoid this behavior in future experiments.

With the failure of the rubidium jet source in the experiment, it is still valuable to evaluate the behavior of other system elements to identify any corrections needed before embarking on future experiments. First, the data acquisition system utilized during testing will need to improved as discussed in Section 4.2.1. Having one data acquisition system capable of digitizing all seven voltage traces at a high sampling frequency would yield easier data processing, greater accuracy in

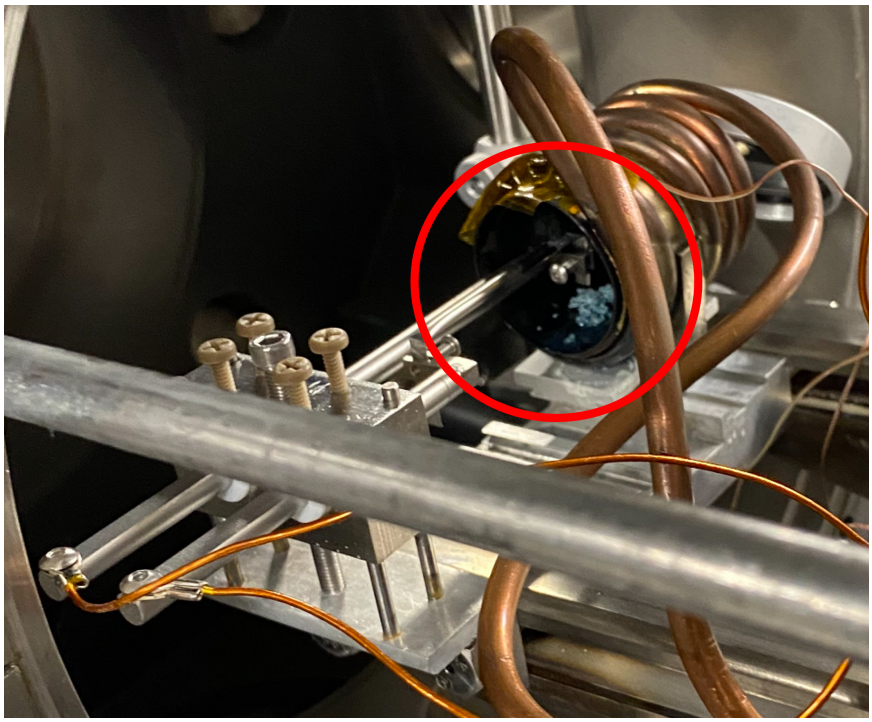

Figure 4.12: Rubidium jet source after overlapped beam experiment completion. A mound of condensed rubidium (circled in red) is directly below the mouth of the rubidium getter.

calculated parameters, and speed up data collection time. The overlapped beam decoupler system performed nominally by successfully extracting the overlapped laser beam for analysis. Additionally, the overlapped laser average intensity did not substantially decay over time, which indicated rubidium likely did not deposit on the optical surface. However, the interaction of the cold beam dump and heated beam decoupler system could not be evaluated due to the absence of a detectable rubidium jet. Lastly, for the overlapped laser extraction to determine axial velocity, it is necessary to ensure the camera image is not saturated at any point in the laser detuning such that image intensity can be used to generate an absorption spectrum as well.

The modified TDLAS diagnostic system performed very well during the experiment as it was able to conduct synchronized spatial scanning across three diagnostic stations. The gantry was able to produce accurate and repeatably stepping increments that quickly repositioned the diagnostic beam. This diagnostic also provided useful insights into the behavior of the gaseous rubidium present in the chamber. One interesting results of the plots shown in Figures 4.7 - 4.9, is the near

complete measurable depletion of the ground state for the entire laser path length. The initial assumption one would draw from a chamber filled with rubidium vapor and a small overlapped laser size relative to the chamber, is that there would still substantial ground state atoms outside of the laser path, however, from Figures 4.7 - 4.9, this does not appear to be an accurate hypothesis. A reason for the ground state depletion behavior seen during this study is hypothesized to stem from absorption in the atoms that are incident with the overlapped laser, then those photons are emitted upon decay from the excited state. These photons are then either reabsorbed by an atom outside that initial group or reflected off the chamber wall to then be absorbed by the vapor. From work done by Joythi et al. it is possible that the stainless steel chamber walls have a reflectance of 60% at 780 nm [64]. Due to the approximate reflectance of the walls and the estimated density values provided in Table 4.6 it appears that the assumption of an optically thick medium is potentially valid.

5. CONCLUSION AND FUTURE WORK

5.1 Conclusion

Reaching distant celestial bodies, including the nearest star system, require significant advancement in space propulsion techniques. Current innovations in the form of directed energy for space propulsion show promise by removing conventional reaction mass systems from the science spacecraft. However, directed energy concepts typically suffer significantly from beam divergence. As the momentum beam spreads out over the propagation, the thrust imparted to the spacecraft declines, thus limiting the terminal velocities of the craft. The self-guided beam propulsion concept aims to overcome this divergence and keep a near-collimated beam over substantially larger distances. This combined beam concept would provide a key to opening science missions beyond our solar system. While theory and simulation of this combined laser and atom beam interaction have seen important developments, there is the need to test the self-guiding phenomenon experimentally. Experimental testing would provide a method for validating simulations which could then be used to predict mission profiles and influence system designs.

The primary objective under this research was to develop infrastructure and apparatus capable of studying a self-guiding spatially overlapped laser and atom beam. In order to study the behavior of the self guiding beam multiple elements were designed, built, and tested including an ultra high-vacuum facility, effusive rubidium jet source, non-intrusive laser diagnostic technique, a method for overlapping the two beams, and a system for separating the laser and atom beam for analysis. The vacuum facilities proved capable of reaching 10^{-8} Torr of vacuum while providing sufficient optical access for visual inspection during the experiment, laser diagnostics, and to couple and remove the high-power overlapped laser beam. The laser diagnostic system provided accurate transmission spectra that utilized Doppler-free hyperfine and cross-over peaks of rubidium as a static reference. These transmission spectra for the initial jet characterization study indicated the combination of a hot and cold atom vapor present in the experiment which resulted from the source

emitting a flow that was not entirely in the free-molecular regime. Additionally, an absorption model fit to the data is used to extract the path integrated number densities, transverse temperature equivalent velocities, and bulk axial velocities. From these extracted parameters, the mass flow rate from the rubidium source was estimated and compared to the vendor's performance data. The results of the jet characterization study indicated that for overlapped laser detunings less than 30 GHz the atom jet would meet the minimum threshold for light guiding. The measured mass flow rates indicated a substantial inconsistency with vendor's specifications causing a redesign of the source to maintain heat in the rubidium reservoir. During testing of the modified effusive source, diagnostics indicated no or weak presence of jet. The leading hypothesis is a slight downward pitch while fixturing the getter caused the reservoir to drain into the condensation shroud. This source still requires further testing before its effectiveness can be truly evaluated. However, Section 5.2 will discuss a proposal for a different type of source and the rationale for moving beyond an effusive source.

The apparatus developed for overlapping the high-power guiding laser also proved effective as the laser was able to be aligned along the central axis of the chamber and brought to a varying focal point. Lastly, the novel beam decoupler system was successful in extracting the overlapped laser and preventing rubidium condensation on the optical surface, resulting in a consistent extracted laser profile during the test cycle. Due to the absence of the beam, the coupled thermal nature of the heated beam decoupler adjacent to the chilled atom beam dump could not be fully evaluated. While the final overlapped beam experiment was not able to study the mutual guiding effects, it served as a benchmark test for the testing hardware and infrastructure. All systems except for the effusive source were able to be proven effective for use in these studies and to quantify the behavior of the both constituent beams in the self-guiding propulsion concept. While this work was not able to produce coupled beam results to validate simulations for the development of the propulsion concept, the infrastructure to gather this information has been evaluated and is prepared for future experiments.

5.2 Future Work

There are several suggested areas for improvement with the system to better generate the self-guiding beam and more accurately quantify the system parameters. Several sources of error have been described throughout Section 4, one of the most critical still remaining to be addressed is the rubidium absorption model assuming a Maxwellian VDF. By modeling the absorption features in the jet based on the Gaussian lineshape for thermal Doppler broadening, there will be an inherent error in the fitted density and temperature for the spectrum. Work will be needed to develop a robust function that uses geometric source parameters as inputs and applies the proper transverse velocity Doppler broadening distribution to the spectrum such that the density and temperature parameters can be fit more appropriately.

To improve the manifestation of self-guiding effects, either mutually or individually, it is necessary to increase atom density, reduce transverse velocity, and extend the propagation length. Propagation length is a rather trivial thing to modify by adding a elongated vacuum nipple to the chamber. The purpose of providing a greater propagation distance is to allow more time for the dipole force to influence the atoms. Increasing the propagation length could allow for the exhibition of the coupled guiding effect where a focused group of atoms increases the refractive index, focuses the overlapped laser, which in turn, focuses the atoms. Lastly, increasing the density of the atom jet by orders of magnitude or more would provide substantial increase to the refractive guiding of the overlapped laser. For an increased mass flow rate from the source, the laser diagnostic systems would experience a larger signal to noise ratio, thus allowing for the detection of smaller changes in the density distribution along the propagation length of the jet.

A final area for improvement is the rubidium atomic source. Modifications can be made to the newest effusive source design to increase mass flow rate such as increasing the volume of the rubidium reservoir or increasing the diameter of the getter. However, developments of a supersonic source show potential for high density beams with inherently low divergence [65]. With the infrastructure already evaluated and proven functional, new source designs can be tested that would provide a greater atom beam density.

REFERENCES

[1] C. Cai and I. D. Boyd, "Collisionless Gas Expanding into Vacuum," *Journal of Spacecraft and Rockets*, vol. 44, no. 6, pp. 1326–1330, 2007.

[2] E. G. Flekkøy, J. Luu, and R. Toussaint, "The Interstellar Object 'Oumuamua as a Fractal Dust Aggregate," *The Astrophysical Journal Letters*, vol. 885, 2019.

[3] G. A. Landis, "A Telescope at the Solar Gravitational Lens: Problems and Solutions," in *Tennessee Valley Interstellar Workshop (TVIW 2017)*, 2017.

[4] S. G. Turyshev and B.-G. Andersson, "The 550 AU Mission: A Critical Discussion," *Monthly Notices of the Royal Astronomical Society*, no. 341, pp. 577–582, 2003.

[5] G. Anglada-Escudé, P. J. Amado, J. Barnes, Z. M. Berdiñas, R. P. Butler, G. A. Coleman, I. De La Cueva, S. Dreizler, M. Endl, B. Giesers, S. V. Jeffers, J. S. Jenkins, H. R. Jones, M. Kiraga, M. Kürster, M. J. López-González, C. J. Marvin, N. Morales, J. Morin, R. P. Nelson, J. L. Ortiz, A. Ofir, S. J. Paardekooper, A. Reiners, E. Rodríguez, C. Rodríguez-López, L. F. Sarmiento, J. P. Strachan, Y. Tsapras, M. Tuomi, and M. Zechmeister, "A terrestrial planet candidate in a temperate orbit around Proxima Centauri," *Nature*, vol. 536, pp. 437–440, 2016.

[6] R. L. Forward, "Exotic Power and Propulsion Concepts," tech. rep., NASA, 1990.

[7] L. Johnson, R. Young, E. Montgomery, and D. Alhorn, "Status of solar sail technology within NASA," *Advances in Space Research*, vol. 48, pp. 1687–1694, 12 2011.

[8] G. A. Landis, "Advanced Solar- and Laser-pushed Lightsail Concepts," no. 216, 1999.

[9] H.-T. Tung and A. Davoyan, "Light-Sail Photonic Design for Fast-Transit Earth Orbital Maneuvering and Interplanetary Flight," tech. rep., University of California Los Angeles, Los Angeles, CA.

[10] G. Swartzlander, L. Johnson, and B. Betts, "Light Sailing into the Great Beyond," *Optics and Photonics News*, vol. 31, 2020.

[11] T. F. Sheerin, E. Petro, K. Winters, P. Lozano, and P. Lubin, "Fast Solar System transportation with electric propulsion powered by directed energy," *Acta Astronautica*, vol. 179, pp. 78–87, 2 2021.

[12] V. Lappas, N. Adeli, L. Visagie, J. Fernandez, T. Theodorou, W. Steyn, and M. Perren, "CubeSail: A low cost CubeSat based solar sail demonstration mission," *Advances in Space Research*, vol. 48, pp. 1890–1901, 12 2011.

[13] V. Lappas, B. Wie, C. McInnes, L. Tarabini, L. Gomes, and K. Wallace, "Microsolar sails for earth magnetotail monitoring," *Journal of Spacecraft and Rockets*, vol. 44, no. 4, pp. 840–848, 2007.

[14] J. C. Horvath and R. H. Frisbee, "Laser Propulsion for Orbit Transfer: Laser Technology Issues.," in *AIAA Fluid Dynamics and Plasmadynamics and Lasers Conference*, (Cincinnati, OH), pp. 1–6, American Institute of Aeronautics and Astronautics Inc., 1985.

[15] A. Kantrowitz, "Laser Propulsion to Earth Orbit," *AIAA Meeting Paper*, 1975.

[16] J. Brophy, "A Breakthrough Propulsion Architecture for Interstellar Precursor Missions," 2018.

[17] F. L. Pedrotti, L. M. Pedrotti, and L. S. Pedrotti, *Introduction to Optics*. Pearson, 3 ed., 2013.

[18] V. Koblik, E. Polyakhova, and L. Sokolov, "Controlled solar sail transfers into near-sun regions combined with planetary gravity-assist flybys," *Celestial Mechanics and Dynamical Astronomy*, vol. 86, no. 1, pp. 59–80, 2003.

[19] I. Levchenko, K. Bazaka, S. Mazouffre, and S. Xu, "Prospects and Physical Mechanisms for Photonic Space Propulsion," *Nature Photonics*, vol. 12, no. 11, pp. 649–657, 2018.

[20] M. Macdonald, G. W. Hughes, C. R. McInnes, A. Lyngvi, P. Falkner, and A. Atzei, "Solar Polar Orbiter: A solar sail Technology Reference Study," *Journal of Spacecraft and Rockets*, vol. 43, no. 5, pp. 960–972, 2006.

[21] R. L. Forward, "Roundtrip interstellar travel using laser-pushed lightsails," *Journal of Spacecraft and Rockets*, vol. 21, no. 2, pp. 187–195, 1984.

[22] I. G. Brown, J. E. Lane, and R. C. Youngquist, "A lunar-based spacecraft propulsion concept-The ion beam sail," *Acta Astronautica*, vol. 60, no. 10-11, pp. 834–845, 2007.

[23] G. A. Landis, "Flight by Particle," in *STAIF Conference on Innovative Transportation Systems for Exploration of the Solar System and Beyond*, (Albuquerque), 2001.

[24] C. Limbach and K. Hara, "PROCSIMA: Diffractionless Beamed Propulsion for Breakthrough Interstellar Missions," tech. rep., NIAC Report No. HQ-E-DAA-TN67917, 2019.

[25] I. D. Boyd and T. E. Schwartzentruber, *Nonequilibrium Gas Dynamics and Molecular Simulation*. Cambridge University Press, 2017.

[26] J. T. Kare, "SailBeam: Space Propulsion by Macroscopic Sail-type Projectiles," in *Space Technology and Applications International Forum 2001*, pp. 402–406, 2001.

[27] G. D. Nordley and A. J. Crowl, "Mass beam propulsion, an overview," *JBIS - Journal of the British Interplanetary Society*, vol. 68, no. 5-6, pp. 153–166, 2015.

[28] P. Kumar, D. Kuldinow, A. Castillo, A. Gerakis, and K. Hara, "Nonlinear dynamics of coupled light and particle beam propagation," *Physical Review A*, vol. 103, no. 4, 2021.

[29] A. Castillo, D. Kuldinow, and K. Hara, "Collisional effects in a laser and particle coupled beam," in *AIAA Propulsion and Energy 2020 Forum*, (Virtual Event), American Institute of Aeronautics and Astronautics Inc., 2020.

[30] D. Kuldinow, K. Hara, D. Morales, and C. Limbach, "Numerical Simulation of Laser and Particle Coupled Beam Propagation," in *AIAA Propulsion and Energy Forum*, (Indianapolis, IN), 2019.

[31] J. E. Bjorkholm, R. R. Freeman, A. Ashkin, and D. B. Pearson, "Observation of Focusing of Neutral Atoms by the Dipole Forces of Resonance-Radiation Pressure," *Physical Review Letters*, vol. 41, no. 20, pp. 1361–1364, 1978.

[32] A. W. Snyder and W. R. Young, "Modes of Optical Waveguides.," *Journal of the Optical Society of America*, vol. 68, no. 3, pp. 297–309, 1978.

[33] S. Wang, J. Yuan, L. Wang, L. Xiao, and S. Jia, "Measurement of the Kerr nonlinear refractive index of the Rb vapor based on an optical frequency comb using the z-scan method," *Optics Express*, vol. 28, no. 25, 2020.

[34] E. D. Hinkley, "High-resolution infrared spectroscopy with a tunable diode laser," *Applied Physics Letters*, vol. 16, no. 9, pp. 351–354, 1970.

[35] J. R. Gilbert, C. P. Roberts, and J. L. Roberts, "Near-resonant light propagation in an absorptive spatially anisotropic ultracold gas," *Journal of the Optical Society of America B*, vol. 35, no. 4, pp. 718–723, 2018.

[36] P. C. Bons, R. De Haas, D. De Jong, A. Groot, and P. Van Der Straten, "Quantum Enhancement of the Index of Refraction in a Bose-Einstein Condensate," *Physical Review Letters*, vol. 116, no. 17, 2016.

[37] P. B. Wigley, P. J. Everitt, K. S. Hardman, M. R. Hush, C. H. Wei, M. A. Sooriyabandara, P. Manju, J. D. Close, N. P. Robins, and C. C. N. Kuhn, "Non-destructive shadowgraph imaging of ultra-cold atoms," *Optics Letters*, vol. 41, no. 20, pp. 4795–4798, 2016.

[38] N. Davidson, H. J. Lee, S. Adams, M. Kasevich, and S. Chu, "Long Atomic Coherence Times in an Optical Dipole Trap," *Physical Review Letters*, vol. 74, no. 8, pp. 1311–1314, 1995.

[39] A. Urvoy, Z. Vendeiro, J. Ramette, A. Adiyatullin, and V. Vuletić, "Direct Laser Cooling to Bose-Einstein Condensation in a Dipole Trap," *Physical Review Letters*, vol. 122, no. 20, 2019.

[40] R. Grimm, M. Weidemüller, and Y. B. Ovchinnikov, "Optical Dipole Traps for Neutral Atoms," *Advances in Atomic, Molecular and Optical Physics*, vol. 42, no. C, pp. 95–170, 1999.

[41] H. Metcalf and P. Van der Straten, "Laser Cooling and Trapping of Atoms," *Journal of the Optical Society of America*, vol. 20, no. 5, pp. 887–908, 2003.

[42] C. J. Foot, *Atomic Physics*. Oxford University Press, 1 ed., 2005.

[43] S. Chu, J. E. Bjorkholm, A. Ashkin, and A. Cable, "Experimental Observation of Optically Trapped Atoms," *Physical Review Letters*, vol. 57, 1986.

[44] J. Hu, A. Urvoy, Z. Vendeiro, V. Crépel, W. Chen, and V. Vuletić, "Creation of a Bose-condensed gas of rubidium 87 by laser cooling," *Science*, 2017.

[45] D. Fagnan, "Study of Collision Cross Section of Ultra-Cold Rubidium using a Magneto-Optic and Pure Magnetic Trap," *Bachelor of Science Thesis*, 2009.

[46] B. I. Robertson, *High Contrast Measurements with a Bose-Einstein Condensate Atom Interferometer*. PhD thesis, University of Strathclyde Glasgow, 2016.

[47] P. Meystre and M. Sargent III, *Elements of Quantum Optics*. Springer, 4 ed., 2007.

[48] D. A. Steck, *Quantum and Atom Optics*. PhD thesis, University of Oregon, Eugene, Oregon, 2007.

[49] W. Demtröder, *Laser Spectroscopy: Basics Concepts and Instrumentation*. Springer, 3 ed., 2003.

[50] B. E. A. Saleh and M. C. Teich, *Fundamentals of Photonics*. Wiley, 3rd ed., 1991.

[51] H. P. Morgan, D. Morales, W. L. Hodges, R. D. Jillapalli, and C. M. Limbach, "Design and characterization of an atomic rubidium jet source for particle beam space propulsion," in *AIAA Propulsion and Energy Forum*, (Virtual Event), American Institute of Aeronautics and Astronautics Inc., 2020.

[52] G. Sanna and G. Tomassetti, *Introduction to Molecular Beams Gas Dynamics*. Imperial College Press, 2005.

[53] H. C. W. Beijerinck and N. F. Verster, "Absolute Intensities and Perpendicular Temperature of Supersonic Beams of Polyatomic Gases," *Physica*, 1981.

[54] D. A. Steck, "Rubidium 87 D Line Data," 2001.

[55] D. A. Steck, "Rubidium 85 D Line Data," 2019.

[56] A. Banerjee and V. Natarajan, "Saturated-absorption spectroscopy: eliminating crossover resonances by use of copropagating beams," *Optics Letters*, vol. 28, no. 20, pp. 1912–1914, 2003.

[57] C. M. Limbach and K. Hara, "Performance analysis of a combined laser and neutral particle beam propulsion concept based on self-guiding," in *AIAA Propulsion and Energy Forum*, (Indianapolis, IN), 2019.

[58] C. Limbach, "Landau Damping in the Transverse Modulational Dynamics of Co-Propagating Light and Matter Beams." 2021.

[59] K. L. Moore, T. P. Purdy, K. W. Murch, S. Leslie, S. Gupta, and D. M. Stamper-Kurn, "Collimated, Single-Pass Atom Source from a Pulsed Alkali Metal Dispenser for Laser-Cooling Experiments," *Review of Scientific Instruments*, vol. 76, no. 2, 2005.

[60] I. H. Malitson, "Interspecimen Comparison of the Refractive Index of Fused Silica," *Journal of the Optical Society of America*, vol. 55, no. 10, pp. 1205–1209, 1965.

[61] A. Rekhy, A. Gerakis, D. Feng, M. N. Shneider, A. Dogariu, and R. Miles, "Temperature profiling of the atmosphere from an airborne lidar by dispersion of filtered rayleigh scattering in atomic and molecular vapors," in *AIAA Aviation 2019 Forum*, (Dallas, TX), 2019.

[62] C. Cai and I. D. Boyd, "Theoretical and numerical study of free-molecular flow problems," *Journal of Spacecraft and Rockets*, vol. 44, no. 3, pp. 619–624, 2007.

[63] L. M. Shockley, "Spacecraft Attitude Determination Using Terrestrial Illumination Matching," 2020.

[64] J. Jyothi, A. Biswas, P. Sarkar, A. Soum-Glaude, H. S. Nagaraja, and H. C. Barshilia, "Optical properties of TiAlC/TiAlCN/TiAlSiCN/TiAlSiCO/TiAlSiO tandem absorber coatings by phase-modulated spectroscopic ellipsometry," *Applied Physics A: Materials Science and Processing*, vol. 123, no. 7, 2017.

[65] K. Luria, W. Christen, and U. Even, "Generation and Propagation of Intense Supersonic Beams," *Journal of Physical Chemistry A*, vol. 115, no. 25, pp. 7362–7367, 2011.

[66] A. Banerjee, D. Das, and V. Natarajan, "Absolute frequency measurements of the D1lines in 39K, 85Rb, and 87Rb with - 0.1 ppb uncertainty," *Europhysics Letters*, vol. 65, no. 2, pp. 172–178, 2004.

[67] E. Arimondo, M. Inguscio, and P. Violino, "Experimental determinations of the hyperfine structure in the alkali atoms," *Reviews of Modern Physics*, vol. 49, no. 1, pp. 31–75, 1977.

[68] J. Ye, S. Swartz, P. Jungner, and J. L. Hall, "Hyperfine structure and absolute frequency of the 87Rb 5P_3/2 state," *Optics Letters*, vol. 21, no. 16, pp. 1280–1282, 1996.

[69] S. Bize, Y. Sortais, M. S. Santos, C. Mandache, A. Clairon, and C. Salomon, "High-accuracy measurement of the 87Rb ground-state hyperfine splitting in an atomic fountain," *Europhysics Letters*, vol. 45, no. 5, pp. 558–564, 1999.

APPENDIX A

RUBIDIUM TRANSITION INFORMATION

The following are figures are diagrams of the hyperfine energy splittings for the ^{85}Rb and ^{87}Rb D_2 transitions. Information for these figures is provided by [54, 55, 66, 67, 68, 69].

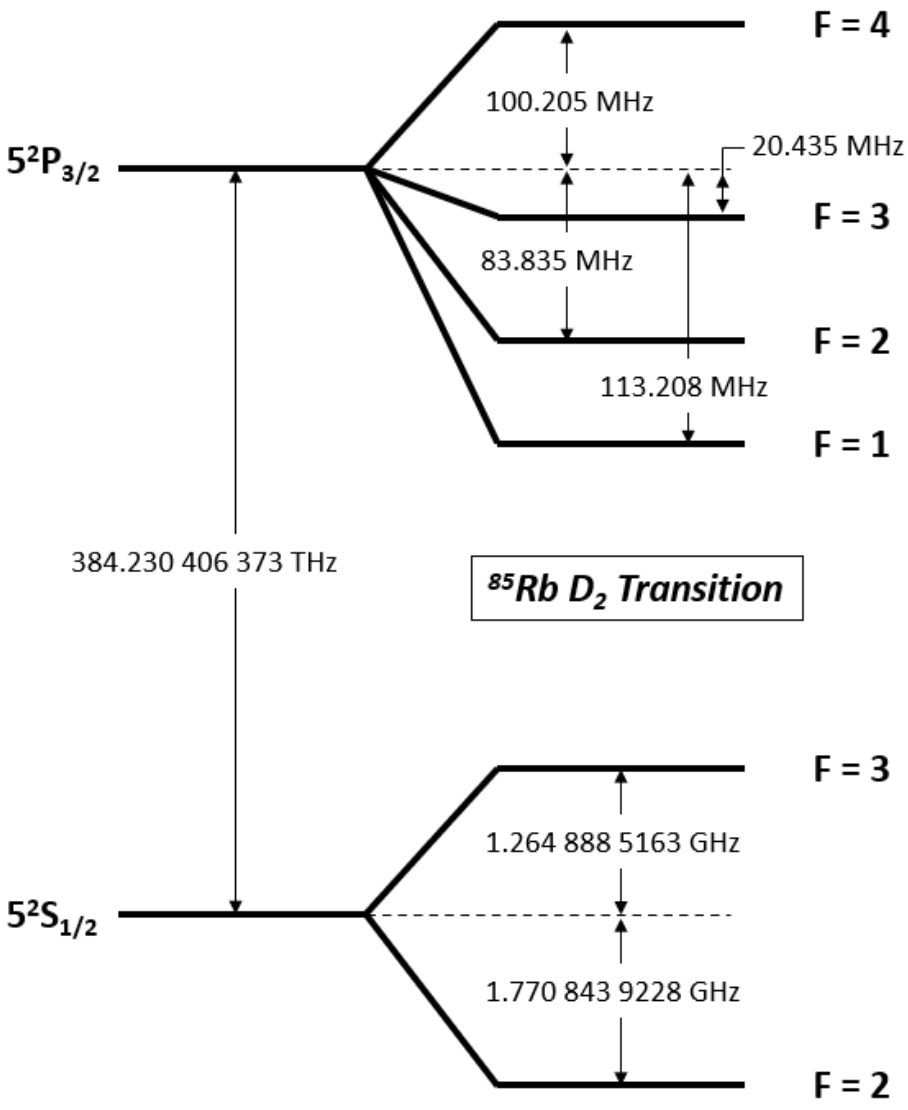

Figure A.1: ^{85}Rb D_2 transition diagram

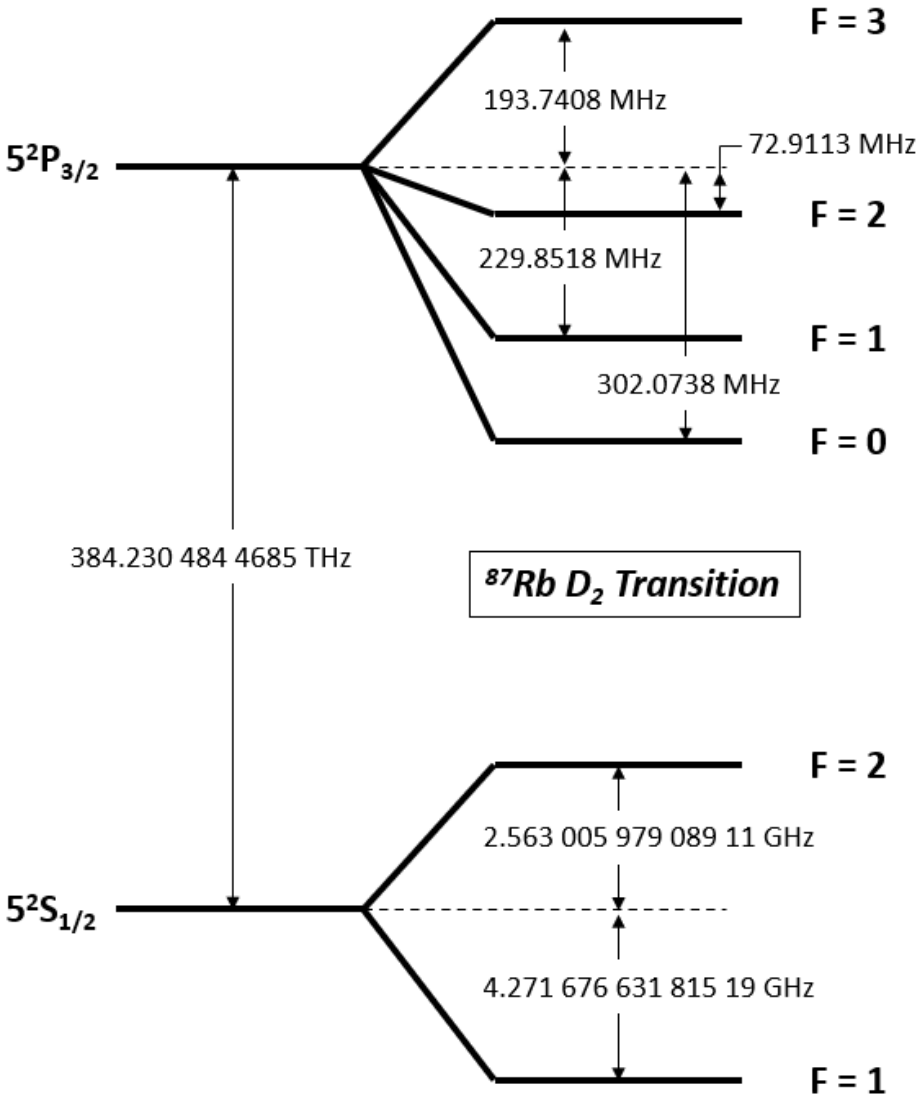

Figure A.2: ^{87}Rb D_2 transition diagram